High-Frequency Study of Two-Dimensional Materials

Kun Meng

Submitted in accordance with the requirements

for the degree of Doctor of Philosophy

University of Leeds

School of Electronic and Electrical Engineering

May 2019

The candidate confirms that the work submitted is his own and that appropriate credit has been given where reference has been made to the work of others.

This copy has been supplied on the understanding that it is copyright material and that no quotation from the thesis may be published without proper acknowledgement.

Acknowledgement

Rubino, and Craig Knox for the many interesting discussions with you all. I would also like to thank Sue Hobson for her administrative help and support.

Last but not least, I would like to thank my family. I wouldn't even have started my PhD study without your support. I would also like to thank all my friends for their ongoing support throughout my studies.

Abstract

Two-dimensional (2D) materials show different properties from three-dimensional materials owing to the quantum confinement they have in the vertical direction (perpendicular to their plane). Graphene, as the first established one-atom-thick 2D material, has received widespread attention owing to its versatile and rather extraordinary properties. Metasurfaces, as an artificial 2D material, have shown potential for new functional electromagnetic (EM) devices since they possess EM properties not found in natural materials. On top of that, the graphene-metasurface hybrid devices are receiving progressing attention.

This thesis investigates the two 2D materials' interactions with high-frequency signals, aiming to develop some exemplar applications, including a high-sensitive dielectric sensor, a THz-pulse detector, a broadband tunable THz polarizer, and tunable (MHz – GHz) acoustoelectric (AE) current source.

The interaction of 2D materials with THz waves was first investigated. The resonant frequency of a THz split-ring resonator (SRR) was found to be altered by the introduction of etched trenches into the LC gap area, owing to a reduction in the effective permittivity, which allowed a significant enhancement in its sensitivity to overlaid dielectric material.

Carriers in graphene can be accelerated by the electrical field of free-space THz pulse, which enabled a free-space THz detector, whose performances were also tested.

Combining the technologies developed in these two projects, the interaction between graphene-metasurface hybrid devices and THz waves was next explored. Our graphene-metal hybrid stripe arrays showed both a significant direction-dependent transmission, and a strong modulation effect for the transmitted THz waves across a wide frequency range, so demonstrating a broadband tunable THz polarizer.

2D materials interacting with surface acoustic waves (SAWs) were then investigated. The SAW induced carriers transport in graphene was examined with SAW frequencies from 10s of MHz to GHz and at cryogenic to room temperature. Experiments were made on bars of graphene, graphene ribbons and gate-modulated graphene strips. The combination of these works suggests strong future possibilities for the study of quantized AE currents in graphene.

Table of Contents

List of Figures

List of Tables

List of Acronyms

2D	Two-dimensional
2DES	Two-dimensional electron system
AE	Acoustoelectric
ALD	Atomic layer deposition
CVD	Chemical vapour deposition
DC	Direct current
DI	Deionized
EBL	Electron beam lithography
EM	Electromagnetic
FFT	Fourier transform
fs	Femtosecond
FWHM	Full width at half maximum
IDT	Interdigitated transducer
LC	Inductive-capacitive
LT-GaAs	Low-temperature-grown gallium arsenide

OL	Optical lithography
PC	Photoconductive
PDMS	Polydimethylsiloxane
PER	Polarization extinction ratio
PMMA	Poly-(methyl methacrylate)
RF	Radio-frequency
RIE	Reactive ion etching
SAW	Surface acoustic wave
SEM	Scanning electron microscopy
SMU	Source-measurement unit
SNR	Signal-to-noise ratio
SRR	Split-ring resonator
TDS	Time-domain spectroscopy
THz	Terahertz

Chapter 1 Introduction

When the size of one dimension of a material is continuously reduced, the properties of the material start to change when the size gets down to hundreds of nanometers owing to the quantum confinement which is produced in this direction. This reduction in dimensionality influences the electronic, chemical, optical, and magnetic properties of materials. If the confinement is seen in one dimension while the other two dimensions remain large, the material is called two-dimensional (2D). Ideal 2D materials have zero thickness, while one-atom-thick material are the thinnest material that can be obtained in nature since the atom is the basic unit of matter. Monolayer graphene is one-atom-thick 2D carbon, and this strictly 2D material has revealed a wealth of new physics and potential applications [1]. Metasurfaces, which can be defined as an artificial-material layer with sub-wavelength thickness, can also be treated as one-atom-thick 2D materials since they are composed of one layer of "meta-atom" arrays; they have received wide attention since they can show electromagnetic (EM) properties not found in natural materials [2]. This chapter introduces the developments of these two kinds of 2D materials. The contents of this thesis regarding the high-frequency studies of 2D materials are then listed.

1.1 Two-dimensional materials

1.1.1 Graphene

Since the realization in 2004 [3] of graphene, it has received widespread attention owing to its versatile and rather extraordinary properties. Firstly, graphene contains the lightest charge carriers, massless Dirac fermions [4], with the longest carrier mean free paths (of micron scale) at room temperature [5], meaning that a high carrier mobility is reachable in graphene without cooling. Secondly, graphene has high electrical conductivity and a high optical transparency [6], and can bare very high current densities (millions of times that achievable in copper) at room temperature [7], making it preferable to metals for some applications, including its use for transparent electrodes and in supercapacitors. On top of that, the flexible and stretchable mechanical properties of graphene indicate potentially promising applications in flexible electronics [8]. It shows unique electrical properties, such as an anomalous integer quantum Hall effect [4], Klein tunnelling [9], and spin-orbit coupling [10], which have not only created active interests in the field of physics, but also have the potential to lead to new kinds of functional devices. [11, 5, 12] People thus believe that graphene could be incorporated into both electronic and optoelectronic devices in the next few years [8].

Several techniques to synthesize graphene were developed shortly after the discovery of graphene, which have enabled the explosion of interest. In general, there are two main categories of approach to graphene synthesis: the top-down approach and the bottom-up approach [13, 14]. The top-down approach is to separate sheets of graphene from graphite by means of

mechanical exfoliation [3], chemical exfoliation [15], or electrochemical exfoliation [16]. The bottom-up approach treats carbon atoms as building blocks. Techniques falling into this category include chemical vapour deposition (CVD) [17], and epitaxial growth [18]. Graphene grown by CVD [19] is probably the most promising synthesis method for industrial-scale graphene production, since it produces large sheets of the material.

In electronics, graphene has generated intense interest for use in high-frequency transistors. By reducing the source-gate spacing [20] and the channel length [21], extremely high-frequency graphene resistors have been created. Graphene transistors with operating frequencies beyond 100 GHz have been achieved [22, 23], while cut off-frequencies as high 1.4 THz cut-off frequency may be reachable [21]. Furthermore, graphene transistors capable of logic operations have also been realized by opening a bandgap in the material [24]. On the other hand, the outstanding optical transparency, mechanical flexibility, and chemical durability have all enabled graphene to be proposed as an excellent material for flexible electronic devices, such as touch screens, and for e-paper [8]. In photonics, the wavelength-independent absorption of visible light [25], the Pauli blocking in infrared light [26], and the plasmonic properties for terahertz waves [27] all indicate that graphene is suitable for many applications, including controllable photonic devices [27], laser/THz generators [28], photodetectors [29], optical modulators [30] and polarization controllers [31].

1.1.2 Metasurface

Metamaterials are engineered materials composed of arrays of individual elements, which have attracted considerable interest due to their many extraordinary EM properties which do not easily exist in nature, including negative index of refraction, artificial magnetism, negative permittivity, and negative permeability [2, 32, 33, 34]. In 3D metamaterials, apart from the artificial EM properties, there are some additional loss and dispersion induced by the bulk materials used for constructing the metamaterials. Metasurfaces, which the term used for 2D metamaterials, can significantly suppress this kind of undesirable loss and dispersion owing to the subwavelength thickness in the wave propagation direction [35]. Many new applications are enabled by these new properties, including perfect lensing [36], sub-wavelength imaging [37] and sensing [38], unique optical controller [39], etc., are all being actively intensively researched, demonstrating they are promising materials for functional EM devices.

The planar nature of metasurfaces means that they can be easily integrated with active functional materials and tuned by external stimuli. As mentioned earlier, graphene has excellent mechanical properties, and its carrier density and optical properties are tuneable by electrical gating, making it a suitable material to enable active metasurfaces [40, 35]. By tuning the optical conductivity of graphene which is located at the active region of metasurfaces, the resonant intensity [41, 42, 43, 44], frequency [45] and the polarization properties [46] of the metasurfaces can each be tuned over a wide range. On top of that, patterned graphene structures themselves

also exhibit resonant plasmonic responses [47, 48], and this additional light-plasmon coupling suggests that graphene could change the properties of metamaterials not only because of conductivity modulation, but also because of the plasmonic effects.

1.2 Outline of thesis

This thesis discusses the interactions between high-frequency signals with the two 2D materials introduced above (graphene and metasurfaces), and demonstrates some potential applications based on them, including a high-sensitivity THz dielectric sensor, a graphene-based free-space THz-pulse detector, a tunable THz polarizer, and a tunable (MHz – GHz) acoustoelectric current source. An outline of this thesis is as follows:

Chapter 2 contains a discussion of the theoretical frameworks relevant to the project. Theories of the band-induced electronic properties of graphene are first briefly discussed. The terahertz properties of graphene, and the terahertz wave interaction with graphene metasurfaces are then introduced. Afterwards, surface acoustic wave induced carrier transport in graphene is discussed.

Chapter 3 then goes on to discuss the key enabling technologies utilized and further developed in the course on my work, including the device fabrication routes, graphene identification and isolation, and experimental measurement techniques developed or adopted, and which are then used in the following chapters.

Chapter 4 demonstrates an enhancement to the sensitivity of split-ring resonators (SRRs) acting as terahertz dielectric sensors. By introducing localized etched trenches in the LC gap area of SRRs, the effective permittivity of the metamaterials is reduced. As a result, the THz response properties of the etched SRRs show a blue shift while their sensitivity for dielectric sensing is enhanced. These aspects are examined at length both in THz-TDS measurements and in simulations.

In chapter 5 THz detectors and polarizers are examined based on the principle of graphene interacting with terahertz waves. A graphene bowtie photoconductive antenna enabling free-space terahertz wave detection is first fabricated, and its performance examined. Broadband tunable THz polarizers using the graphene-metasurface hybrid structures are then proposed and investigated. These hybrid structures dramatically enhance the direction-dependent terahertz wave modulation, which is both theoretically discussed and experimentally demonstrated

In the final experimental chapter (chapter 6), surface acoustic wave induced carriers transport in graphene channels is explored based on the acoustoelectric (AE) effect. Graphene AE devices working at up to GHz frequencies, and operating at low temperatures, tunable using gate voltages are realized. AE current induced by carrier localization behaviour in graphene nanoribbons is also observed.

Conclusions of the research and possible future work leading on from the thesis are discussed in chapter 7.

Chapter 2 Theoretical background

2.1 Chapter introduction

This chapter discusses the theoretical framework relevant to this project. The general electronic properties of graphene are first introduced. Afterwards, the behavior of graphene's interaction with two kinds of high-frequency signals, terahertz waves and surface acoustic waves, are discussed.

2.2 Electronics of graphene

Strictly speaking, graphene is a single layer of carbon atoms densely packed into a lattice which is composed of benzene-ring-like structures [3]. This project focuses predominantly on the properties of this monolayer graphene.

2.2.1 Bandstructure

It is the four outermost electrons in a carbon atom which can participate in the formation of covalent chemical bonds. In graphene, three exterior electrons in each atom participate in forming in-plane σ-bonds (sp^2 hybrid orbitals) with nearest-neighbouring atoms, whose bond energy is 615 kJ/mol, which is much stronger than the C-C bonds in diamond (345 kJ/mol), making

it one of the strongest films [11]. On the other hand, the electrons in $2p_z$ orbitals, which are oriented perpendicular to the graphene plane, form delocalized π-bonds, which determine most of the electronic properties of graphene. [11]

The energy band of graphene can be derived from the tight-binding Hamiltonian, which can be written as formula 2.1 when considering the electron hopping between the nearest- and next-nearest-neighbour atoms. [5, 49]

$$E_{\pm}(\vec{k}) = \pm t\sqrt{3 + f(\vec{k})} - t'f(\vec{k}) \qquad 2.1$$

with $\qquad f(\vec{k}) = 2\cos(\sqrt{3}k_y a) + 4\cos\left(\frac{\sqrt{3}}{2}k_y a\right)\cos\left(\frac{3}{2}k_x a\right)$

where, a is the carbon-carbon distance; t and t' are the hopping energy of nearest-neighbour and next-nearest-neighbour atoms, respectively; The plus sign applies to the π^* (conduction) band and the minus sign applies to the π (valence) band.

The band structure of graphene in reciprocal space can be obtained by solving the tight-binding Hamiltonian, as shown in Fig. 2.1. It can be seen that the conduction and valence bands meet at the points of $\vec{K} = \left(\frac{2\pi}{3a}, \frac{2\pi}{3\sqrt{3}a}\right)$ and $\vec{K'} = \left(\frac{2\pi}{3a}, -\frac{2\pi}{3\sqrt{3}a}\right)$, which are named Dirac points or charge neutrality points, making graphene a gapless material.
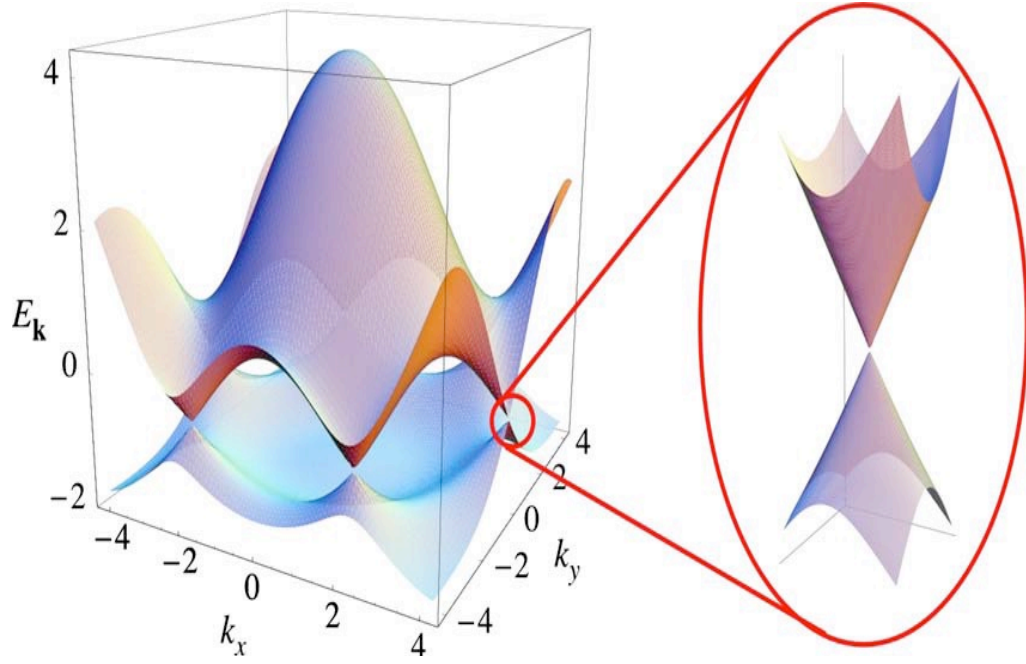
Figure 2.1 Band structure of graphene calculated using tight-binding approach. Taken from Ref. **[5]**

Near the K and K' points, the dispersion relation can be written as follows:

$$E_{\pm}(\vec{q}) \approx \pm v_F |\vec{q}| + O\left[\left(\frac{q}{K}\right)^2\right] \qquad 2.2$$

where, q is the momentum measured relatively to the Dirac points, and v_F is Fermi velocity. If the hopping energy of next-nearest-neighbour atoms is zero, the second term of formula 2.2, $O\left[\left(\frac{q}{K}\right)^2\right]$, is negligible. In that case, the dispersion relation of the graphene close to the K and K' points is linear since the value of Fermi velocity is independent of the energy or momentum and takes a value of around 10^6 m/s calculated by $v_F = 3ta/2$. This linear-dispersion relation can be well described by the 2D relativistic Dirac

equation, indicating charge carriers in graphene are massless Dirac Fermions, which has been experimentally demonstrated [4].
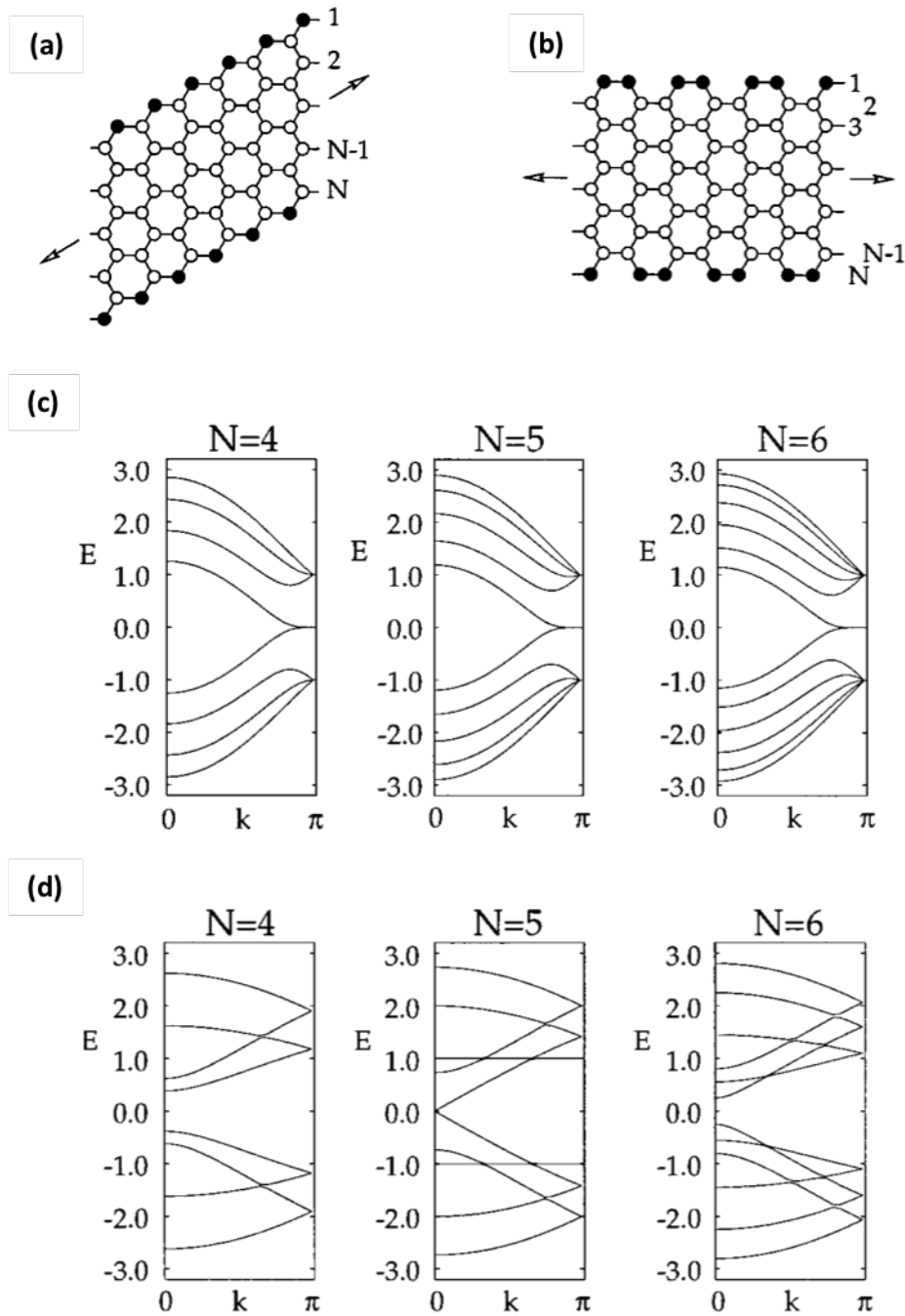
Figure 2.2 The geometry of (a) a zigzag ribbon and (b) an armchair ribbon, and the calculated band structure of (c) zigzag ribbons and (d) armchair ribbons of various widths. Taken from Ref. **[50]**

A band gap in graphene can be opened when the dimension of graphene is reduced. On the nanometer scale, the edge state becomes crucial for determining the electronic properties of graphene. In the "zigzag" edge (Fig. 2.2(a)) state, the charge density is strongly localized, while in the "armchair" edge (Fig. 2.2(b)) state, no charge localized state appears [50]. These two different edge states produce different band structures, as shown in Fig. 2.2(c) and (d), which shows the band structure of zigzag ribbons and armchair ribbons respectively. A band gap was seen in armchair nanoribbons with the condition of the number of dimer lines $N \neq 3M - 1$, where M is an integer [50]. It is notable that the width of ribbon affects the relative importance of the edge state and the orientation of ribbon affects the quantities of zigzag and armchair sites, both of which change the band gap as well as the band structure of graphene [50, 51].

On top of this bandstructure, the disorder at the ribbon edges in real devices introduces a further potential in graphene, making the band gap larger than for ideal graphene ribbons' [52, 53, 54]. The band gap of graphene ribbons with rough edges is inversely proportional to the ribbon width, as has been experimentally demonstrated, as shown in Fig. 2.3 [55]. According to these measurements, the band gap of a graphene ribbon and the ribbon width followed the relationship $E_{gap} = \alpha/(W - W^*)$, where E_{gap} was the energy of band gap, W was the width of ribbon, and α and W^* were fitting values obtained based on experimental data. Opening a band gap in graphene enables the realization of logic electronics and pinch-off of the current in graphene is then possible, thus also enabling quantum dots [56], for example, to be formed in the material.
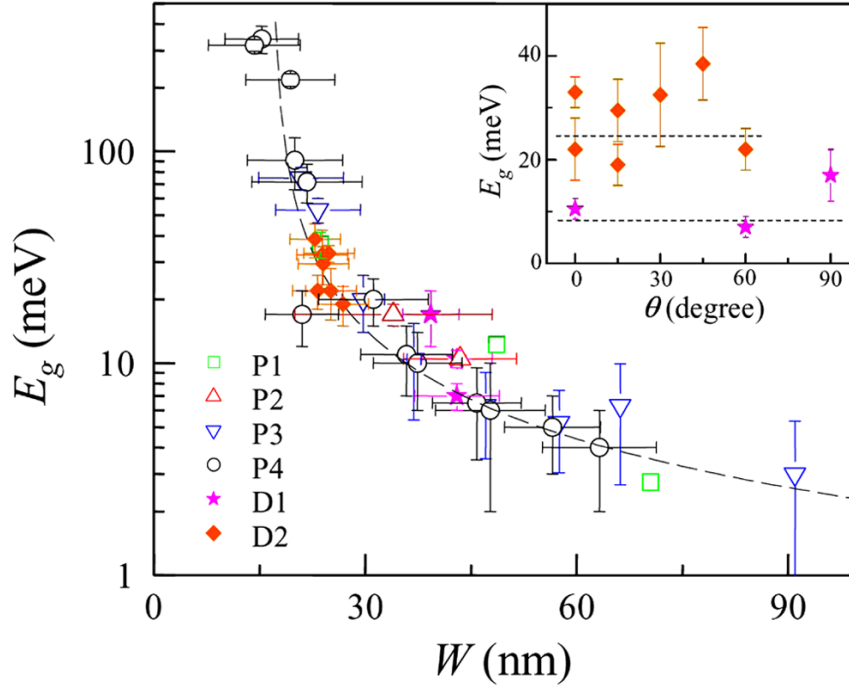
Figure 2.3 Energy of graphene ribbons' band gap as a function of ribbon width. Taken from Ref. **[55]**

2.2.2 Electrical properties

Graphene's ambipolar behaviour is such that the charge carriers in it can be electrically tuned between electrons and holes [1]. Close to the Dirac point, the density of states per unit cell is given by $\rho(E) = \frac{2A_c}{\pi} \frac{|E|}{v_F^2}$ [5, 57], where Ac is the unit cell area, calculated by $A_c = 3\sqrt{3}a^2/2$ with $a \approx 1.42\text{Å}$ being the carbon to carbon atomic distance. It can be clearly seen that the density of states vanishes when approaching the Dirac point, which makes the carrier density also approach zero. The carrier density in graphene can typically be tuned from 0 to $\sim 10^{13}$ cm^{-2} for both electrons and holes [1].

The transport mobility, μ, is an important parameter used to estimate the electronic quality of materials. The intrinsic electron-phonon scattering is the fundamental limit of charge carrier mobilities in perfect graphene, which limits the mobility of bulk graphene to be ~ 200 000 cm^2/Vs at room temperature [58, 59]. Other factors, including charge impurities, microscopic ripples, remote interfacial phonon scattering from the substrate, will further reduce the mobility. Graphene obtained by exfoliation can produce perfect single crystals, whose mobility has reached up to 230 000 cm^2/Vs, achieved in suspended graphene samples at 5 K [60], and 140 000 cm^2/Vs achieved by placing graphene on a boron nitride substrate at room temperature [61]. The boron nitride acts as an excellent substrate for graphene owing to its atomically smooth surface and its similar lattice constant to graphene, which reduces the charge trapes and the scattering. The polycrystalline nature of CVD-grown graphene increases the scattering rate, which results in the mobility typical one order of magnitude lower than that in exfoliated graphene, peaking at ~23,000 cm^2/Vs according to a wide range of experiments [62]. Interestingly, epitaxial graphene grown from decomposition of silicon carbide is heavily doped due to the charge transfer from the substrate, resulting in a strong metallic character though large electronic mobilities [5]. Up to now, the highest graphene mobility, exceeding 5, 000 000 cm^2/Vs, was achieved by using this kind of graphene with the dimensions smaller than the mean free path of carriers in it, in which case it acts as a ballistic conductor [63].

The Dirac like nature of the massless Dirac fermions in graphene results in the eigenenergies of Landau levels being

$$E_n = \sqrt{2eB\hbar v_F^2 |l|}, \quad l = 0, \pm 1, \pm 2, \cdots \qquad\qquad 2.3$$

where, e is the element charge, B is the magnetic field, and $\hbar$ is reduced Planck constant. It can be seen that there is a Landau level existing at zero energy, resulting in the existence of a minimum conductivity value corresponding to the quantum unit of conductance even when carrier concentration tends to zero. On top of this, the Landau level structure results in an anomalous quantum Hall effect that the conductance plateaus occur at half-integer values of the quantum of conductance. [11, 4] These two properties were demonstrated through early measurements on Hall bars soon after the first isolation of graphene, as shown in Fig. 2.4.
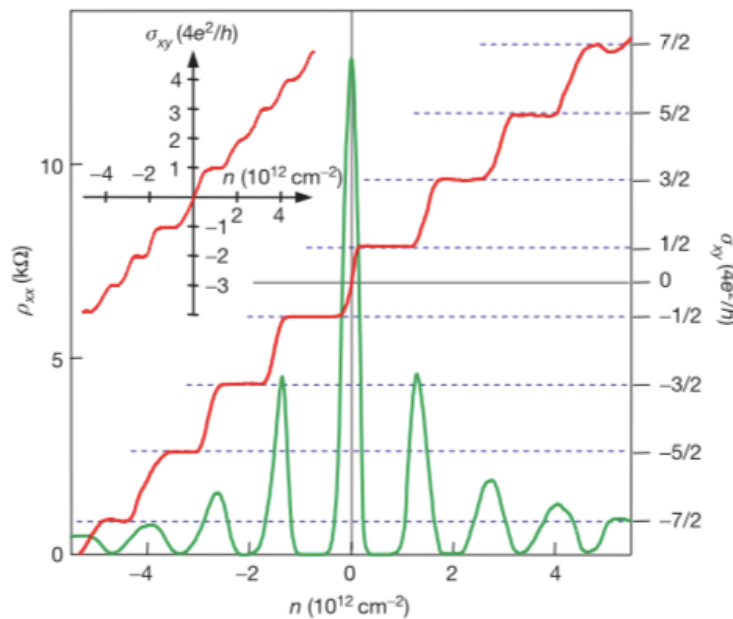
Figure 2.4 Quantum Hall effect for massless Dirac fermions in graphene measured by Hall bar method at B=14 T and T=4 K. Taken from Ref. **[4]**

2.3 Graphene's interaction with terahertz waves

2.3.1 The absorption spectrum of graphene
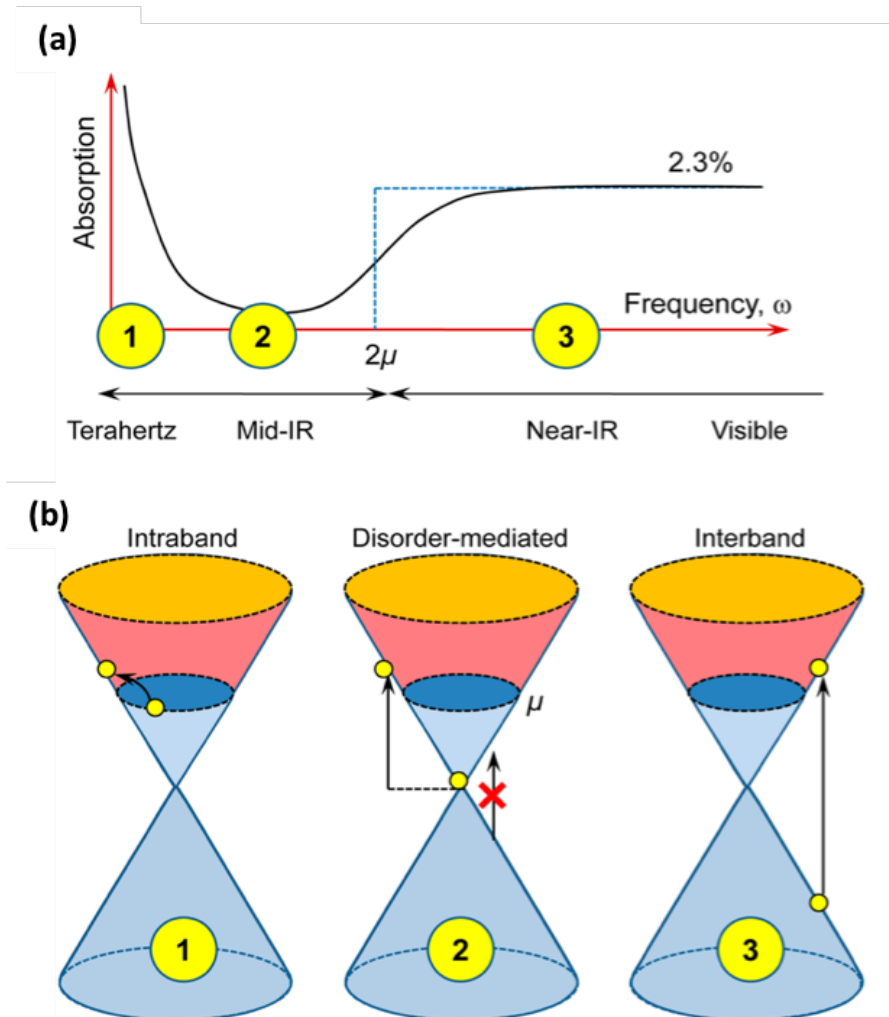
Figure 2.5 (a) A typical absorption spectrum of doped graphene ranging from terahertz waves to visible light, (b) Illustration of the optical transition processes in different optical bands. Taken from Ref. **[27]**

Graphene has a very broad optical absorption band, ranging from terahertz to visible wavelengths, as shown in Fig. 2.5(a) while the absorption mechanisms are dependent on a comparison of the energies between the

photons and the chemical potential, μ, as illustrated in Fig. 2.5(b) [27]. When the photon energy ($\omega\hbar$) is less than thermal energy ($k_B T$), the optical transition occurs via intra-band processes, and the absorption of the photons shows a frequency-dependent nature, which decreases with the frequency increasing, as shown in Fig. 2.5. It can be seen that the terahertz wave absorption does not change the carrier density of graphene. For photons of higher frequency, though still smaller than 2μ, the absorption is generally attributed to disorder [64]. When the photon energies are larger than 2μ, direct inter-band processes occur, which generates electron-hole pairs. In that case, there graphene exhibits a constant absorption of $\pi\alpha \approx 2.3\%$, where α is the fine-structure constant, 1/137 [65, 26].

2.3.2 Terahertz response of graphene

The optical conductivity of graphene in the terahertz band (0.1 - 10 THz) can be derived from Kubo's formula [25], which is given by:

$$\sigma_{intra} = i\frac{e^2/\pi\hbar^2}{\omega+i/\tau}\int_\Delta^\infty d\epsilon(1+\Delta^2/\epsilon^2) \times [f(\epsilon-E_F)+f(\epsilon+E_F)] \qquad 2.4$$

where, $f(\epsilon - E_F)$ is the Fermi distribution function, τ is the momentum relaxation time caused by intra-band scattering, and 2Δ is equal to the bandgap of graphene, which is zero in bulk graphene. The conductivity depends on the Fermi level which is tunable by electrical gating. In that case, photocurrents can be induced by a terahertz fields incident on the graphene, which has been experimentally demonstrated [66], showing promising potential for the fast room temperature detection of THz waves [67].

The wavevector of plasmon in graphene at terahertz frequencies can be calculated by [27]:

$$q(\omega) = \frac{\varepsilon_r}{2\alpha} \frac{\omega}{\omega_F} k_0 (1 + i/\tau\omega) \qquad\qquad 2.5$$

where, $\omega_F = E_F/\hbar$, ω is the frequency of plasmon and terahertz wave, $\alpha = 1/137$ is the fine-structure constant, and k_0 is the wavevector of terahertz wave in free space. Given that $(\frac{\varepsilon_r}{2\alpha} \frac{\omega}{\omega_F})$ can be calculated to be around 100 or larger., the plasmon wavevector in graphene is deduced to be two orders larger than the wavevector of terahertz wave in free space. Hence, THz wave can be coupled with graphene plasmons in graphene samples with dimensions much smaller than the THz wavelength, making it an attractive material for micro- THz devices. In graphene ribbons, plasmonic resonances occur for the conditions $q \approx (2n + 1)\pi/W$, where W is the width of ribbons. In that case, the plasmonic modes coupled into the graphene ribbons can be engineered, as has been experimentally demonstrated [68, 69].

2.3.3 Tuneable metasurfaces using graphene

Metasurfaces (2D metamaterials) are artificial structures, which are patterned on a two-dimensional surface, possessing engineered EM properties that do not commonly exist in nature. Such structures pave the way for new applications since they permit electromagnetic wave manipulation; examples of such applications are shown in Fig. 2.6 [34]. The subwavelength structural design of typical metasurfaces induce changes of spatial distribution (amplitude and phase) of incident EM waves. As a result

of that, new diffraction modes are created. The resulting reflection and refraction waves can be calculated by applying Fermat's principle [70].
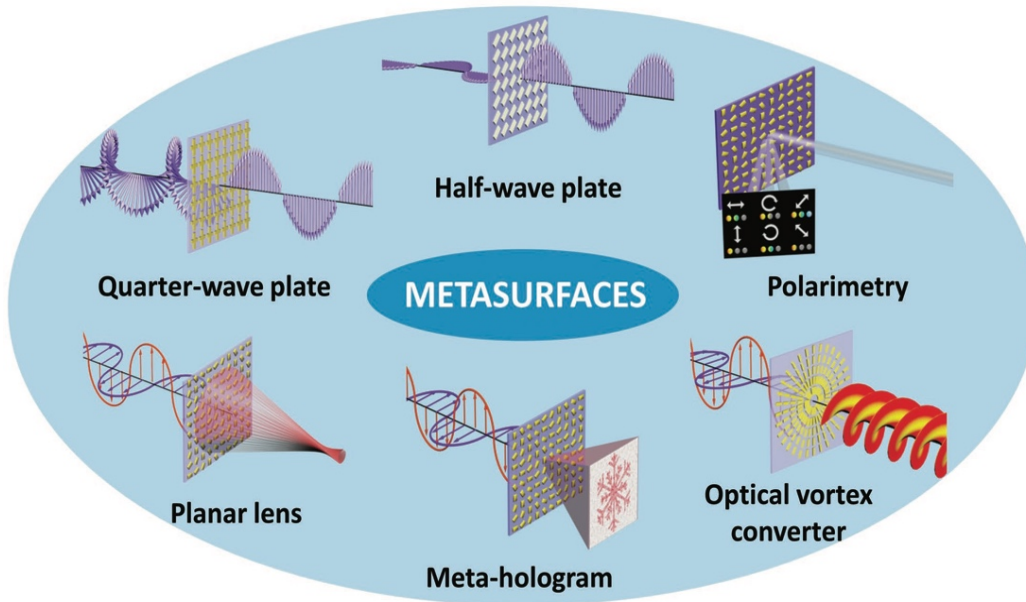
Figure 2.6 Possible applications produced from controlling and shaping electromagnetic waves using metasurfaces. Taken from Ref. **[34]**

Early metasurfaces were made from noble metals, which cannot be tuned once fabricated [71]. By contrast, graphene can be easily tuned by electrical gating at room temperature, which suggests that by introducing graphene into metasurfaces, the metasurfaces can then become capable of the dynamical control of phase and amplitude of electromagnetic fields. For this reason, graphene metasurfaces have received wide attention [41, 42, 43, 44].

There are two general ways to introduce graphene into metasurfaces. The first is by the direct replacement of the metal elements by graphene

structures [47, 72, 73, 74]. Since the carrier density and the conductivity can both be electrically modulated as discussed above, metasurfaces made from graphene structures are promising for tunable THz devices [47]. On the other hand, when lasers illuminate graphene, the inter-band transition process (Fig. 2.5(b)) generates electron-hole pairs, indicating that this kind of graphene metasurfaces can also act as optical modulated device [73].

The other way to create tunable THz controllers is to make hybrid graphene / metal metasurfaces [44, 75, 43]. In such geometries, graphene is coupled to the location of enhanced fields of the metal metasurfaces, sometimes known as "hot spots". Owing to the plasmon-induced local field enhancement through the graphene plasmon-THz wave coupling as discussed above, the graphene-metal hybrid structures can achieve large modulation of transmitted waves [44, 76].

2.4 Acoustoelectric effect in graphene

2.4.1 Surface acoustic waves interact with two-dimensional electron system

When a surface acoustic wave (SAW) propagates through a two-dimensional electron system (2DES) which is much smaller than the SAW wavelength, momentum is transferred from the SAW to carriers in the 2DES, so resulting in SAW intensity attenuation and velocity change. These changes can be calculated using the following equations [77]:

$$\Gamma = k \frac{K_{eff}^2}{2} \frac{\sigma_s/\sigma_M}{1+(\sigma_s/\sigma_M)^2} \qquad 2.6$$

$$\frac{\Delta v}{v_0} = \frac{K_{eff}^2}{2} \frac{1}{1+(\sigma_s/\sigma_M)^2} \qquad 2.7$$

where, σ_s is the sheet conductivity of the 2DES, σ_M is named critical conductivity defined by $\sigma_M = v_0(\varepsilon_p + \varepsilon_s)$ with ε_p and ε_s being the permittivity of the materials below and above the 2DES, respectively. These relations have been experimentally demonstrated [77, 78]. According to equation 2.6, the attenuation is associated with the sheet conductivity of the 2DES, indicating that the interaction strength between SAWs and 2DES can be modulated by means of changing the doping level of the semiconductor.

2.4.2 Acoustoelectric current in graphene

The momentum transferred from the SAWs to 2DES accelerates the carriers, inducing a current flow in the 2DES, called acoustoelectric current. The acoustoelectric current density is given by [79, 80]:

$$j = -\mu Q = -\mu \frac{I\Gamma}{v} \qquad\qquad 2.8$$

where, μ is the carrier mobility, Q is called phonon pressure, which can be calculated by $Q = I\Gamma/v$, with I the intensity of the SAW, Γ the attenuation obtained from formula 2.6, v the SAW velocity. This theory can also be applied to graphene AE devices.

According to formula 2.6, a peak value of attenuation should appears when $\sigma_s = \sigma_M$, also indicating a peak AE current generated when this condition is met [81]. According to formula 2.8, the AE current is proportional to the SAW intensity, in agreement with the experimental findings [82]. It is notable that the SAW acts as a moving periodic potential in the process of AE effect that effectively traps carrier in the 2DES traveling with it in its

"washboard" potential. In that case, the carriers are always transported in the same direction as the propagating direction of SAW, no matter whether the carriers are positively or negatively charged. Due to the ambipolar transport properties of graphene, both the amplitude and the direction of AE current in graphene can therefore in principle be tuned by electrical gating. Especially, in CVD grown graphene, a nonlinear relationship between the SAW intensity and the AE current was seen at low temperature when the SAW frequency was around 30 MHz or lower, as shown in Fig. 2.7 [83]. The reason is that the graphene's conductivity is strongly affected by electron-hole charge puddles, and the percolation of thermally excited carriers over potential fluctuations in disorder sites played an important role in the conductivity [84]. SAWs with longer wavelength were more sensitive to the component of the conductivity caused by percolation, owing to their length scales then being more commensurate.

Since many factors, such as photoexcitation [85], chemical doping [86], and temperature [87] will change the properties of graphene, inducing an change in the response of AE device consequently, graphene AE devices have the potential to operate as versatile sensors [88, 87, 86, 89].
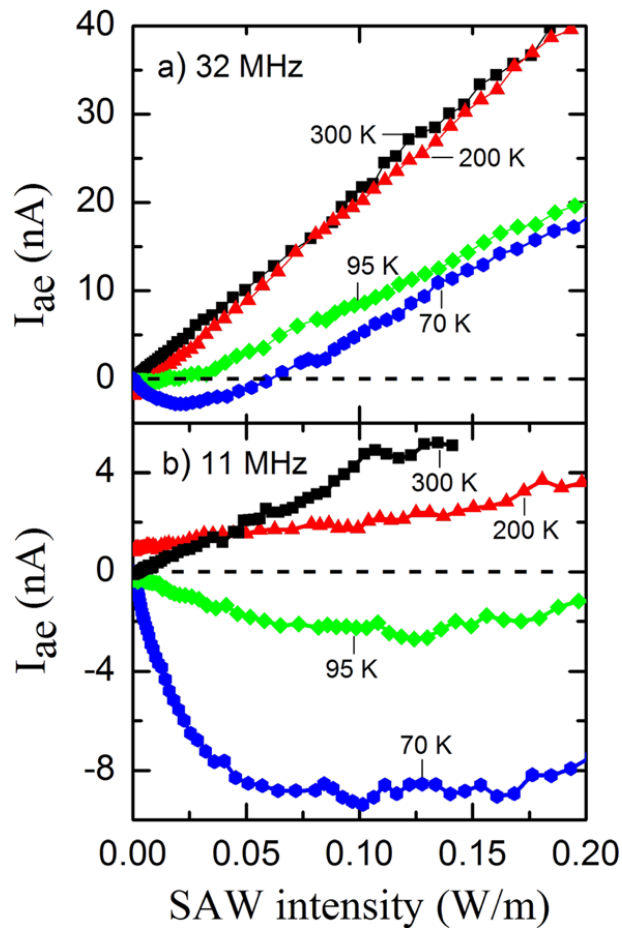
Figure 2.7 AE current generated by (a) 32 MHz and (b) 11 MHz SAW at low temperature as a function of SAW intensities. Taken from Ref. **[83]**

2.5 Conclusion

The theoretical background around this project was introduced. The theories of band structures and electronics of graphene were first briefly introduced in so far as they are needed later on. Then, the interactions between graphene and terahertz waves were discussed, including the carrier transition processes, conductivity and plasmons in bare graphene, which provides the basis for graphene THz devices such as THz detector and THz modulator (relevant to the researches in chapter 5). After that, the principle

of metasurfaces (relevant to chapter 4) and especially tunable metasurfaces based on graphene (relevant to the graphene-metasurface hybrid THz polarizer in chapter 5) were introduced. Lastly, the principle of the acoustoelectric effect in graphene was discussed and some special features which make it different from conventional 2DES were discussed, which will be used in discussion within chapter 6.

Chapter 3 Key technologies used in this project

3.1 Chapter introduction

This chapter discusses some technologies that will be utilized in the following chapters, including: graphene transfer, Raman spectroscopy, terahertz time-domain spectroscopy, and surface acoustic wave delay lines. These works make a preparation for the device fabrication and data acquisition in the following chapters.

3.2 Graphene transfer

Graphene grown by chemical vapor deposition has been widely used for electronic applications owing to it being a reliable growth process, offering relatively large area coverage with good quality obtainable [90, 91]. Low-cost metals with low carbon solubility, such as copper (Cu) and nickel (Ni), are usually employed as substrates for growing graphene by CVD [92]. Comparing these two metals, Ni is more suitable for producing multi-layer graphene since it is an active catalyst for the decomposition of the hydrocarbon bond in the methane used for graphene film growth, while Cu is suitable for producing single-layer graphene owing to its weak catalytic action on methane [93]. On top of that, large-area graphene films on copper have been produced using the "roll-to-roll" method [19], making copper the most widely used metal substrate for commercial production of graphene

films. The graphene samples used in this project were CVD-grown single-layer graphene on copper purchased from Graphene Supermarket.
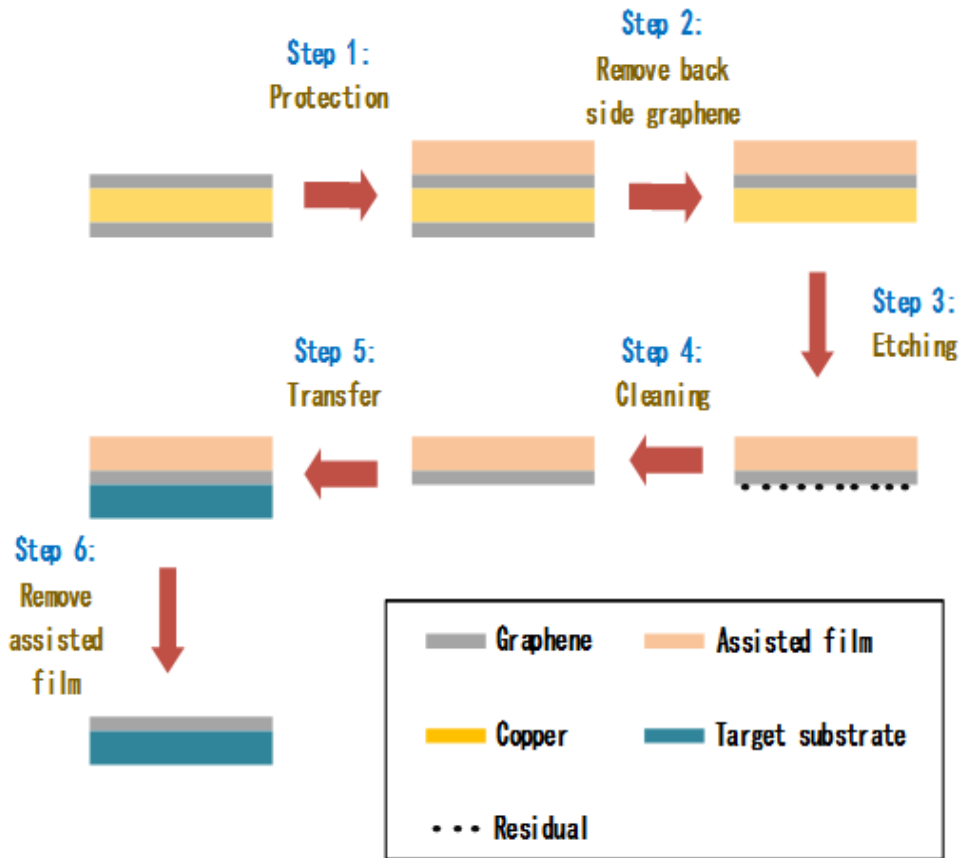
Figure 3.1 Procedure for transferring CVD grown graphene onto an arbitrary substrate, which was the internal recipe in our group developed by Nicholas Hunter.

As shown in Fig. 3.1, and discussed in more detail in the following section, CVD grown graphene is typically transferred on to arbitrary substrate for device fabrication using the following six steps: (1) spin a polymer on to the graphene for protection, (2) remove the graphene on the reverse side of the copper film, (3) etch the copper layer, (4) clean the graphene sample, (5)

transfer the graphene onto the target substrate, and (6) remove the assisted polymer film. This overall recipe, which was the internal recipe in our group developed by Nicholas Hunter, was used for fabricating all the graphene devices in this project.

As shown in Fig. 3.1, the first step is to adhere assisted polymer layer on to the target graphene, with the aim of protecting the graphene during the process of transferal. Although some works have omitted this step [94], protection is still the standard procedure used for graphene transfer to increase the success rate. Several materials, including spin coated poly-(methyl methacrylate) (PMMA) [95, 96], polydimethylsiloxane (PDMS) [97], and thermal release tape [98], have each shown good performances for graphene transfer. In this project, PMMA was utilized owing to the simplicity of coating and lack of residues left on the graphene [99].

After removing the backside graphene (which is extraneous to most experiments), using a gas plasma (step 2 in Fig. 3.1), the copper layer is then etched using a copper etching solution (step 3). There are several optional solutions to choose from, including $FeCl_3$, $Fe(NO_3)_3$, $(NH_4)_2S_2O_8$, and H_2O_2.aqua Regis.H_2O. Compared with the first of these three solutions, H_2O_2.aqua Regis.H_2O showed the fastest etching speed [100]. Step 4, cleaning, is aimed to remove residues underneath the graphene sample. Deionized (DI) water can be used for rinsing the polymer/graphene film, while, the "modified RCA (Radio Corporation of America) clean" methodology has demonstrated a better measure regarding improving the cleaning efficiency of metal contamination [101]. After this, the graphene sample then

floating on the surface of DI water is pulled up using the target substrate and left to rest for drying (step 5). These four steps should be performed with great care with care for the fragile graphene and copper films, to avoid unwanted residual material, wrinkles, and cracks appearing, all of which will significantly reduce the performance of the sample.

The final step of the graphene transfer recipe is removal of the protection film (PMMA in our case). The most common method for removing PMMA is rinsing in acetone. However, this method can leave residues on the graphene, which causes carrier scattering so degrading the sample quality [102]. Some efforts have been made to enhance the removal of the PMMA, such as thermal annealing [96], double-PMMA-layer enhanced removal [99], and electron beam induced removal [103]. In this project, the double-PMMA-layer method was used for bulk graphene device since it is easy to accomplish and suitable for large graphene samples; while the electron beam method was used for graphene nanoribbon devices since better quality electronic graphene samples could be obtained by using this method.

3.3 Raman spectroscopy

Raman spectroscopy is a powerful spectroscopic tool to characterize the interactions of electrons and phonons in graphene [104]. The Raman effect, named in honor of the discoverer [105], refers to a scattering process in which the energy and momentum of photons incident on materials are different from those of the scattered photons. The differences depend on the bandstructure of the material. Raman spectroscopy is the spectroscopic technique based on the Raman effect, which identify the materials by

investigating the momentum or energy shift between incident photons and scattering photons. Several distinct peaks, referred to as the D, D', G, G*, 2D, 2D', D+D' peaks, may appear in the Raman spectra for graphene [106, 107, 108, 109]. The G peak and 2D peak, locating at around 1580 cm^{-1} and 2700 cm^{-1}, respectively, constitute the characteristic spectra for graphene, whose position, shape, and relative intensity vary with the number of layers, and doping level. For single layer graphene, the intensity of 2D peak is significantly larger than the intensity of G peak. The defect-induced D peak is located at around 1350 cm-1, and it reflects the defects [110] and carrier density [111] in graphene.

In this project, Raman spectroscopy was utilized to confirm the identity of graphene in devices. It is noted that the substrates chosen for devices may also possess Raman peaks in the range of 1200 cm^{-1} to 3000 cm^{-1}, which will then affect the graphene spectra located in the same range. Quartz was used as the substrate for the graphene devices fabrication in chapter 5, while lithium niobate ($LiNbO_3$) was used as the substrate for the graphene devices fabrication in chapter 6. In order to distinguish the Raman spectra on graphene in both cases, it was therefore sometimes necessary to record additional spectra of the uncoated substrates to perform background subtraction.

Fig. 3.2(a) and (b) give the Raman measurement results of graphene samples on quartz and $LiNbO_3$, respectively. The solid red lines are the Raman signals of the substrates. As can be seen, the Raman signal of quartz is much smaller than graphene's, while the intensity of the Raman

spectra for LiNbO$_3$ was comparable to that of graphene. In that case, the Raman spectra of graphene on quartz could be used directly as indicative of graphene's signal, as shown in Fig 3.2(a), in which the signal of graphene and the signal of graphene/quartz overlapped. On the other hand, the signal of graphene located on LiNbO$_3$ should be obtained by subtracting the graphene/LiNbO$_3$ signal with LiNbO$_3$'s signal (Fig 3.2(b)). The intensity of 2D peak was 2~3 times larger than the G peak, indicating that single-layer graphene was located in the area of the substrate tested.
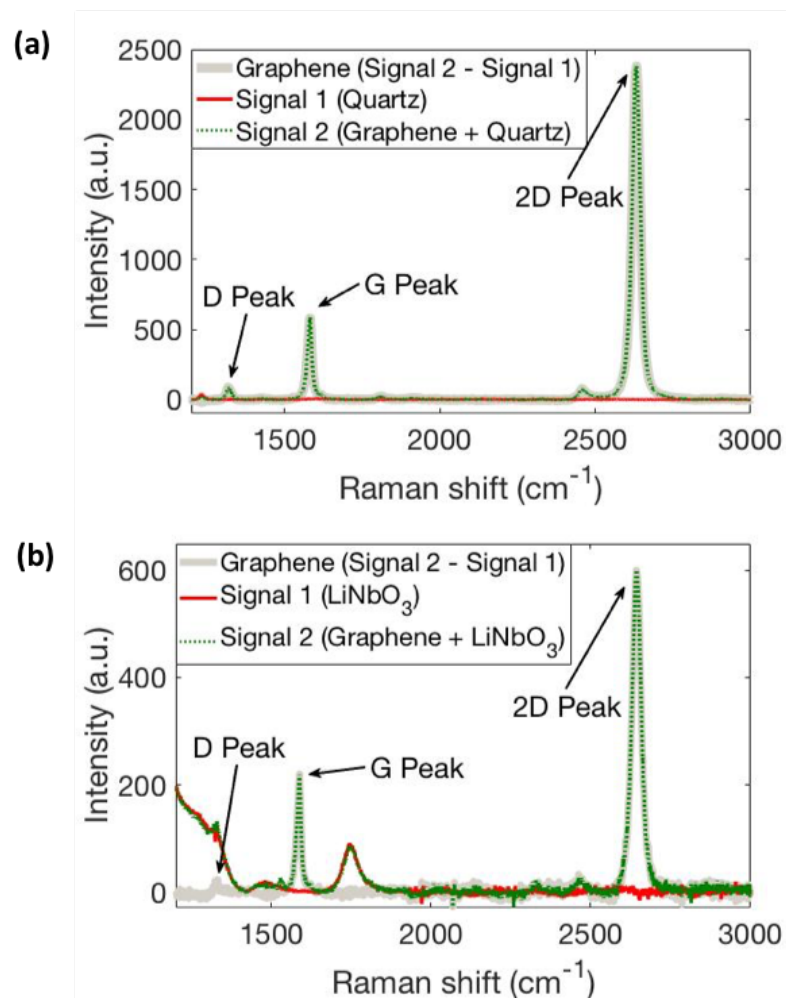
Figure 3.2 Raman spectra of graphene on the substrates of (a) Quartz and (b) LiNbO3, in which the graphene signal (grey line) was taken as the difference of the two experimental data (signals 1 and 2).

3.4 Terahertz time-domain spectroscopy

Terahertz time-domain spectroscopy (THz-TDS) is a spectroscopic technique based on a femtosecond (fs) laser pumped THz pulse emitter and detector [112]. Various emitters and detectors have been utilised for THZ-TDS, including those based on photoconductive (PC) antennae [113], electro-optical crystals [114], air plasmas [115], and the photo-Dember effect [116]. Both the real part and the imaginary part of materials' frequency-dependent optical constants in the THz band can be obtained simultaneously by THz-TDS without recourse to Kramers-Kronig analysis, meaning that THz-TDS is now widely used in many fields of physics, materials sciences, engineering, chemistry, and biomedicine [112, 117].

Both THz pulse emitter and detectors used for the THz-TDS performed in the course of this project were based on low-temperature-grown gallium arsenide (LT-GaAs) PC antennas. A diagram of a typical THz-TDS system is shown in Fig. 3.3. A mode-locked Ti:sapphire laser operating at a 80 MHz repetition rate was used to provide 20 fs pulses with a central wavelength of 800 nm. This laser was split into two beams by a beam-splitter, with one path then made to be incident on the THz emitter acting as the pump beam, while the second path was focused on to the THz detector (a second PC LT-GaAs structure) to act as the probe beam. Electron–hole pairs generated in the antenna gap area of the emitter by the incident photons were accelerated under the biased electric field, and, consequently, an electromagnetic wave was then generated by these accelerating charges. The carrier lifetime of the LT-GaAs is an important factor for determining the duration of the generated

EM wave, which is typically on sub-picosecond timescales. The THz pulses were then guided by off-axis parabolic mirrors into the antenna gap of the THz detector. When the detector was illuminated by the probe beam and THz wave at the same time, a current was generated owing to the photoexcited carriers accelerated by the THz electric field coincident with the probe fs laser, which is proportional to the amplitude of THz wave and could be record using a lock-in amplifier. By tuning the time-delay between the THz pulse and the probe using a retroreflector on a translation stage, the time-resolved profile of the THz pulse was obtained. This kind of THz-TDS setup with PC antennas as the THz generator and detector were taken for the THz experiments in chapter 4 and 5.
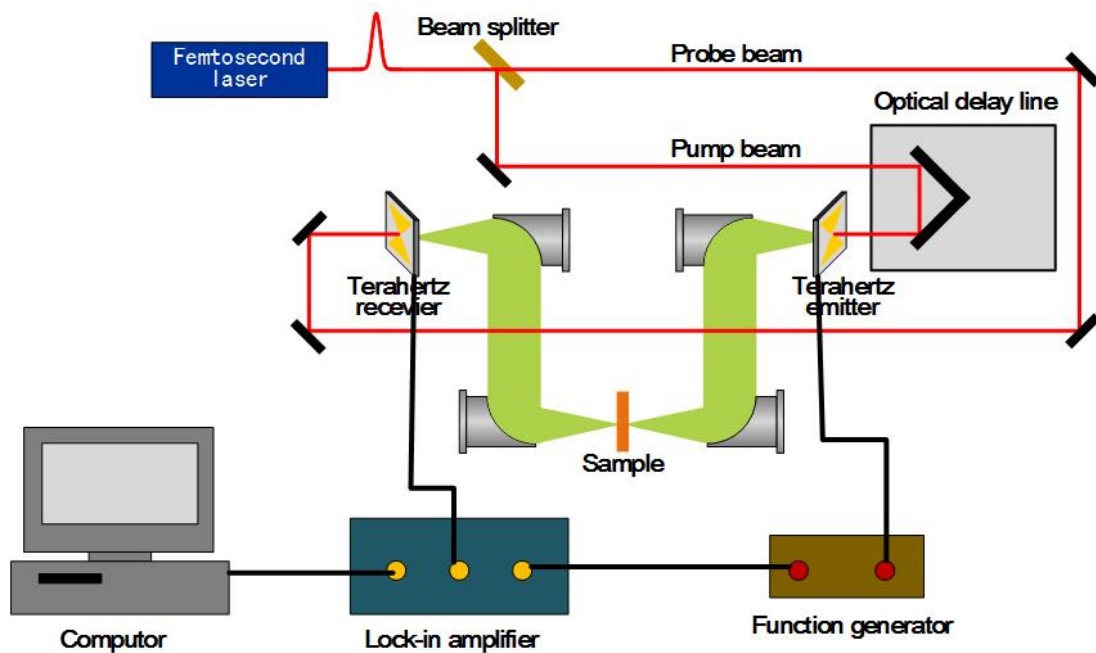
Figure 3.3 Diagram of THz-TDS system based on the PC antenna THz emitter and detector.

Frequency-dependent information contained in the THz pulse can be obtained from these time-domain signals by using Fourier transformation. To obtain the THz response of samples, two THz time-domain traces are needed: one is obtained by the THz-TDS without sample in the beam path, (the "reference" THz signal), while the other is obtained by the same THz-TDS but with a sample in the path of the THz beam, then named the "signal" THz pulse. The differences between these two pluses are determined by the THz properties of the sample, which can be obtained mathematically by comparing the frequency-domain information of the reference THz pulses and the signal THz pulses [112].

3.5 Surface acoustic wave delay lines

Surface acoustic waves, which were first described by Lord Rayleigh in 1885 [118], refer to a mode of acoustic propagation along the surface of elastic materials, and comprise both longitudinal and vertical shear components, whose amplitude decays exponentially with depth into the substrate. The generation of SAWs by electronic methods involves combining interdigitated transducers (IDTs) with piezoelectric crystals [119], which historically opened up a wide application fields for SAWs, including their use in filters [120], oscillators [121], and transformers [122].

The geometry of a typical IDT is shown in Fig. 3.4. The IDT is made from a highly conductive material, typically metal, though graphene has also been shown by our group to work too [123]. When an oscillating voltage is applied to the two electrodes of the IDT, an oscillating strain wave is applied to the substrate underneath owing to the piezoelectric effect, which launches SAWs

in both directions perpendicular to the fingers. The wavelength of the excited SAWs can be calculated by $\lambda_{SAW} = v_{SAW}/f$, with f the frequency of the oscillating voltage. If the wavelength of the IDT, λ as shown in Fig. 3.4, is equal to the wavelength of SAWs, λ_{SAW}, every IDT finger is phase matched, with the intensity of their generated SAWs being efficiently superimposed. Because of this, the geometry of IDT should match with the frequency of the oscillating voltages. The detection of SAWs is the reverse process of generation based on similar considerations.
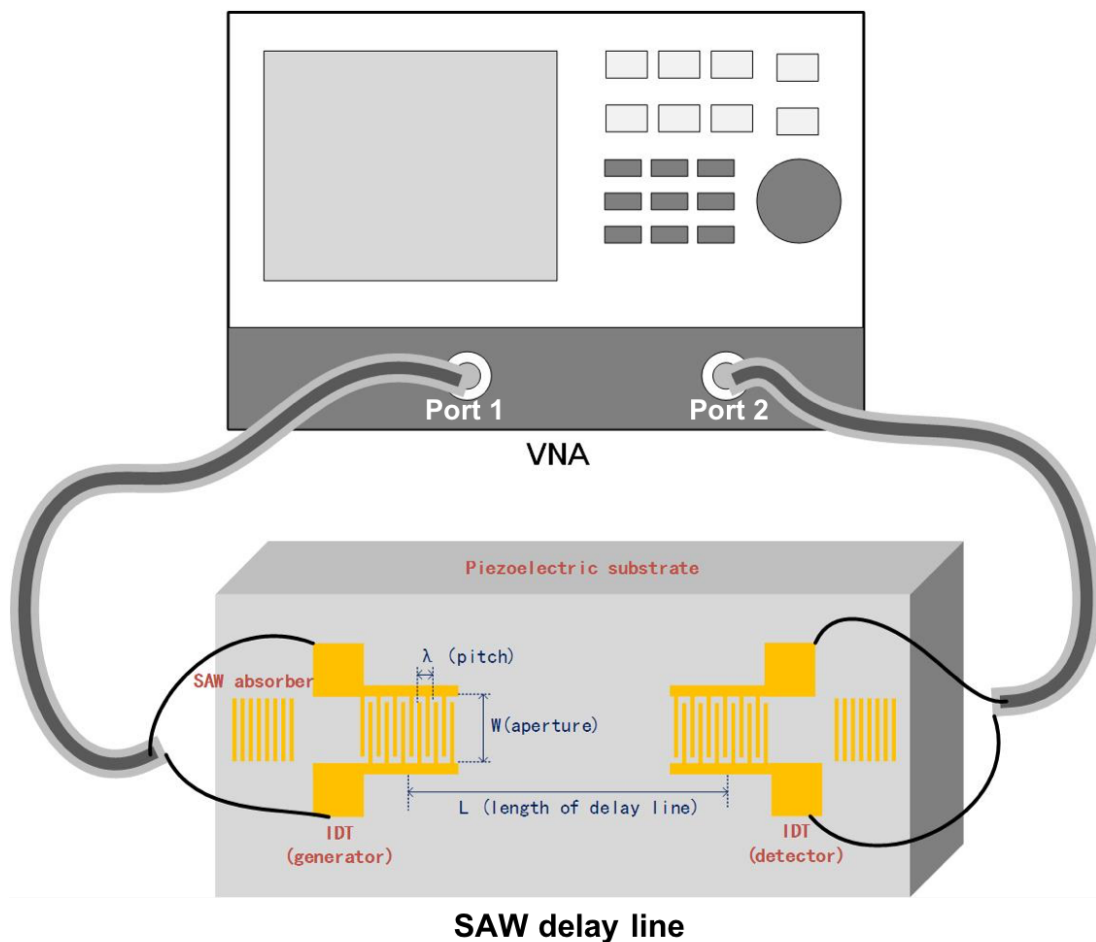
Figure 3.4 Diagram of SAW delay line testing, in which the key parameters of the SAW device are illustrated.

The SAW delay lines were tested using a network analyzer (Agilent E8364B), with the testing system illustrated in Fig. 3.4. Coaxial cables were used to transmit the RF signals into and out of the network analyzer. The SAW delay lines were connected to the coaxial cables through SMA connectors, which were conducted with IDTs by ball bonding. Chip holders for MHz devices were PCB board as shown in Fig. 3.5(a), and for GHz devices were aluminium mounts as show in Fig. 3.5(b).
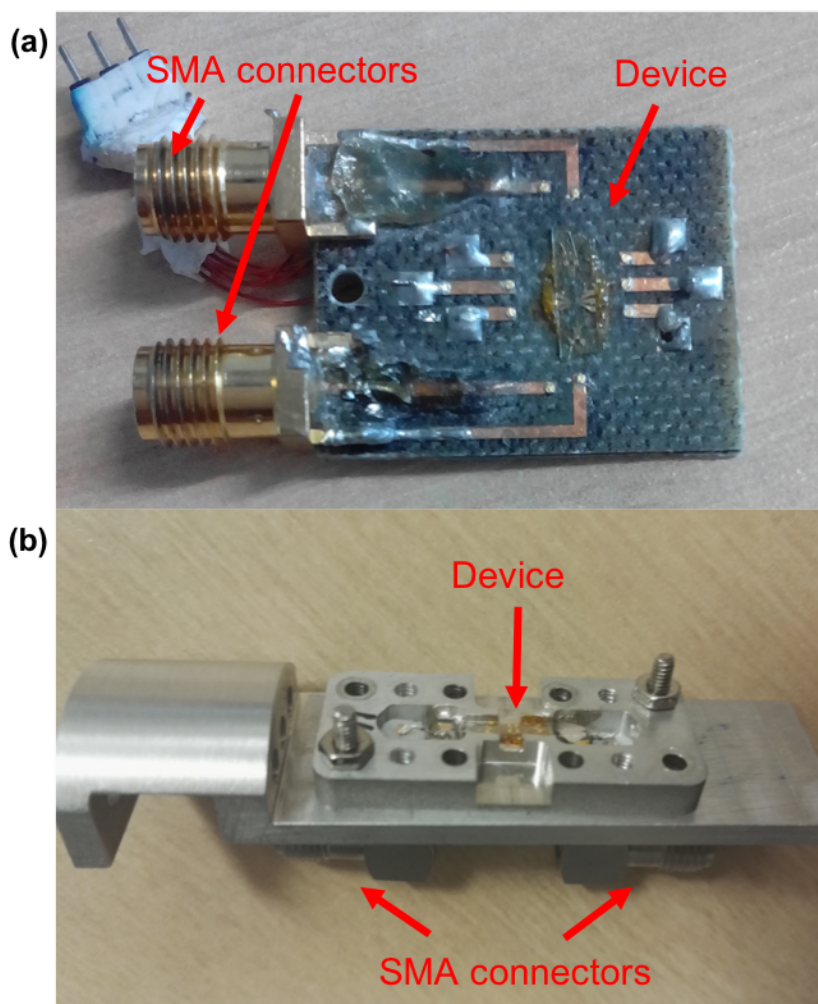
Figure 3.5 (a) PCB board used for MHz SAW delay line measurements, (b) Aluminium mount used for GHz SAW delay line measurements.
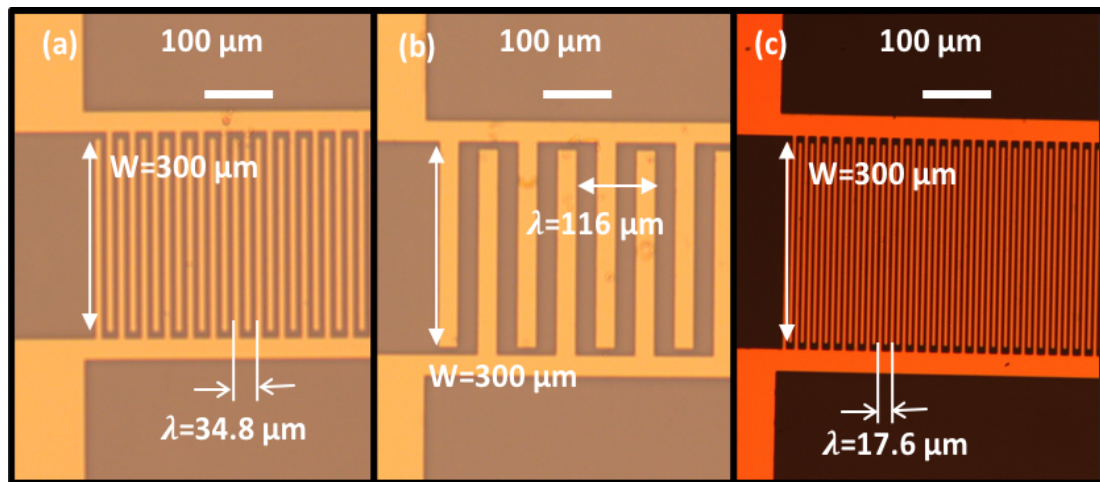
Figure 3.6 Microscopic images of IDTs with the wavelength of (a) 34.8 μm, (b) 116 μm, and (c) 17.6 μm.

The fabrication of a SAW delay line, which contains two separate IDTs, follows standard microfabrication procedures. Optical lithography (OL), or named photolithography, was used for patterning the devices with operating frequencies below 500 MHz. The details of the recipe were as follows: Firstly, a layer of S1813 photoresist was spun on $LiNbO_3$ at 4000 rpm for 40 s and baked at 115 degree Celsius (℃) for 120 s. Then it was patterned employing OL, rinsed in the chlorobenzene for 2 min, and developed in MF319 for 1 min. After that, ohmic contacts were formed using Cr/Au (7nm / 70 nm) using evaporator. Finally, the pattern was lifted off in acetone for more than 4 hours. Fig. 3.6 shows microscopic images of IDT fingers of the fabricated devices with the dimensions as shown in table 3.1, in which λ is SAW wavelength, W is the width of the acoustic aperture, L is the distance between two IDTs measured from the center of on IDT to the center of the other one, and N_p is the number of electrode pairs, all of which were

illustrated in Fig. 3.4. According to the wavelength of the IDTs, the resonant frequency of the SAWs can be calculated; it is 114.8 MHz for device 1, 34.4 MHz for device 2 and 227 MHz for device 3.

Table 3.1 Parameters of SAW delay lines patterned using OL

Parameters	Device 1	Device 2	Device 3
λ (µm)	34.8	116	17.6
W (µm)	300	300	300
L (mm)	1.8	2.1	2.7
Np	13	10	40
Theoretical $f_{resonant}$ (MHz)	114.8	34.4	227.1
Experimental $f_{resonant}$ (MHz)	110.3	33.2	217
Theoretical bandwidth (MHz)	17.7	6.9	11.4
Experimental bandwidth (MHz)	18.1	5.3	10.6
S12 (dB)	-20.2	-38.5	-7.2
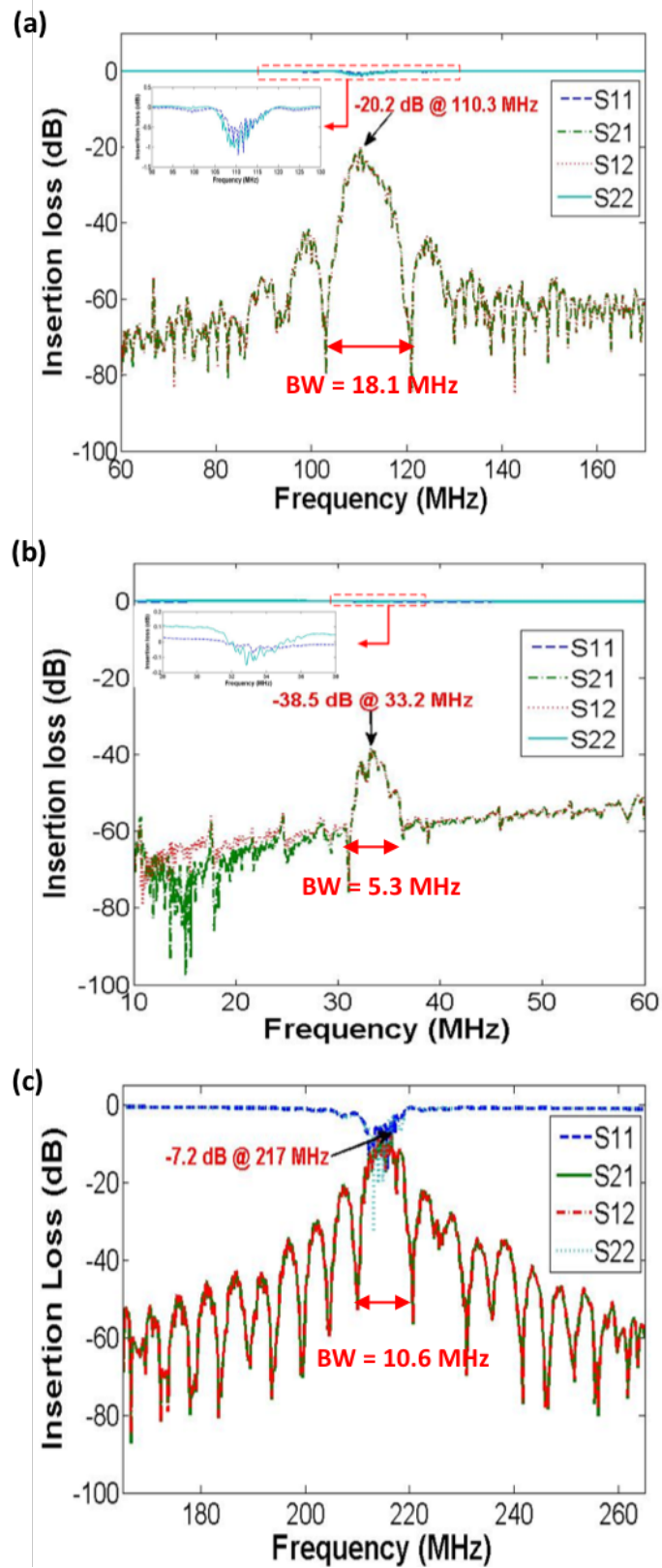
Figure 3.7 Response of SAW delay lines formed on lithium niobate of (a) device 1, (b) device 2, and (c) device 3.

The measurement results are shown in Fig. 3.7, in which S11 and S22 are used to estimate the reflection properties of IDT1 and IDT2, respectively, and S12 and S21 are used to estimate the transmission properties from IDT1 to IDT2 and from IDT2 to IDT1, respectively. The transmittance insertion loss, S21 and S12, for device 1 at the resonant frequency was -20.2 dB. The central frequency was 110.3 MHz, similar to the theoretical expectation (114.8 MHz). The insertion loss for device 2 was -38.5 dB at the frequency of 33.2 MHz, which was close to the calculated value 34.4 MHz. The higher loss in device 2 was accounted for by its larger divergence angle, caused by diffraction induced by the longer wavelength [124]. The transmission S21 of device 3 at the resonant frequency was -7.2 dB and the central frequency is 217 MHz, comparing well with the theoretical value of 227.1 MHz.

The form of the transmission versus frequency showed the characteristic sin(x)/x behavior typical of SAW transducers [125]. The bandwidth of the SAW delay lines, as illustrated in Fig. 3.7, can be calculated by $BW = (2 \cdot f)/N_p$, where f is the central frequency of IDT, and Np is the number of finger pairs. Thus, the bandwidth of these three devices was calculated to be 17.7 MHz, 6.9 MHz, and 11.4 MHz, respectively. The experimental results of the minimum-to-minimum bandwidth of these three devices were 18.1 MHz, 5.3 MHz, and 10.6 MHz, respectively, close to the theoretical predictions.
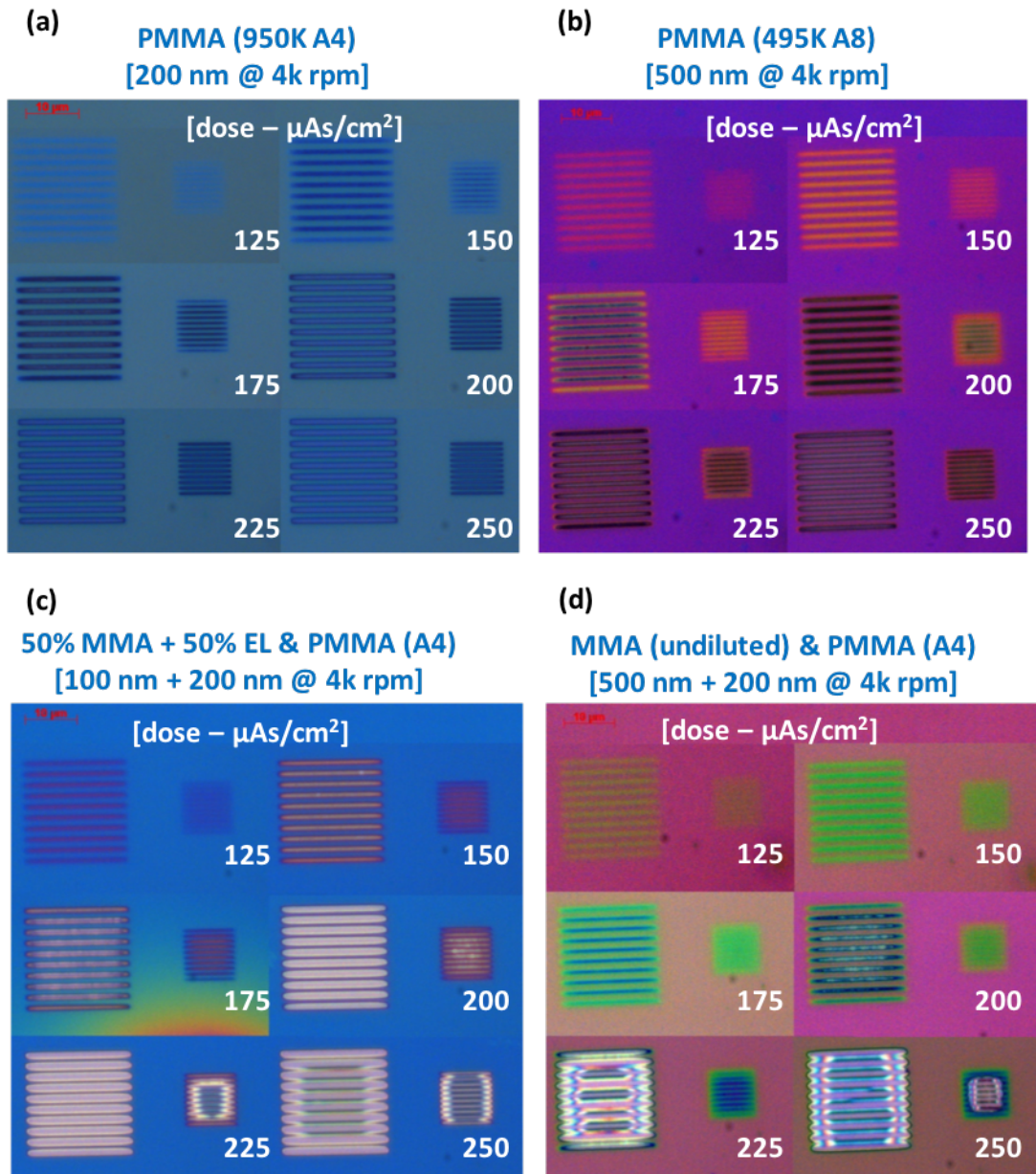
Figure 3.8 EBL dose test for 4 µm-wavelength IDTs by using the resist layer of (a) 200 nm PMMA (950K A4), (b) 500 nm PMMA (495K A8), (c) 100 nm 50% diluted MMA / 200 PMMA (A4), and (d) 500 nm MMA / 200 nm PMMA (A4).

For patterning devices with operation frequencies higher than 500 MHz, electron beam lithography (EBL) was needed since the finger width of IDTs

was smaller than 2 μm, which surpassed the resolution of the OL techniques being used. Dose tests were needed before fabrication of real devices since the dose varies with the dimensions, substrate and resist chosen. Fig. 3.8 shows a typical dose test used for the fabrication SAW delay line with 4 μm wavelength (1 μm finger width) on LiNbO$_3$. By comparing the patterning quality and considering the lift-off, the 500 nm PMMA (495K A8) with the exposure dose of 250 μAs/cm^2 was chosen for subsequent device fabrication.
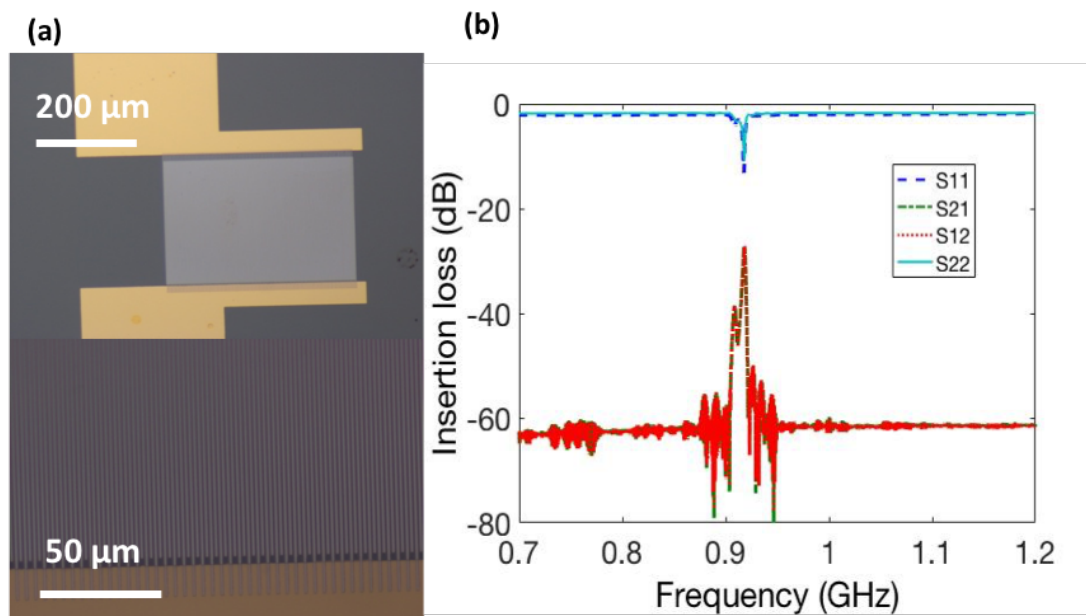
Figure 3.9 (a) Micrograph of fabricated ~1 GHz IDT, where the upper frame is an overview of the IDT, and the under frame is a closeup view of the fingers. (b) The response of the 4 μm-wavelength SAW delay line.

Images of fabricated 4 μm-wavelength IDTs are shown in Fig 3.9(a), which were then tested using a network analyzer obtaining the results shown in Fig. 3.9(b). The peak transmittance (insertion loss) of this device at its

resonant frequency was found to be -27.15 dB. The central frequency was 918 MHz, which was similar to the theoretically calculated results, 910 MHz. The number of finger pairs Np of this device was 100, determining the theoretical minimum-to-minimum bandwidth to be 18.2 MHz, which was agreed well with the experimental value of ~17.8 MHz.

3.6 Conclusion

Key technologies that will be utilized in the following chapters were discussed. A graphene transfer method was chosen and shown to produce single-layer graphene. The identification of graphene layers on piezoelectric substrates using Raman spectroscopy was discussed. THz-TDS systems used in chapter 4 and 5 were introduced. Techniques for SAW delay-line fabrication and testing were examined. These measurements and techniques provide the preparations for the research discussed in the following chapters.

Chapter 4 Increasing the sensitivity of THz metamaterials for dielectric sensing

4.1 Chapter introduction

Metamaterials are composed from artificial subwavelength elements, referred to as "meta-atoms", arranged into periodic or quasi-periodic structures, whose interaction with electromagnetic waves can be tuned through their geometry [126, 127, 128, 129, 130, 131]. Substances placed on or near metamaterials dominate the interaction between EM waves and the metamaterials. On top of that, by engineering the geometry of the metamaterials, physical quantities such as the components of electric field or magnetic field that the metamaterials are sensitive to and the operating frequency can be determined, allowing sensing applications to be developed [132, 133]. Metamaterial absorbers, meaning the metamaterials that have significant resonant absorption frequencies on EM waves, are potentially useful in sensing applications, since a strong and easy-measurable signal can be produced owing to the strong resonances between the meta-atoms and the EM waves [134]. Various resonances such as the inductive-capacitive (*LC*) resonance [135, 136], dipole resonance [137], and quadruple resonance [138] can be employed for the elements designs, whereby surface

current modes are strongly excited on interaction with the incident electromagnetic radiation.

Split-ring resonators, which have received particular attention [139, 140, 141], are particularly attractive in the context of sensing applications since the presence of dielectric materials in the gap area directly induces an absorption frequency shift [142, 143, 144, 145]. The resonant frequency of the *LC* resonance in SRRs can be described by $1/2\pi\sqrt{LC}$, where C is the capacitance of the gap and *L* is the inductance of the ring [146, 147]. The effect of various geometrical parameters, including gap width, metal thickness, and substrate index on dielectric sensing using THz metamaterials have been explored in some detail [148, 149, 150]. Recent examples of sensing using SRR arrays include the detection of low-density nano/microscale microorganisms [126, 151].

A noteworthy enhancement of the sensitivity was recently obtained by substituting high-index substrate materials (such as silicon) for lower-index materials (such as quartz) [151]. We could take the formula $f = 1/2\pi\sqrt{LC}$ to understand the sensitivity enhancement. The capacitance can be calculated by $C = \varepsilon_{eff}A/d$, where A is the area of the capacitor's two plates and d is the distance between them. Effective dielectric constant can be calculated by $\varepsilon_{eff=\alpha\cdot\varepsilon_{substrate}+\beta\cdot\varepsilon_{up}}$, in which α and β are constant depending on the geometry of the metamaterials, $\varepsilon_{substrate}$ is the dielectric constant of the substrate, and ε_{up} is the dielectric constant of the materials on top of the substrate. In order to act as dielectric sensor, what we would obtain is the frequency shift between the resonant frequencies when the upper materials

are air and measured materials, respectively. Take f_{air} and $f_{material}$ are the resonant frequency without measured material and with material, respectively, thus, $f_{air}^2 - f_{material}^2 = \frac{d}{4\pi^2 LA}$. $\frac{\beta \cdot \varepsilon_{material} - \beta \cdot \varepsilon_{air}}{(\alpha \cdot \varepsilon_{substrate} + \beta \cdot \varepsilon_{air}) \cdot (\alpha \cdot \varepsilon_{substrate} + \beta \cdot \varepsilon_{material})}$, from which we can see that a lower substrate index, $\varepsilon_{substrate}$, leads to a larger frequency shift.

Based on the analysis above, an effective method to enhance the sensitivity is to reduce the substrate's index. Our idea is to introduce a trench structure in the capacitor area of the metamaterials, which means we replace the high-index substrate material with low-index air, which would significant improve the sensitivity of the metamaterials.

In this chapter localized etched trenches in the LC gap area of SRRs were introduced to enhance the sensitivity of the SRRs acting as terahertz dielectric sensors. The reason to etch the substrate in the capacitor area is that the dielectric constant used in formula $C = \varepsilon_{eff}A/d$ is the effective dielectric constant between the two plates. The whole LC gap would be etched to obtain significant sensitivity enhancement. Different etching depth would be tested to reveal the rule of sensitivity changing. After carefully design and reactive ion etching (RIE), THz SRRs with various depths of trenches were tested using a transmittance THz-TDS setup. The THz response properties of the etched SRRs were first measured, and then the sensitivity enhancement produced by the etching to overlaid dielectric materials was examined both through experiments and in simulations. It is demonstrated that a sensitivity enhancement by a factor of up to ~2.7 times can be obtained, and the mechanism for the enhancement is discussed.

4.2 Experimental methods

4.2.1 SRRs design and fabrication

A schematic diagram of the metamaterial arrays incorporating the etched regions, along with the periodicity of the unit cells is shown in Fig. 4.1(a). The metamaterials are designed to be split-ring resonators structures, employing a metal track width of 4 μm, with outer element dimensions of 36 μm × 36 μm, and periods of 50 μm in orthogonal directions; the LC gap size was chosen to be 2.7 μm. As discussed later, this choice of geometry produced a strong LC resonance at ~0.79 THz before etching. The etched region was located in the LC gap area and in the center of each SRR element, with the width confined by the LC gap (2.7 μm), and length to 20 μm. The actual etched region was slightly larger than the designed value (Fig. 4.1b) owing to the OL error and the characteristics of RIE etching.

Fig. 4.1(b) and (c) show scanning electron microscopy (SEM) and optical microscope images respectively of one element and an overview of the array. All metamaterial patterns were prepared using direct-write DLP laser lithography (MLA150, Heidelberg Instruments) on a high-resistivity (>10,000 Ω·cm) undoped (100) silicon substrate with a thickness of 525 μm. Ti (10 nm) and Au (100 nm) metal layers deposited by electron-beam evaporation defined the THz SRR arrays. After that, the LC gap area was etched using a dry etching method, details of which are described in section 4.2.2. Dimensions of fabricated SRRs were measured, illustrated in Fig. 4.1(b) and (c), which were utilized for the simulations in the following sections.
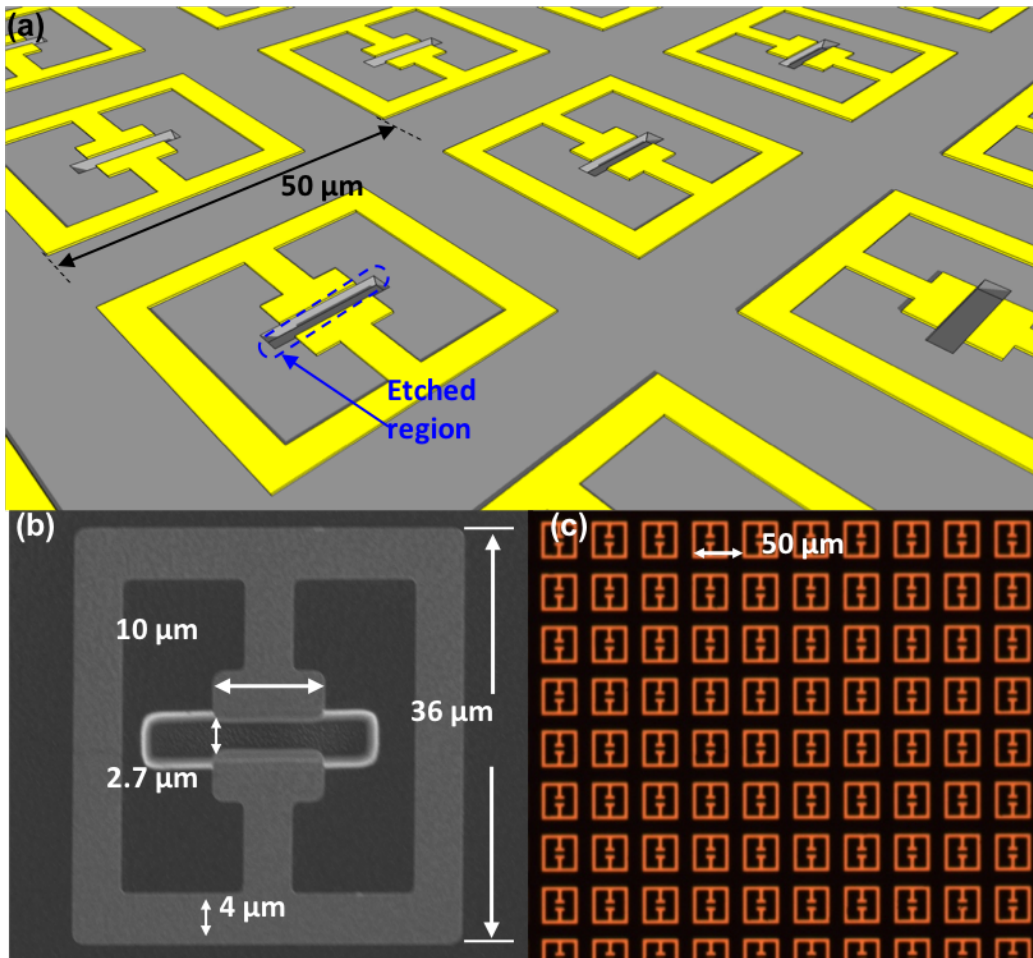
Figure 4.1 (a) Schematic of THz metamaterials arrays with trenches. (b) An SEM image of the SRR element. (c) An optical image of the SRR arrays.

4.2.2 Localized silicon substrate etching

To explore the optimal way to etch the substrate, two techniques, wet etching using KOH etchant and dry etching using RIE, were investigated here. Based on these experimental studies, the dry etching method was ultimately determined to be a better choice for this research.

KOH solution is one of the most widely used etchants for silicon etching, owing to its ease of use and fast etching rate [152, 153]. The KOH etchant

was prepared by mixing KOH tablets (Merck) into DI water, while stirring until the tablets dissolved. The solution was then warmed on a hot plate. The temperature and concentration both then affected the etching rate, which was measured as shown in table 4.1. The concentration by weight was determined and controlled in the process of preparing the solutions, while the temperature was measured directly using a thermometer. The experimental data show that the etching rate goes up with as temperature increases while, for highly concentred KOH solution, higher concentration results in lower etching rate, which agrees with previous research [154, 155].

Table 4.1 Silicon etching rate in KOH solutions of different concentrations at different temperatures

KOH	20%	30%	40%	50%
21 °C	0.022 µm/min	0.017 µm/min	0.011 µm/min	0.005 µm/min
36 °C	0.116 µm/min	0.079 µm/min	0.067 µm/min	0.052 µm/min
60 °C	0.660 µm/min	0.634 µm/min	0.539 µm/min	0.379 µm/min

Two reasons ultimately determined that KOH etchant was not best suited for the localized etching in this research. Firstly, the anisotropic nature of the etch produces a trench with sidewalls at an angle of ~54.7° angle to the (100) surface [156, 157], as illustrated in Fig. 4.2(a), limiting the etch depth that could be obtained. To confirm this, the profile of etched trench edges on

(100) silicon patterned using large etch windows was directly measured by a surface profiler (Alpha-Step IQ, KLA-Tencor), obtaining a ~ 56° angle between the substrate surface and the etch edge, as shown in Fig. 4.2(b). The 1.3° difference between the theoretical value and the measurement value probably arose came from systematic error in the profiler, and / or impurities on the substrate that affected the etching. Because of this, the dimension of etching window limits the trench depth to the maximum value of $D_{max} = \tan 54.7° \cdot w/2$, with w the width of etching window, as observed in silicon samples patterned by small etching windows (Fig. 4.2(c)). For the SRR designs in this research, the LC gap was 2.7 µm wide, limiting the maximum etching depth to around 1.9 µm, which was not sufficient for this study. Secondly, the materials used to pattern the etch masks have to be thoroughly removed without negatively influencing the devices in case they affected the dielectric sensing, which proved difficult for strong KOH. Some inert materials, such as SiO_2 [158] and gold [159], can be used as masks to protect the substrate from KOH etching, but these are hard to remove entirely while keeping the metamaterials unchanged. Aluminum or chromium are sometimes used as fast KOH etching masks [160], but they are not good enough in this case, as shown in Figure 4.2 (d), in which silicon at the locations adjacent to the gold tracks of SRRs were etched due to pinhole effects. Based on the discussion above, a more suitable silicon etching technique was thought to be needed.
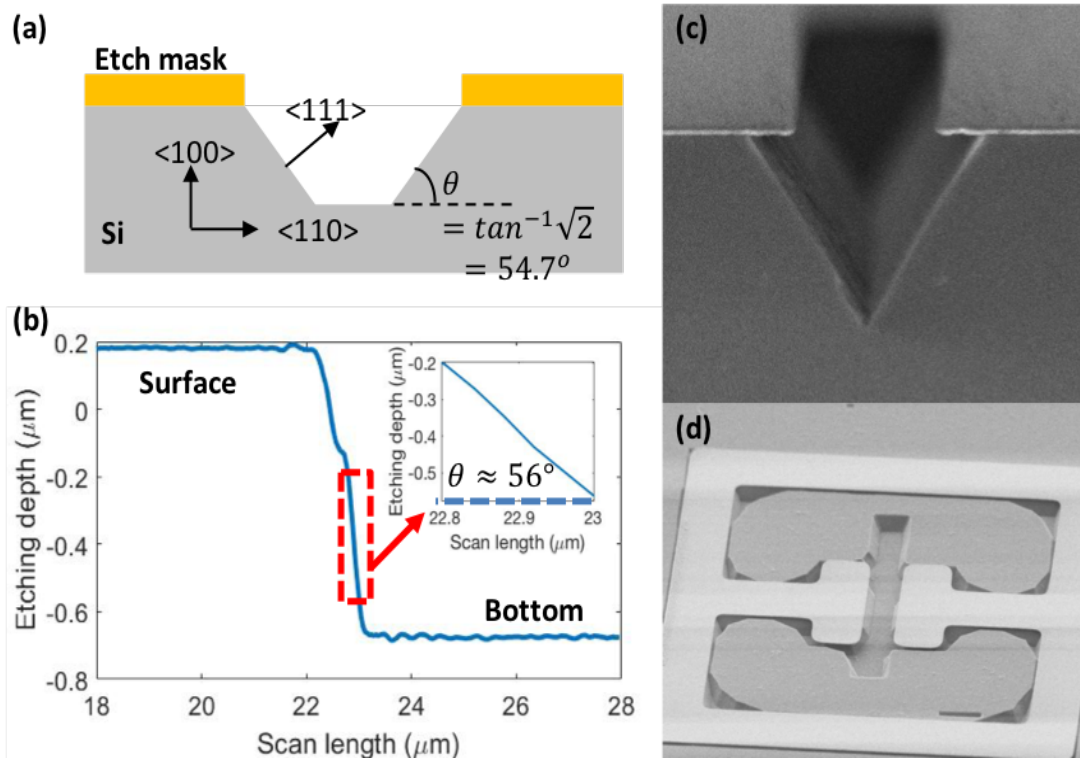
Figure 4.2 (a) Schematic of anisotropic wet etch on (100) silicon. (b) Profile of trench edge in (100) silicon etched by KOH solution. (c) An SEM image of V trench in narrow window confined (100) silicon etched by KOH solution. (d) An SEM image of chromium protected metamaterial after KOH etching.

Reactive ion etching is an alternative technique for silicon etching capable or obtaining high aspect ratios [161, 162], while allowing easier protection of the substrate using standard positive photoresists, (such as Shipley S1813 or Micro Chemicals Corp AZ9260), making it a potentially promising candidate technique for silicon etching in this research. S1813 was used for trench depths < 5 μm, while AZ9260 was used for trench depths > 7.4 μm; both were first spin-coated and then patterned by photolithography into an etch mask. The RIE chamber was then prepared by applying 50 W RF bias onto a gas mixture of 30 sccm SF_6 and 20 sccm O_2 for 3 mins before the etching process; a 2-inch silicon wafer was loaded in the system

for this. The pretreatment aims to prepare the inner wall conditions of the chamber ensuring a stable etching.   After that, metamaterials with photoresist masks were etched using the same RIE parameters as used for the chamber pretreatment; this resulted in an etching rate of 210 nm/min according to calibration using SEM measurements. SRR arrays were successfully fabricated with trench depths up to 7.4 µm by adjusting the etching time.
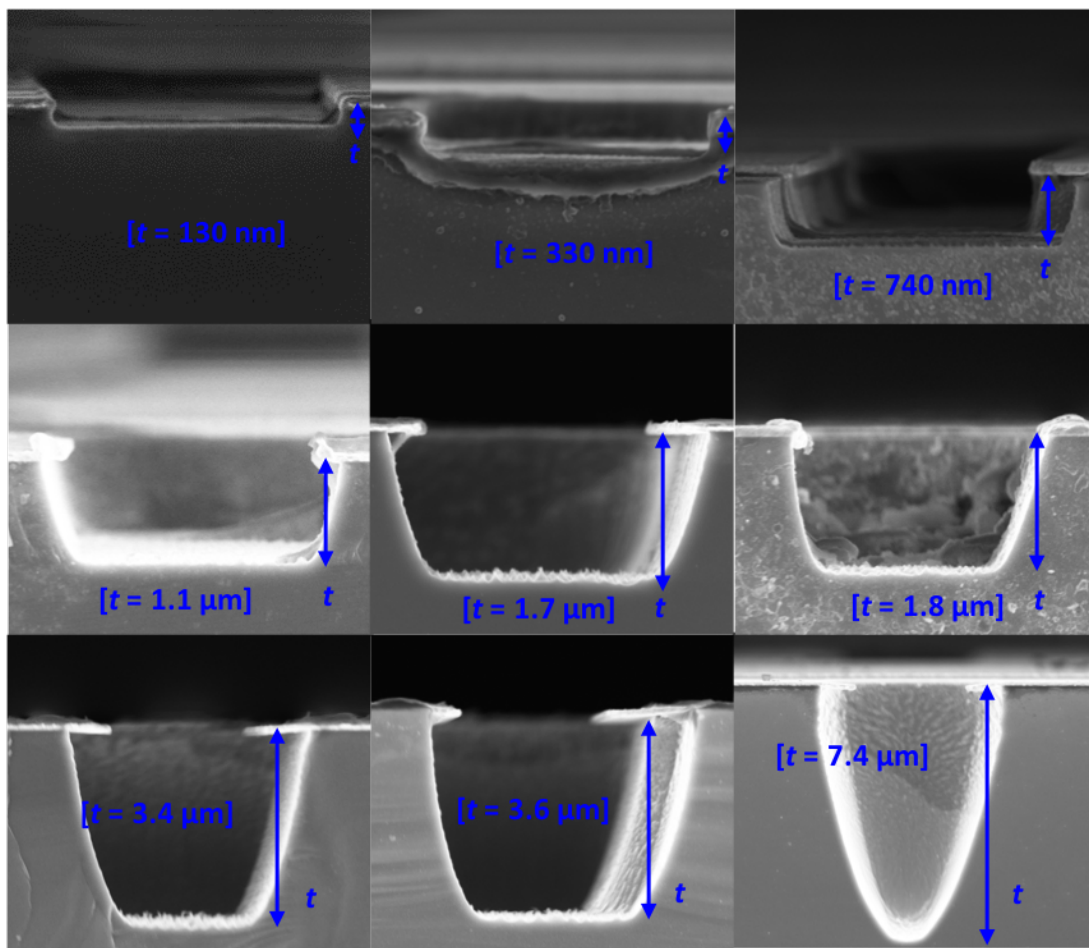
Figure 4.3 Cross-section SEM images of the SRRs with various trench depths obtained by RIE.

Cross-sectional SEM images of etched trenches with various depths from 130 nm to 7.4 μm are shown in Fig. 4.3. Significant and repeatable resonant frequency shifts along with the desired sensitivity enhancement were seen in the following measurements, indicating that RIE is a good technique for silicon etching in this research.

4.2.3 Data acquisition

Terahertz TDS was used to test the performance enhancement of the etched SRRs dielectric sensors. Fig. 4.4(a) shows a schematic diagram of the metamaterial chips undergoing pulsed THz measurements along with the polarization direction of the incident THz waves. The PC THz emitter and detector were each comprised a two μm-thick layer of LT-GaAs transferred on to a five mm-thick quartz substrate, fabricated using an epitaxial lift-off method [163] (noting that these were fabricated by Dr David Bacon in our research group). THz pulses generated from the PC antenna were focused on to the surface of the metamaterials, with a spot size of ~ 1.2 mm^2 measured using knife-edge method (Fig. 4.4(b)), which illuminated ~ 480 SRR elements. Pulses obtained in transmission through the array (Fig. 4.4(c)) were fast Fourier transformed (Fig. 4.4(d)) and then normalized to reference traces obtained from an unpatterned silicon substrate. In Fig. 4.4(d), two different resonant modes are observed. The LC resonance introduces a narrow absorption feature at a frequency below 1 THz, which can be highly modulated by etching the LC gap areas of the metamaterial. By contrast, the dipole resonance produces a broad absorption feature peaking at around 2 THz, the frequency of which is determined by the

dimension of the outer frame of the SRRs and which does not change for the trench depth in gap areas.
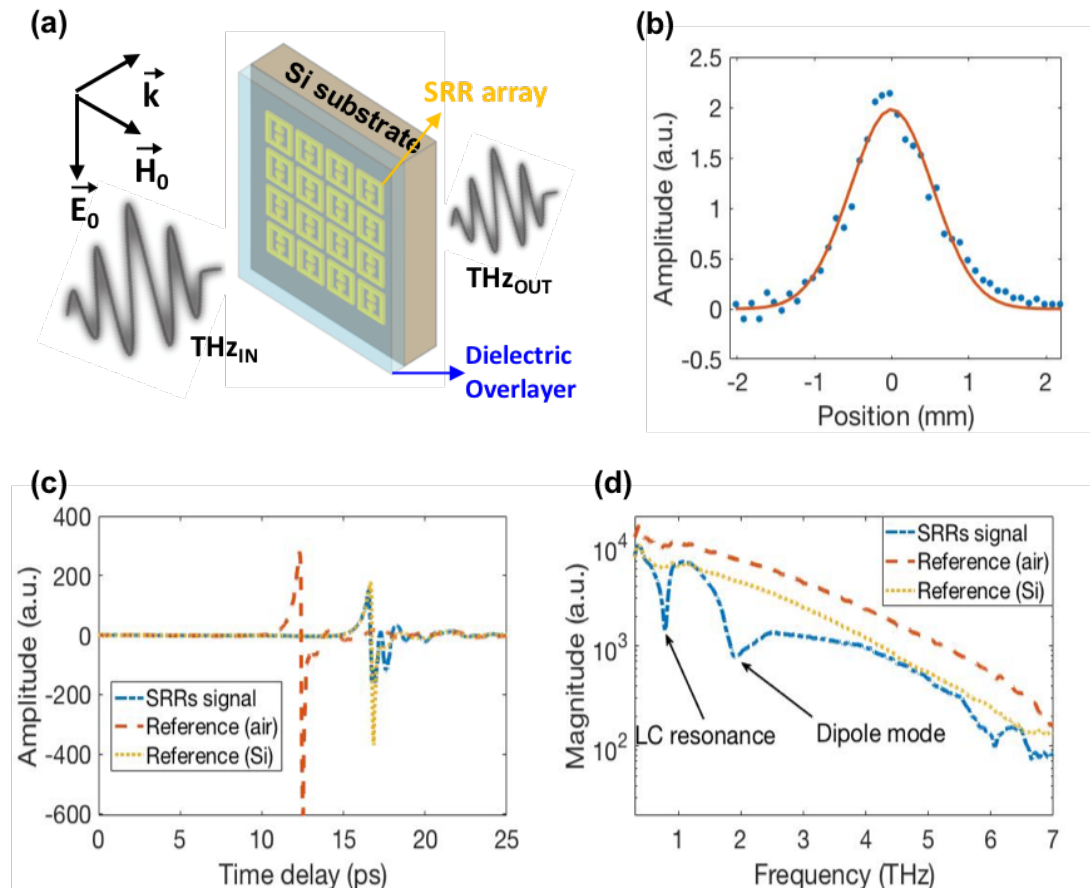
Figure 4.4 (a) Schematic of the THz transmission experiment for dielectric sensing using etched metamaterials. (b) Profile of THz spot incident on SRRs, obtained by translating a knife-edge across the focal spot. (c) Time domain, and (d) Frequency domain spectra of the SRRs signal and reference.

4.3 Localized etch trenches induced properties change of the SRRs

4.3.1 Effective permittivity decrease

To understand the effect of the etched trench structures on the effective dielectric permittivity, finite-element simulations were performed to investigate the electric distribution near the gap area, using commercial

software (Ansys High Frequency Structure Simulator, HFSS). A linearly polarized incident THz plane wave and periodic boundary conditions around a single unit cell were chosen, which provided a suitable simulation of our SRRs. The SRR itself was considered as a perfect sheet conductor with the sheet conductivity being set as 10^7 S, while 11.8 (±0.1) was used for the silicon permittivity, as previously obtained using conventional THz-TDS methods [164]; the trench depth chosen was 7.4 μm.

Shifts in the distribution of the electric field were seen near the gap area both in the transverse and in the vertical directions when THz pulses were incident on the metamaterials. Fig. 4.5(a) and (b) show the 2D electric field distribution in the SRR element area along the x-y plane (at z=0) for metamaterials both without and with the etched trench structures, respectively. The electric field magnitude in the gap area was significantly decreased when the trench structures were introduced, which can be seen by comparing Fig. 4.5(a) and Fig. 4.5(b). The decrease of field magnitude is owing to the reduction of the capacitance of the gap structure, which is proportional to the effective dielectric permittivity of the gap, indicating a decrease of effective dielectric permittivity. To further confirm the change of effective permittivity, the electric field distribution along the z-axis (at x=0 and y=0) is plotted in Fig. 4.5(c), where the solid black line represents the electric field distribution of unetched metamaterials while the dashed red line represents the distribution of 7.4 μm etched metamaterials. Clearly, the decay length of the electric field magnitude in the substrate region (z<0) is larger for the etched trench metamaterials, which illustrates a smaller effective permittivity of etched metamaterials. The simulations also reveal a

slight shift down to the substrate direction (~ 200 nm) in the position of the maximum electric field magnitude (inset to Fig. 4.5(c)) as expected since the trench structure replaces a portion of the substrate by air.
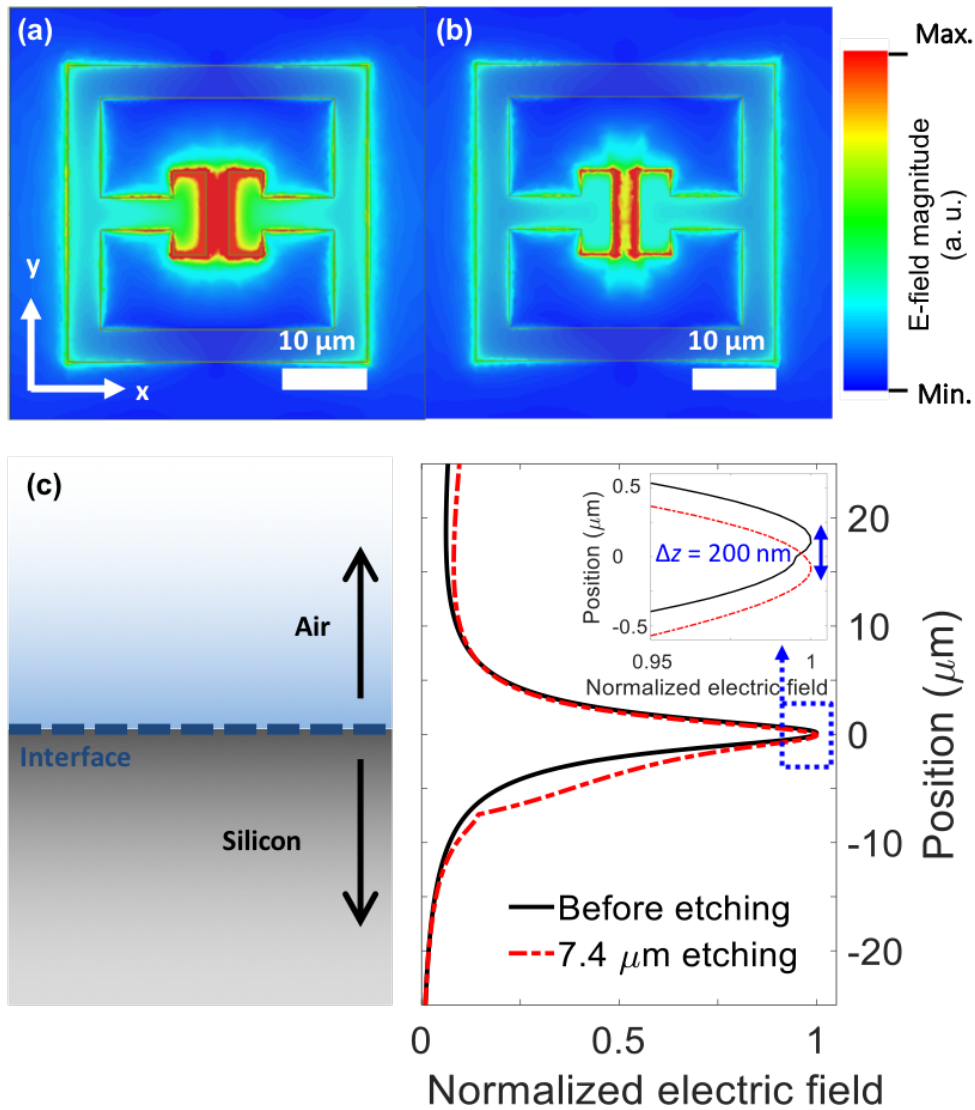
Figure 4.5 Field distribution near the metamaterials surface (at z = 0) for (a) normal metamaterials and (b) etched metamaterials. (c) LHS cross-section of the interface between silicon and air. RHS The electric field line profile near the center of the gap structure along the z-axis. Inset: Close-up view of the electric field line profile near the air-substrate.

4.3.2 Resonant frequency blueshift

The frequency of the *LC* resonance depends strongly on the effective dielectric permittivity in the gap area which can be expressed as a combination of the air and the substrate refractive index [165]. The LC resonant frequency can be expressed by $f = f_0(\varepsilon/\varepsilon_{\text{eff}})^{-\frac{1}{2}}$, where ε_{eff} is the effective permittivity in the gap area, f_0 is the resonant frequency when the permittivity is ε and the relation between them two depends on the geometry of the SRRs [142, 150]. Thus, by reducing the effective permittivity, a blueshift of the resonant frequency is expected.

The change of THz transmission spectra of the SRR arrays owing to the trench structures induced effective permittivity change, was demonstrated by comparing devices without trench structures and with 3.4-μm-deep trench structures, as shown in Fig. 4.6(a) and (b), which were obtained by experiments and simulations, respectively. In simulations, a trapezoid cross-section was used for modeling the sloped sidewalls of the etch trench as observed in the SEM images to better approximate the structure used in the experiments. In Fig. 4.6, the solid black line shows the transmission of SRRs without etching trenches, while the dashed red line gives the transmission of SRRs with 3.4 μm of etching trenches, where the position of the valley transmission value is the LC resonant frequency. A blueshift in resonant frequency of 116 GHz (from 788 GHz to 904 GHz) with an error of ±0.6 GHz in the experiments and 110 GHz (from 794 GHz to 904 GHz) with an error of ±4 GHz in the simulations was observed. The Q-factor of the LC resonance decreased from 7.8 to 5.3 with the introduction of the

trenches owing to the decrease in the capacitance, which reduces the confinement effect of the LC circuit to the electromagnetic wave.
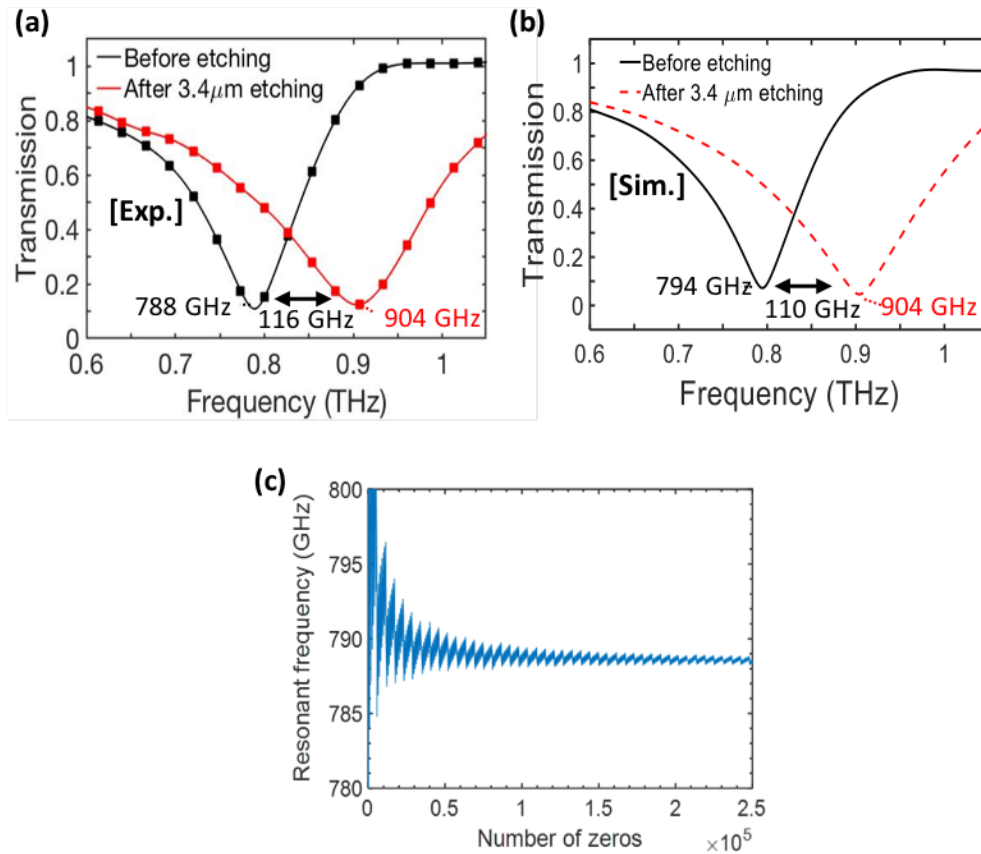
Figure 4.6 THz transmission spectra of the metamaterials with and without the trench structure in the (a) experiment and (b) simulation. The dots in (a) are the raw data. (c) The resonant frequency of the metamaterials without the trench structure as a function of the number n of padded-zeros in the Fourier transform, showing convergence to a single value of f for large enough n.

The experimental error was estimated from the residual spread in the resonant frequency of zero-padded data. Numerically, the frequency resolution (uncertainty) of a spectrum obtained by FFT of a time-domain signal depends on the time delay of the signal. Zero-padded method

numerically makes the time delay longer, which could suppress the frequency uncertainty caused by the numerical calculation, as shown in Fig. 4.6(c). The number of zero used in this chapter was 2.4×10^5, resulting in the error of about 0.6 GHz. The error in the simulation results from the experimental error in the dielectric constant of the silicon substrate. The silicon dielectric constant was taken as 11.8 ± 0.1, which we obtained using conventional THz-TDS methods. We first measured both the amplitudes and phases of the transmitted THz pulse through the silicon substrate and calculated the dielectric constant of the silicon substrate using the measured phase and substrate thickness. The error of 0.1 quoted here in the silicon dielectric constant arises from our estimate of error in the silicon substrate thickness. This error of dielectric constant, which was utilized for the simulation, induced an error of simulated resonant frequency.

To provide further insight, the resonant frequency with respect to etching depths was investigated, both in experiments and in simulations. Fig. 4.7 shows the resonant frequency of the etched metamaterials as a function of the trench depth, in which the squares are the collected data in experiments (black), and simulations (red) and the dashed lines are the exponential fitting curves of them. An exponential fitting was used because the electric field decayed exponentially as the position away from the surface of the substrate, which was shown in the simulation results in Fig. 4.5(c). Both fitting curves were obtained using the auto fitting function of Matlab by the equation of $f(x) = a \cdot \exp(-b \cdot x) + c$. For experimental data, the fitting parameters of a, b, and c were -0.1865, 0.2948, and 0.9752, respectively, with the confidence intervals of (-0.1957, -0.1774), (0.2627, 0.3269), and

(0.9654, 0.985), respectively. For simulation data, the fitting parameters were -0.1699, 0.3193, and 0.9639, respectively, with the confidence intervals of (-0.1763, -0.1635), (0.2863, 0.3523), and (0.9581, 0.9696), respectively.
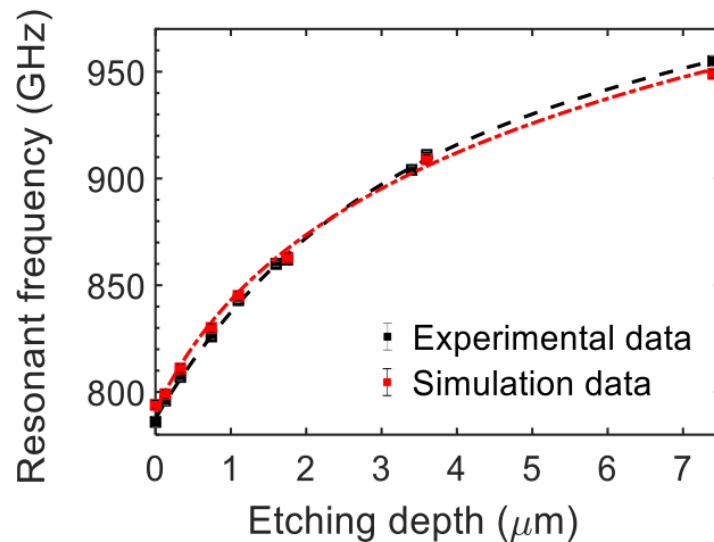
Figure 4.7 The resonant frequency of metamaterials as a function of trench depth in the experiment and simulation.

The resonant frequency of the metamaterials is seen to gradually increase with the etching depth. The deepest trench depth reliably obtained in this research was ~7.4 µm, limited by the anisotropy of the RIE method, which produced increasingly angled side walls as shown in Fig. 4.3. The experimental findings are in excellent agreement with the predictions of the simulation values, although small systematic deviations (of order a few GHz, or ~0.5%) were observed. These deviations likely arise from the limited spatial resolution of the lithographic techniques being used and / or the simplification of the shape of the trench cross-section to a trapezoid in the simulation. The positive correlation between the resonant frequency of metamaterials and the etching depth supports our previously stated

assumption that the effective dielectric permittivity decreases with increasing depth of the etched trenches.

The resonant frequency of metamaterials with trench depth deeper than 7.4 µm was also simulated, and the resonant frequency shift was found to progressively saturate at about 970 GHz for large trench depths. The reason for the saturation behavior is that the evanescent field in the gap area is highly confined near the surface (within ~ 10 µm) [148], resulting in gradually vanishing interaction between the resonant THz wave and the substrate as the position going deeper.

4.4 Localized etch trenches induced dielectric sensitivity enhancement of the SRRs

4.4.1 Increase of dielectric induced frequency shift

A well-characterized dielectric material, S1813 [166, 167], was then applied to the SRR arrays in order to investigate the effect of the etched trenches on the sensitivity. To accurately obtain the dielectric constant of S1813 for use in the simulation, the relationship, $\varepsilon_{\mathrm{r}} = 25.06 \cdot \Delta f_{\mathrm{sat}}/f_0 + 1$, was used, where ε_{r} is the relative dielectric constant of the target materials, and Δf_{sat} the saturated resonant frequency of the SRRs without etching obtained with the deposition of a dielectric over-layer thicker than 15 µm [168]. Here, the size of the saturated resonant frequency shift, Δf_{sat}, can be described by $\Delta f_{\mathrm{sat}}/f_0 \approx \alpha(\varepsilon_{\mathrm{S1813}} - \varepsilon_{\mathrm{air}})/\varepsilon_{\mathrm{eff}}$, where α is the sensitivity coefficient determined by the geometry of the metamaterials, $\varepsilon_{\mathrm{S1813}}$ is the dielectric constant of S1813, and $\varepsilon_{\mathrm{air}}$ is the dielectric constant of air [168].

Based on the experimental data, $f_0 = 789\ GHz$ and $\Delta f_{\text{sat}} = 62\ GHz$, the dielectric constant of S1813 was obtained to be 2.97 with an error of ±0.16 arising from the fitting error of frequency being used for calculation.

The terahertz transmission spectra of the THz SRR arrays with various etch trench depths and various thicknesses of spin-coated S1813 were obtained. Fig. 4.8(a) shows an experimental example of THz transmission properties of the "normal" SRRs (black curves) and etched SRRs with 3.4 µm deep trench structures (red curves), both with (dashed lines) and without (solid lines) the deposition of a 3.5 µm thick S1813 layer. The measured resonant frequencies of both normal SRRs and etched SRRs showed a redshift after coating with S1813 layers, and the size of the frequency shift obtained from the device with 3.4 µm deep trench structures was 86 GHz ±1.2 GHz, which increased by a factor of ~two times compared with that of the standard SRR device, 40 GHz ± 1.2 GHz. Simulation results, as shown in Fig. 4.8(b), were in good agreement with the experimental results when the same parameters as the experiments being taken in the simulation. The results indicate that trench structures in the SRR device enlarge the size of the frequency shift with the equal quantities of dielectric materials being introduced.
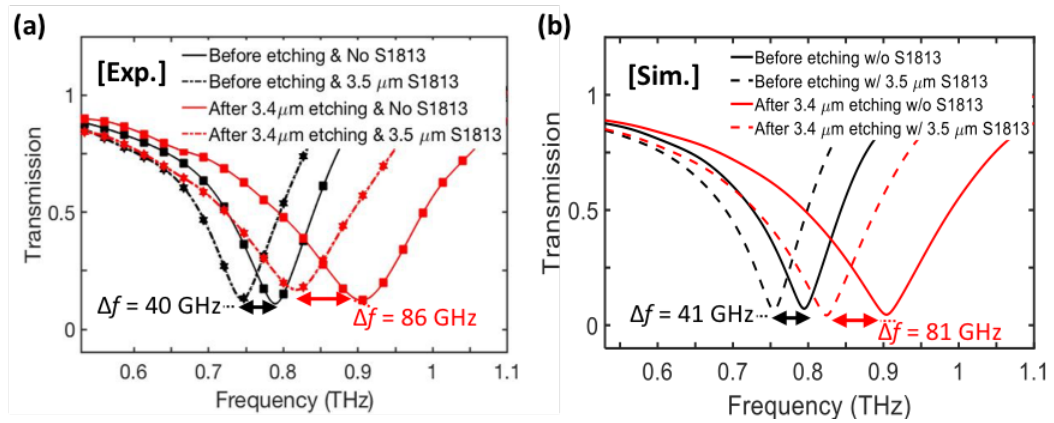
Figure 4.8 THz transmission of traditional SRRs and the SRRs with 3.4 μm depth trench structures, both with and without coating 3.5 μm S1813 layer in (a) experiment and (b) simulation. The dots in (a) are the raw data.
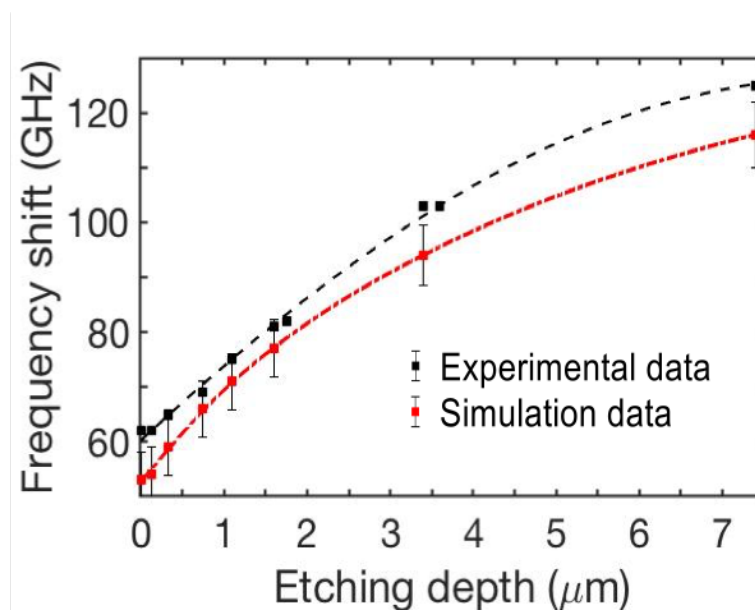
Figure 4.9 The resonant frequency shift of the SRRs coated thick resist layers as a function of the trench depth in experiment and simulation.

Deeper trench depth results in a lower overall effective dielectric permittivity, which consequently induces a larger resonant frequency shift caused by the introduction of the same quantities of overlaid dielectric

materials. To confirm this, thick (>15 μm) S1813 overlayers were spin-coated on SRR devices with various depths of trench structures, and the saturated frequency shifts, Δf_{sat}, were obtained and plotted in Fig. 4.9, where the squares are the data obtained from experiments (black) and simulations (red), and the dashed lines are the exponential fitting curves. The simulation results are in good agreement with the experimental findings taking into account the size of the errors discussed above. The increase of the resonant frequency shift was observed as the depth of the trench structures increased, from ~60 GHz in normal SRRs to ~120 GHz in 7.4 μm etched SRRs. The positive correlation between the frequency shift and the etching depth indicates the effectiveness of the performance enhancement of metamaterials acting as dielectric sensors by introducing the localized etching trenches in the LC gap areas.

4.4.2 Enhancement of dielectric sensitivity

Here, the ratio between the shift of the resonant frequency and the thickness of the overlaid S1813 layer is applied to analyze the sensitivity enhancement of the etched metamaterials. The ratio should be constant when a sensor works in its linear region.

(a)

(b)
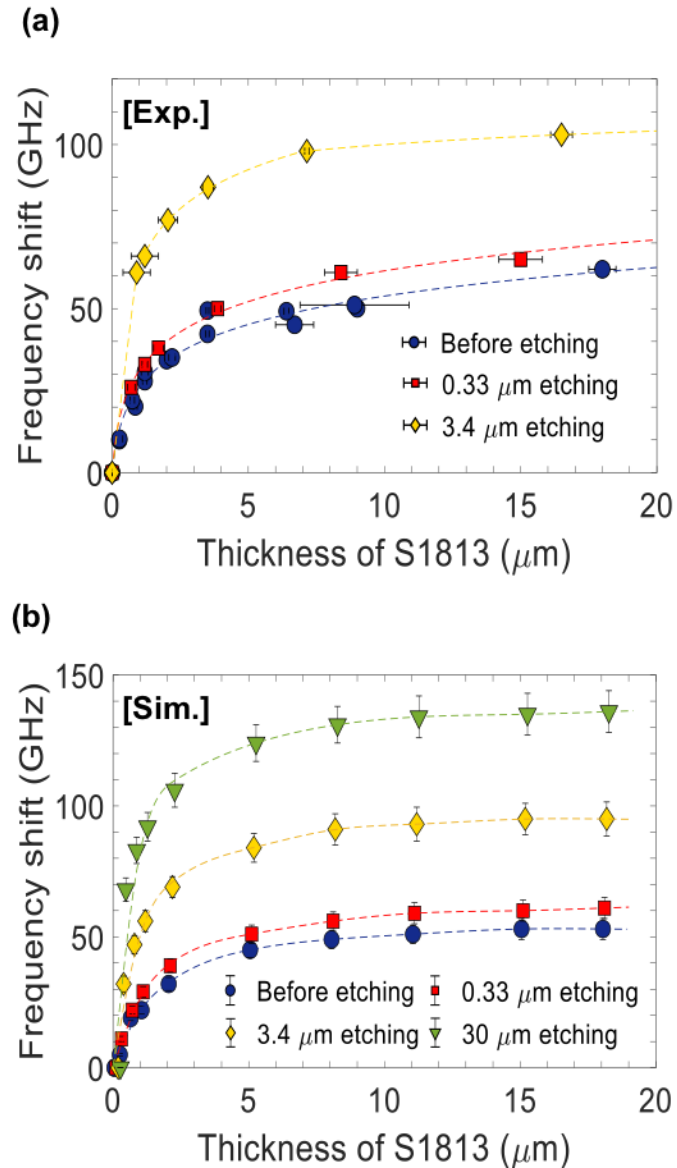
Figure 4.10 Resonant frequency shift as a function of hS1813 for various trench depths in the range of (a) 0 – 3.4 μm in experiments and (b) 0 – 30 μm in simulations.

To investigate the sensitivity, the relationships between the frequency shift and the thickness of S1813 layer in each device were firstly obtained in experiment and simulation. The frequency shifts as a function of the thickness of S1813 coated on devices under three etching conditions: un-

etched, with a shallow trench (0.33 µm), and with a deep trench (3.4 µm), are plotted in Fig. 4.10(a) and (b), obtained by experiments and simulations, respectively. In these two figures, blue circles, red squares and yellow diamonds give the data of the unetched device, the device with 0.33 µm etching depth and the device with 3.4 µm etching depth, respectively. Furthermore, a simulation of the metamaterials with a deeper trench depth (30 µm) was made and shown in Fig. 4.10(b) by green triangles. The fitting curves for all the data are plotted as dashed lines with the same colors as the discrete data. As can be seen, the frequency shifts experience a fast, linear increase as a function of the thickness of S1813 layers in the smaller layer thickness region, and then gradually saturate to a specific value in the larger layer thickness region. In that case, the sensitivity of the device is reasonably extracted from the initial slopes of the $\Delta f - h_{S1813}$ curves in the linear region ($h_{S1813} < 2$ µm).

The sensitivities extracted by dividing the initial slopes of the $\Delta f - h_{S1813}$ curves in Fig. 4.10 by the refractive index are shown in Fig. 4.11. The sensitivity is enhanced by a factor of ~2.7 through the introduction of a 3.4-µm-deep trench, from 4.28×10^{-2} GHz/nm to 11.61×10^{-2} GHz/nm in experiments and from 3.51×10^{-2} GHz/nm to 10.42×10^{-2} GHz/nm in simulations. The sensitivity could be further enhanced by ~6.6 times the sensitivity of unetched device, obtained from the initial slope of the green curve in Fig.4.10(b), by introducing the etch trench depths up to 30 µm, which is an achievable etching depth using anisotropic etching techniques such as Inductively Coupled Plasma Etching [169]. By now, a significant dielectric sensitivity enhancement of SRRs by introducing localized etch

trench structures has been demonstrated both in experiments and in simulations.
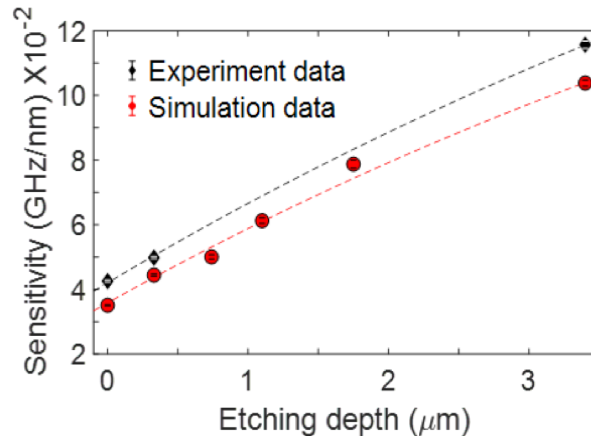
Figure 4.11 Sensitivities extracted from the initial slopes as a function of the etching depth.

To confirm that the sensitivity enhancement was caused by the reduction of effective permittivity instead of the increase of resonant frequency, additional simulations were performed to compare the sensitivity of two SRR devices without trenches and operating at 794 GHz and 904 GHz respectively. The 904 GHz was chosen because this was the same frequency that the 3.4 μm device worked at. The resonant frequency was adjusted by changing the LC gap distance. An SRR with a gap of 2.7 μm resonates at 794 GHz while SRR with the gap distance of 7.96 μm operates at 904 GHz. The sensitivity obtained from the initial slope decreases when f0 increases to 904 GHz in the main region where we are interested (h1318 < 1 μm), as shown in Fig. 4.12. The resonant frequency shift slightly increased by 4 GHz when the resonant frequency shifts are saturated, while for a comparison the degree of resonant frequency shift introduced by the 3.4 μm

trenches was increased by 42 GHz. This confirms that the increase in sensitivity and Δf is caused by the reduction in effective permittivity.
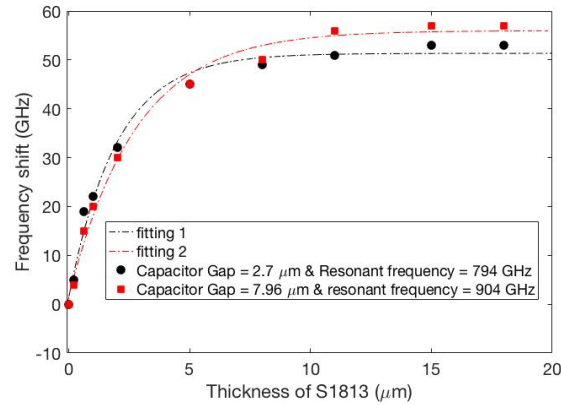
Figure 4.12 Resonant frequency shift as a function of hS1813 for SRRs working at 794 GHz and 904 GHz, respectively.

4.5 Conclusion

This chapter demonstrates an enhancement in sensitivity of THz metamaterials sensors to overlaid dielectric materials, by the introduction of etched trenches in the LC gap area, which reduces the local effective dielectric permittivity. These results are useful for practical dielectric sensing applications based on metamaterials devices and have been submitted to Optics Express for a publication. In addition, this work contributes to further understanding the mechanism of THz metamaterials as dielectric sensors and, as discussed later in the conclusions and further work chapter, a similar methodology could be extended to other metamaterials devices.

Chapter 5 Terahertz wave modulation and detection with graphene

5.1 Chapter introduction

The unique electronic and optoelectronic properties of graphene, as discussed in chapter 2, make it a promising material for a variety of THz applications [170, 171]. Although graphene possesses Dirac fermions owing to the quasi-relativistic dispersion of the bandsstructure [1], the ac conductivity of graphene in the terahertz regime still exhibits Drude absorption behavior [172], which has been experimentally demonstrated with epitaxial graphene [173] and CVD grown graphene [174]. When the graphene was excited by high-intensity laser, population inversion in graphene can be obtained over a wide terahertz spectral range even at room temperature [175, 176], which indicates the application of THz amplification and THz laser. The lifetime of photoexcited carriers in graphene lies in sub-ps to tens of ps range [177, 178, 179], making graphene a suitable photoconductive material for pulse THz emitters and detectors [28]. On the other hand, the wavevector of plasmon in graphene is more than two orders larger than that of THz wave, which allows dimension of graphene THz devices much smaller than the wavelength of THz wave (miniaturized THz devices) [180, 181, 182, 183]. On top of that, the symmetric, gapless and linear band structure of graphene

[184, 6] means that the carrier density can be easily modulated [185], so allowing the manufacture of tunable THz devices.

Based on the discussion above, one potential application is THz detection owing to the strong interaction between graphene and THz wave. The majority of works focus on power detection [186, 187, 29, 188, 189], the signal of which is linear with the power of the incident THz wave, with reported voltage responsivities reaching 10 V/W at room temperature [186] and 240 V/W at 10K [29]. Besides, owing to the mechanical properties of graphene, flexible graphene terahertz detectors have been realized with a voltage responsivity reaching 2 V/W at room temperature [187]. Another THz detection approach is time domain amplitude detection, based on photoconductive antennae, which is suitable for THz-TDS application and which has been realized in on-chip devices [28].

Another potential application of graphene in THz technology is as a THz modulator, since by electrically tuning the Fermi level of graphene the carrier density and the optical conductivity of graphene are easily modulated. The maximum electrical modulation depth, calculated by $MD = (T_{max} - T_{min})/T_{max}$ with T_{max} and T_{min} the maximum and minimum transmittance, of sheet graphene is around 10%, according to a previous study [47], which is not sufficient for practical applications. Several methods have been adopted to improve the modulation depth. Multi-layer graphene shows a larger modulation depth than monolayer graphene [190, 191, 192], allowing a modulation depth of larger than 80% to be realized. Introducing 2D THz resonators or cavities into graphene samples is another way to enhance the

modulation depth [41, 42, 43, 44, 76]. More than 90% modulation depth was realized for THz wave propagating in free space [44], while a modulation depth of 100% was reported by integrating graphene on the output apertures of surface-emitting concentric-circular-grating THz quantum cascade lasers [76]. Whereas, the significant modulation enhancement is limited in a narrow frequency band around the working frequency of the structures [43]. The introduction of Fabry-Perot interference is another way to enhance THz modulation, though this only works in a narrow frequency range [30, 193].

The modulators discussed above didn't aim to polarizer applications, but since controlling the polarization of a THz wave is an essential issue in THz technology [194], working on tunable graphene THz polarizers is of potentially high significance. The graphene metasurfaces was shown to be promising for tunable THz polarizers, which was illustrated by many theoretical designs and simulations [195, 46, 196, 72, 197, 198]. Most of these designs use metasurfaces with certain resonant frequencies to enhance the modulation of the polarizer, whereas the consequent problem caused by this is that the polarizer can only work over a narrow band of frequencies. Recently, a different approach was proposed and experimentally realized, based on a graphene-controlled Brewster angle device [31]. Using this technique, the modulation depth surpassed 99%, with a broad bandwidth ranging from 0.5 THz to 1.6 THz, limited by the frequency-dependent Brewster angle.

This chapter investigates two THz applications for graphene based on the THz-graphene interaction. In section 5.2, based on our group's previous

work of on-chip THz detection using graphene PC antenna, this research extended our work to make a free-space THz detection antenna using graphene. The fabrication of this graphene bowtie photoconductive antenna is discussed, then allowing time-domain traces of free-space terahertz pulses to be detected. The signal-to-noise ratio (SNR) of the THz signals obtained by fabricated graphene bowtie detector was ~ 130, with a bandwidth of ~2 THz. This SNR was poorer than LT-GaAs detector mainly due to larger noise, whose details were discussed in section 5.2.2. The factors that affect the detection performance were also discussed based on experiments in the following sections.

In section 5.3, a broadband tunable THz polarizer was designed with a geometry utilizing hybrid graphene-metal strip arrays, which dramatically enhanced the modulation depth compared with graphene strips by increasing the effective conductivity and the plasmon-terahertz wave coupling. After fabrication, the direction dependent modulation, the bandwidth, and the modulation enhancement of polarizers with different metal and graphene dimensions were examined. The THz polarizer of this hybrid-stripes geometry with ~18 times modulation enhancement compared with graphene-stripes polarizer was obtained experimentally, which agreed with the calculation results. Also, we predict greater than 40 THz bandwidth with a modulation depth of 95% at 0.5 THz, with a maximum of >98% modulation depth is reachable according to the calculations.

5.2 THz pulse detection using graphene photoconductive antenna

Since graphene is a promising material for THz detection and the technique for on-chip THz pulse detection as has been established in our group, this section of work sought to extend this work to graphene bowtie PC antennae for free-space THz pulse detection.

5.2.1 Experimental methods

A graphene PC antenna was designed using a bowtie structure, with gap dimensions of 20 µm. A bowtie-shaped antenna typically provides good THz detection sensitivity and wide spectral bandwidth [199]. CVD graphene was first transferred to a quartz substrate following the recipe discussed in chapter 3. Then, a bowtie pattern was prepared using optical lithography, followed by deposition of Cr (10 nm) and Au (100 nm) metal layers by thermal evaporation and lift-off in acetone. Chrome was chosen as the adhesion layer because of its relatively low contact resistivity [200]. After that, a 20 µm graphene stripe was formed by nitrogen plasma etching with a 20-µm-wide S1813 mask on top of it. Fig. 5.1 (a) shows the microscope image of the fabricated graphene bowtie, in which the long stripe across the center of the bowtie is the S1813 mask, showing the graphene's position. A close-up view of bowtie's gap area (Fig. 5.1 (b)) demonstrates a 20 µm × 20 µm graphene square bridging these two bowtie electrodes.
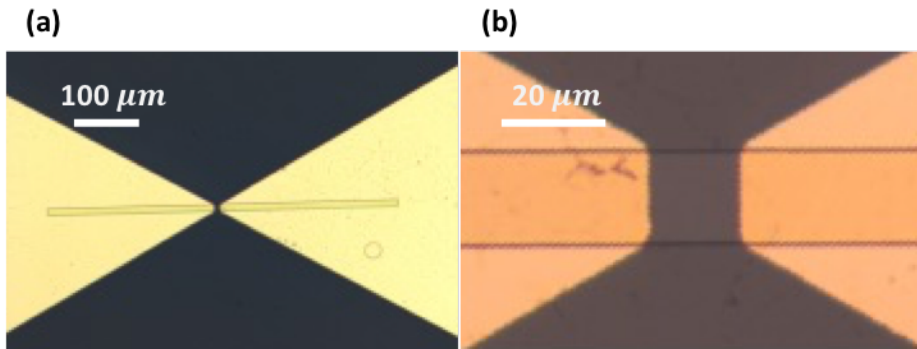
Figure 5.1 (a) Micrograph image of fabricated graphene bowtie, and (b) close-up image of the central area of bowtie.

Raman spectroscopy was utilized to confirm the graphene in the gap area after dissolving the S1813 mask in acetone, as shown in Fig. 5.2. Clear graphene characteristic spectra, in terms of the G peak and 2D peak, were obtained, in which the 2D peak was much larger than G peak, verifying the presence of single-layer graphene [106], while the D peak was beneath the noise level, indicating a high quality of the graphene sample given that the D peak corresponds to a defect-assisted intervalley single-phonon scattering [201].
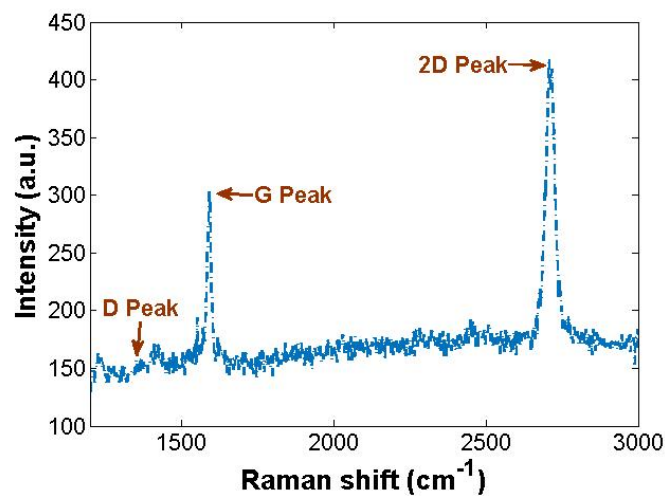
Figure 5.2 Raman trace of graphene in bowtie gap area.

A THz-TDS system was utilized to test the graphene detector by replacing the photoconductive detector in this system with the fabricated graphene bowtie antenna. A biased LT-GaAs PC antenna with a 200 μm gap illuminated by a 230 mW averge power pump laser beam with 100 fs pulse width and 796 nm central frequency, was used for THz pulse generation. Multiple intensities of THz pulses, which were modulated by a bias voltage, and powers of the probe beam, which were adjusted using a continuously variable laser attenuator and measured using a power meter, were made incident on the graphene detector to investigate its performance.

5.2.2 Detection performance
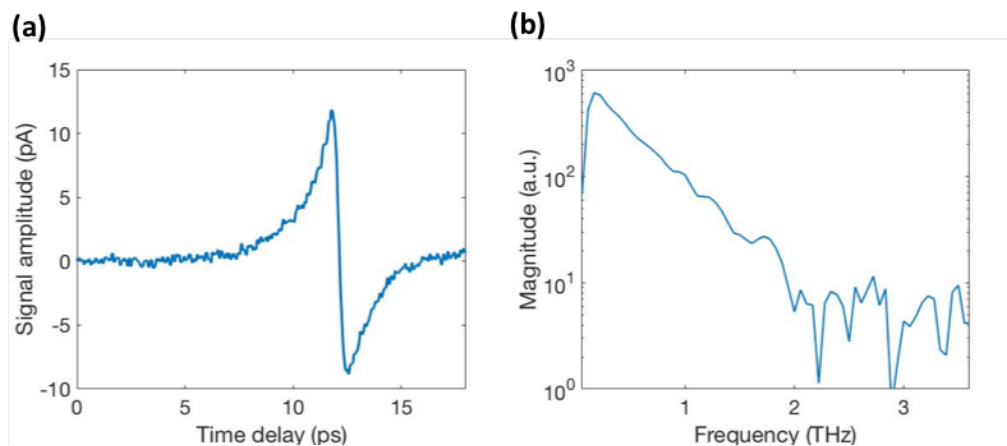
Figure 5.3 THz signal detected using graphene photoconductive antenna in (a) time domain, and (b) frequency domain.

Strong THz pulse signals were obtained by the fabricated graphene bowtie detector. A typical terahertz pulse trace is shown in Fig. 5.3(a); a 10 kV/cm emitter bias and 27.8 mW probe laser was used for this particular scan. The SNR was calculated by dividing the signal amplitude by the mean

square root of noise in the time domain to be about 130. Spectra of the terahertz pulse, obtained by fast Fourier transform (FFT) of the time domain trace, is shown in Fig. 5.3(b), indicating a bandwidth of 2 THz.

An LT-GaAs photoconductive antenna, which is one of the most widely used THz detectors owing to its high mobility, high intrinsic resistivity, and short photoexcited carrier lifetime [202], was used for comparison to investigate the comparative performance of the graphene detector. To compare the performance of the graphene detector and LT-GaAs detector, the detected terahertz pulse traces were normalized to the same incident terahertz pulse intensity and probe beam power in the gap area, as shown in Fig. 5.4(a) and (b), providing a direct comparison between LT-GaAs detector (red dashed line) and graphene detector (blue solid line) both in time domain and frequency domain, respectively.

Similar amplitude but narrower bandwidth of THz signal was obtained using graphene detector, compared with LT-GaAs detector, which was demonstrated both in time domain and frequency domain. Fig. 5.4 (a) shows the time-domain signals obtained by graphene bowtie and LT-GaAs bowtie, respectively, where the peak-peak amplitudes are shown to be 20.7 pA for graphene detection and 21.3 pA for LT-GaAs detection, indicating similar signal intensity. On the other hand, the full width at half maximum (FWHM) of the THz pulse detected by graphene detector was ~1.1 ps, which was larger than that of LT-GaAs detector (~0.5 ps), indicating a narrower bandwidth for the graphene detector. To provide a further comparison, the frequency-domain signals are given in Fig. 5.4(b), in which a cut-off frequency of 2 THz

was seen by graphene detection, comparing to 2.85 THz for LT-GaAs detection. The narrower bandwidth suggested a longer carrier lifetime in graphene since the lifetime of the photoconductive materials determines the bandwidth of PC antenna acting as THz detector. On the other hand, the signal detected by graphene detector was larger than that of LT-GaAs detector in the low-frequency range.
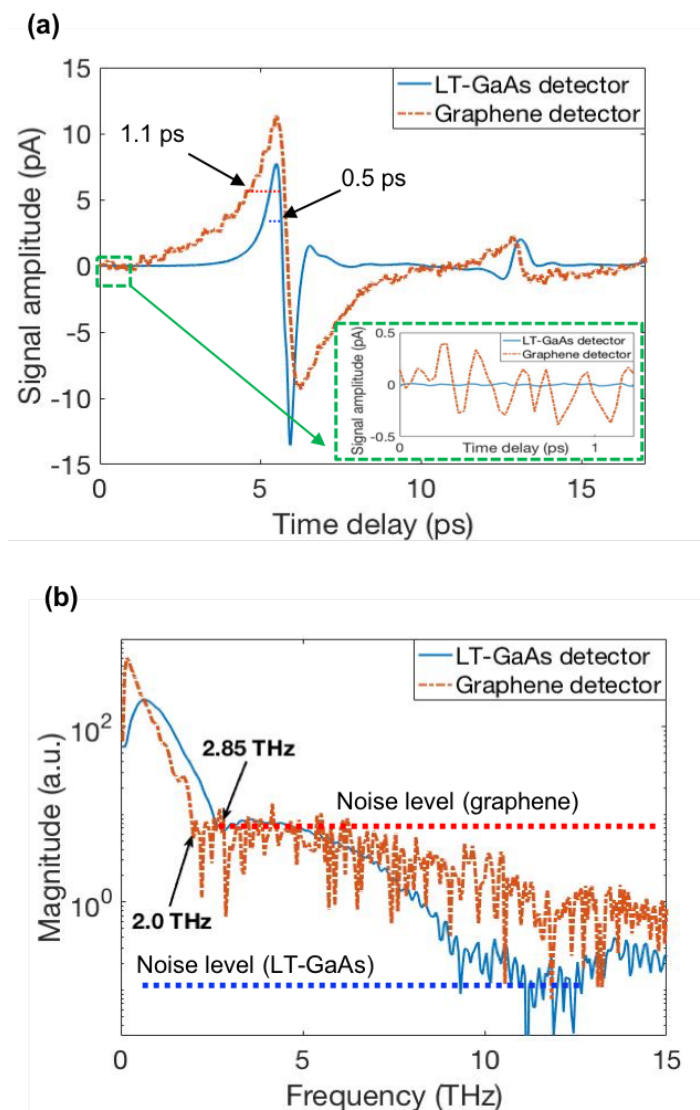
Figure 5.4 Comparison of THz signals detected by LT-GaAs bowtie and graphene bowtie in (a) the time domain, and (b) the frequency domain.

It is also notable that the noise of the graphene detection was tens of times larger than for the LT-GaAs detection, which was illustrated both in time domain (insert of Fig. 5.4(a)). The mean-square-root noise of graphene antenna is 0.16 pA while that of the LT-GaAs antenna was 0.02 pA. The larger noise in graphene-detection signal may be caused by the lower resistance of graphene, which resulted in a larger Johnson noise. The Johnso can be calculated by $\sqrt{\overline{v_n^2}} = \sqrt{4k_B T R}$, where $\sqrt{\overline{v_n^2}}$ is the voltage variance per hertz, k_B is Boltzmann's constant, T is absolute temperature in kelvins and R is the resistance in ohms. Illuminated by a 5.6 mW probe laser, which was the value being used to obtain the signal in Fig. 5.4, the resistances of graphene antenna and LT-GaAs antenna were 1.5 kΩ and 187 MΩ, respectively. Johnson noises are calculated to be 4.9 $nV/\sqrt{\mathrm{Hz}}$ for graphene antenna and 1.74 $\mu V/\sqrt{\mathrm{Hz}}$ for LT-GaAs antenna, corresponding to the current noises being 3.27 $pA/\sqrt{\mathrm{Hz}}$ and 9.3 $fA/\sqrt{\mathrm{Hz}}$. The current was firstly amplified by using a current preamplifier (SR570) with a 6dB band-pass filter and then input into a lock-in amplifier (7270), whose phase measurement resolution is in the range of 0.001° - 0.01° and whose gain was set to be 0 dB. Using the modulation frequency of 7.7 kHz, we can obtain the final noise $\frac{v_{n-in}}{6dB} \times \sqrt{0.0214 Hz} < v_{n-out} < \frac{v_{n-in}}{6dB} \times \sqrt{0.214 Hz}$. Based on these calculation, we estimated that the Johnson noise induced noise of graphene detection was in the range from 0.12 pA to 0.38 pA, while that of LT-GaAs detection was in the range from 0.34 fA to 1.08 fA. In that case, it is reasonable to consider the larger noise in graphene detection was caused by the Johnson noise.

5.2.3 Signal amplitude as a function of THz intensity and probe power

The relationship between the detected signal versus the intensity of incident THz wave, as represented by the electrical field applied to the THz emitter, and power of probe beam incident on the graphene area were also investigated, a linear relationship for both values was demonstrated.
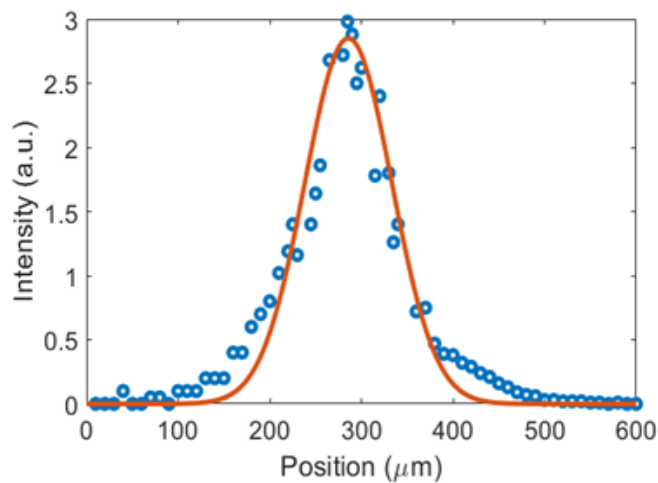
Figure 5.5 Profile of probe beam spot incident on THz detector, obtained by translating a knife-edge across the focal spot.

Before investigating the relationship, the power of probe beam present in the graphene area was first obtained. The profile of probe beam spot incident on the THz detector was first measured using a scanned knife-edge in front of a calibrated laser power meter; the data was then fitted using a Gaussian distribution. It was found that the diameter of the probe beam spot on the detector surface was around 67 µm. The results are shown in Fig. 5.5, in which blue circles show the experimental data, while the red solid line shows the fitting curve. Since the graphene area was a ~20 µm square, only

~20.3% of the probe beam power was incident on the graphene according to a calculation based on the (assumed) Gaussian distribution of the laser spot. In the following discussion, the probe power means the laser power incident on the graphene area instead of the power of the probe beam.
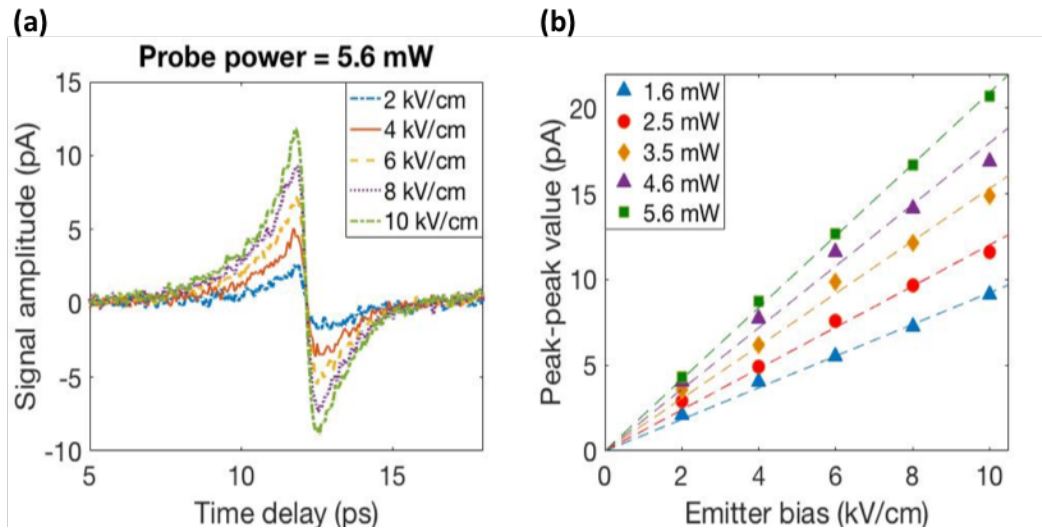
Figure 5.6 (a) Terahertz pulses detected at different emitter bias; (b) Relationship of signal amplitude vs. emitter bias.

Fig. 5.6 shows the measured THz signals for different emitter biases; the electric field applied in each case is obtained by taking the applied bias voltage and dividing by the dimensions of THz emitter gap (200 µm). Fig. 5.6(a) show the terahertz pulses generated with different emitter bias while probed with 5.6 mW probe beam, in which a significant signal increase was found with larger bias field applied on the THz emitter. The peak-peak values of the THz pulses were extracted and plotted with respect to emitter bias (Fig. 5.6(b)) to investigate their relationship further. The intensities of generated THz pulse and detected THz signal are linear, as was confirmed

by applying several probe beam powers. Furthermore, all curves in Fig. 5.6(b) with different probe powers converged to the same point, (0, 0), which agrees with expectations since the emitted THz wave is expected to be the reason for the charge movement in graphene detector.
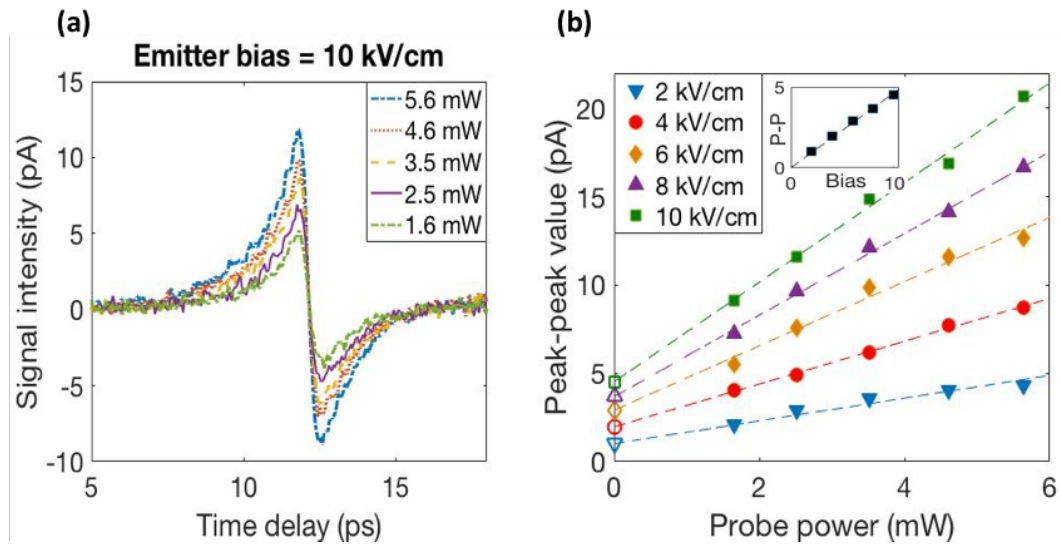
Figure 5.7 (a) Terahertz pulses detected at different probe power; (b) Relationship of signal amplitude vs. probe power; insert: relationship of emitter bias vs. intersections of y-axis and fitting curves.

The relationship of the THz signal with respect to probe power was also investigated and is shown in Fig. 5.7. Higher probe powers generate more photoexcited carriers, resulting in higher detection efficiency, as demonstrated in Fig. 5.7(a), where, for the same incident THz pulse, stronger probe beams induced a larger detected signal intensity. Fig. 5.7(b) shows the peak-to-peak values extracted from the THz time-domain signals as a function of probe power, in which the same colour represents the same incident THz intensity. A clear linear relationship can be seen from the fitting

curves in Fig. 5.7(b), indicating that the detecting efficiency was proportional to the probe power.

Values of the intersections of fitting curves and the y-axis in Fig. 5.7(b) were linear in the emitter bias, as shown in the insert of Fig. 5.7(b). The reason is that apart from the photoexcited carrier, the usual charge carriers in graphene were also accelerated by the electric field of THz pulse, inducing an additional current flow in the bowtie gap area. These carriers will not experience a recombination, and their interaction with THz wave should obey the Drude model as discussed in chapter 2.

5.3 Tunable broadband THz polarizer using graphene-metal hybrid stripe arrays

Up to now, tunable THz polarizers based on graphene device have only been demonstrated operating at a narrow bandwidth, though ultra-high bandwidth THz polarizers based on silicon-metal stripe arrays have previously been reported [203]. In this section, we sought to demonstrate a potentially improved geometry for a broadband THz polarizer based on graphene-metal stripe arrays, by replacing the silicon in [203] with graphene. The advantage of graphene in our device is that it can be electrically modulated, while the silicon device needs to be photon modulated.

Metallic wire-grid, the geometry of one of the most widely used polarizers, typically shows a low transmission for transverse electric (TE) polarized waves and a high transmission for transverse magnetic (TM) polarized waves. The same is true for wire grids formed from graphene, both in the

near-infrared [204], and in the microwave regions of the electromagnetic spectrum [205], while at THz frequencies, they typically show a low transmission for TM-polarized THz waves owing to THz wave-plasmon coupling [47]; this thus represents a limitation of pure graphene wire grid based polarizers. A further limitation is the low modulation (~10%) of the TE transmission, which is caused by Drude absorption [47]. In this section, the two drawbacks of graphene wire grid acting as THz polarizer were overcome by introducing metal patch arrays in the graphene wire grid. The introduction of metal patch arrays made graphene wire grid a better tuneable polarizer for three reasons. First, the introduction of metal makes the sheet conductivity of the graphene-metal hybrid wires larger than wires formed from graphene alone. In that case, we can get a larger Drude absorption and larger modulation of TE-polarized THz wave. Second, the strong TM-polarized plasmon mode present in graphene wires is suppressed by the introduction of the metal metasurface, which effectively acts to transform the graphene wires into separated graphene patches connected by metal. The EM wave-to-plasmon coupling efficiency of the graphene patches is determined by their dimensions, and for a certain width, the TM-polarized coupling is highly suppressed by decreasing the dimension of graphene [206]. Third, the metal introduces a TE-polarized plasmon into graphene, which also contributes to the THz transmission modulation [48]. The generated TE-polarized plasmon is induced by the THz wave coupling to the resonance of an inductive-capacitive (LC) circuit formed by the metal-graphene structure, in which the metal acts as a capacitive reservoir for charge accumulation and the graphene serves as an inductive channel.

5.3.1 Experimental methods

The geometry chosen for our graphene-metal hybrid terahertz polarizers was a wire-grid, with 25 μm stripe width and 5 μm stripe gap, whose strips were made up by graphene-metal arrays as shown in Fig. 5.8(a), in which θ is the angle between the polarization of incident terahertz wave and the direction of the strips, and $L_{graphene}$, L_{metal} and $\Lambda_{G/M}$ are the dimension of graphene, metal and period of graphene-metal arrays in the strips' direction, respectively. Five devices with different geometry parameters were designed, shown as the design value in table 5.1, in which the number of the device gives the designed period of graphene-metal arrays ($\Lambda_{G/M}$ in Fig. 5.8(a)). Among these five devices, Dev 30, Dev 90 and Dev 15 were designed to possess the same graphene filling factor, $L_{graphene}/\Lambda_{G/M}$, with different periods, $\Lambda_{G/M}$, aiming to reveal the factors that limit the bandwidth of the polarizer; while Dev 30, Dev 27.5 and Dev GS were designed having quite different graphene dimensions and filling factors, aiming to investigate how these aspects affect the modulation of the polarizer. All these considerations were also accessible from theoretical analysis, as will be discussed in section 5.3.2.
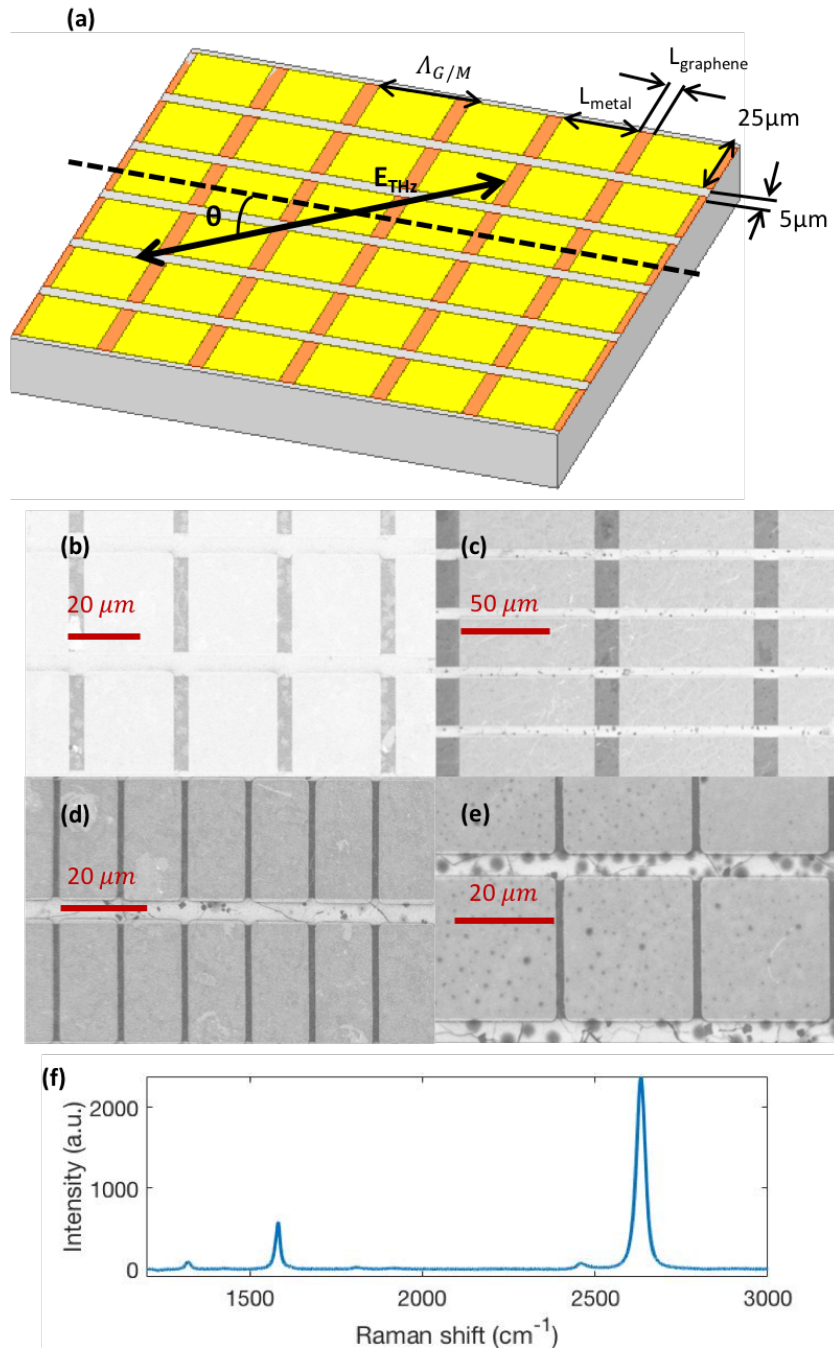
Figure 5.8 (a) Schematic of graphene-metal hybrid strips arrays. SEM images of metal arrays in (b) Dev 30, (c) Dev 90, (d) Dev 15, and (e) Dev 27.5. (f) Raman spectrum of graphene in polarizer.

Table 5.1 Geometric parameters of the tunable terahertz polarizers
fabricated in this work

Device	Data acquisition	$L_{graphene}$ (μm)	$\Lambda_{G/M}$ (μm)	Graphene Filling Factor
Dev 30	Design	5	30	1/6=0.167
	Measurement	4.1	29.1	0.141
Dev 90	Design	15	90	1/6=0.167
	Measurement	14	90.6	0.155
Dev 15	Design	2.5	15	1/6=0.167
	Measurement	1.7	15.1	0.113
Dev 27.5	Design	2.5	27.5	1/11=0.091
	Measurement	1.7	27.6	0.062
Dev GS	Graphene Strips Only			

The polarizers were fabricated on ST-cut quartz substrates and then imaged using an SEM, as shown in Fig. 5.8 (b)-(e). The quartz substrates were firstly OL-patterned using direct-write DLP laser lithography (MLA150, Heidelberg Instruments) and then electron-beam evaporated with Ti/Au (7nm/70nm) layers. The reason to choose this metal thickness was that it was not too thin, and larger than the terahertz penetration depth, which is about 50 nm for gold, avoiding the generation of unwanted plasmon in metal [207], while also being not too thick in order to reduce defects formed at the edge of the metal patches. After that, CVD graphene samples were transferred onto the metal arrays following a wet transfer procedure [99,

100], details of which have been discussed in chapter 3, and were then etched into stripe-array structures (25-μm-wide stripe and 5 μm space between stripes) using oxygen plasma. The graphene samples are CVD grown monolayer graphene on copper foil, which were purchased from the company "Graphene Supermarket". The devices were taken for Raman measurements after THz experiments and subsequent removal of the ion gel. One Raman spectrum of graphene in the polarizer (Dev 30) was shown in Fig. 5.8(f). Due to fabrication errors introduced by OL, such as the power distribution of laser spot inducing differences in the edge of the exposed pattern, and small errors in developing time inducing slight uncertainties, there was found to be differences in dimensions up to 1 μm between the fabricated devices and the designed parameters. The measured dimensions of the polarizers are different from the designed values, which were measured and listed in table 5.1. In the following sections, the measured dimensions instead of the designed ones were utilized in the calculations of device response for comparison with experiments.

The geometry of the integrated device is shown in Fig. 5.9(a). The two upper metal contacts which, respectively, connected to the two ends of each strips, were used to measure the DC conductance of the stripe arrays, which was then used to deduce the conductivity of graphene based on the geometry of the strips. The lower metal contact was used to supply a gate voltage, relative to the graphene strips, to modulate the Fermi level of graphene. Devices were electrically modulated by using ion gel as the gate dielectric material owing to its good transparency for terahertz waves [208] and the possibility to induce a large carrier density at lower gate voltage

compared with other dielectric materials such as SiO₂ [209]. The ion gel was a mixture of 2 [EMIM][TFSI]: 1 PVDF-HFP by weight, both of which were purchased. PVDF-HFP was first dissolved in acetone with the aid of a magnetic stirrer for an hour. Then, the [EMIM][TFSI] was added into the solution and stirred for a day. Ion gel was formed on the target substrate by drop casting and dried in ambient conditions for an hour [210].
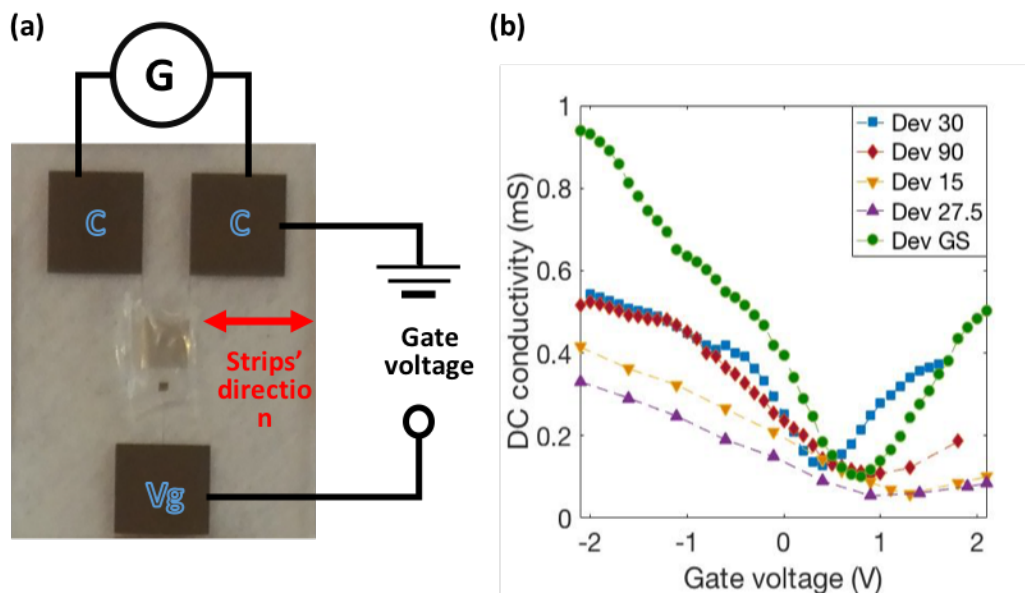
Figure 5.9 (a) Images of a fabricated device and the modulation method. (b) Measured DC conductivities of each device under the modulation of gate voltage.

Gate voltage dependent DC conductivities of graphene samples in each device were directly measured using a source-measurement unit (SMU), which were plotted in Fig. 5.9(b). The inconsistency of Dirac point and graphene's conductivity might be induced from the process of device

fabrication, which highly affected the quality of graphene samples and the contact resistance between graphene and metal.

5.3.2 Mechanisms of THz wave modulation

Two types of interactions between THz radiation and the carriers in the graphene are likely to be generated in the polarizers with graphene-metal-hybrid stripe arrays when illuminated by terahertz wave with a polarization direction parallel to the strips. First, the charge carriers will be accelerated by the terahertz electric field, moving freely along the length of the strips. Second, the carriers' collective oscillation (ie a plasmon) should be excited in the graphene due to carrier reflection at the interface of graphene and metal [48]. Both mechanisms will transfer THz wave's energy to charge carriers, reducing the transmittance of THz wave, and both should be affected by the conductivity of the graphene. Since the conductivity of graphene can be electrically modulated by a gate voltage, the transmittance of the hybrid stripe arrays is also tunable. In the parallel direction, both mechanisms are distinct, and the total modulation depth combines these two mechanisms [47]. In the perpendicular direction, noting that the movement of carriers is confined within the dimension of stripe width and no graphene-metal interface supports for carrier reflections in graphene, both mechanisms are highly suppressed.

To calculate the free carrier movement associated enhancement of transmittance modulation by introducing metal arrays in the graphene strips, the graphene-metal strips are treated as having a uniform conductivity, which is a reasonable hypothesis since the period of graphene-metal array is small

compared with the wavelength of THz wave. The sheet conductivity of the graphene-metal hybrid stripe will be given by:

$$\sigma = \left(\frac{L_{graphene}}{\sigma_{graphene} \times \Lambda_{G/M}} + \frac{L_{metal}}{\sigma_{metal} \times \Lambda_{G/M}}\right)^{-1} \qquad (5.1)$$

Where, $\sigma_{graphene}$ and σ_{metal} are the sheet conductivity of graphene and metal, respectively, and $L_{graphene}$ and L_{metal} are defined in Fig. 5.8(a). The frequency dependent conductivities of graphene were calculated based on the Drude model [174] in the following calculations. Since the sheet conductivity of metal is much larger than that of graphene, a good approximation can be written as follows:

$$\sigma \approx \left(\frac{L_{graphene}}{\sigma_{graphene} \times \Lambda_{G/M}}\right)^{-1} \qquad (5.2)$$

$$\Delta\sigma \approx \Delta\sigma_{graphene} / \left(\frac{L_{graphene}}{\Lambda_{G/M}}\right) \qquad (5.3)$$

According to formula 5.3, it is clear that, for a certain value of $\Delta\sigma_{graphene}$, a smaller graphene filling factor, $\left(\frac{L_{graphene}}{\Lambda_{G/M}}\right)$, leads to a larger conductance change of the hybrid stripes ($\Delta\sigma$), which directly results in a larger transmittance modulation, according to the relationship between THz transmittance and sheet conductivity, $t_{12} = 2n_1/(n_1 + n_2 + Z_0\sigma_s)$ [211], where n_1 and n_2 are the refractive index of the ion gel and quartz, respectively. The transmittance modulation depth was defined as $MD = (T_{max} - T)/T_{max}$, where T_{max} was the maximum transmission which was obtain when the conductivity of graphene reaches the minimum value (at the

Dirac point for example). Fig. 5.10(a) and (b) illustrate the calculated frequency dependent transmission with different graphene filling factors based on the view of free carrier movement, at the DC graphene conductivity of 0.15 mS in Fig. 5.10(a) and 0.75 mS in Fig. 5.10(b). The increasing transmission with higher frequency in the calculation corresponds to a decrease of AC conductivity with frequency, agreeing with the Drude model, while an increase of transmission with graphene filling factor is caused by the smaller conductivity of hybrid strips with larger graphene filling factor.
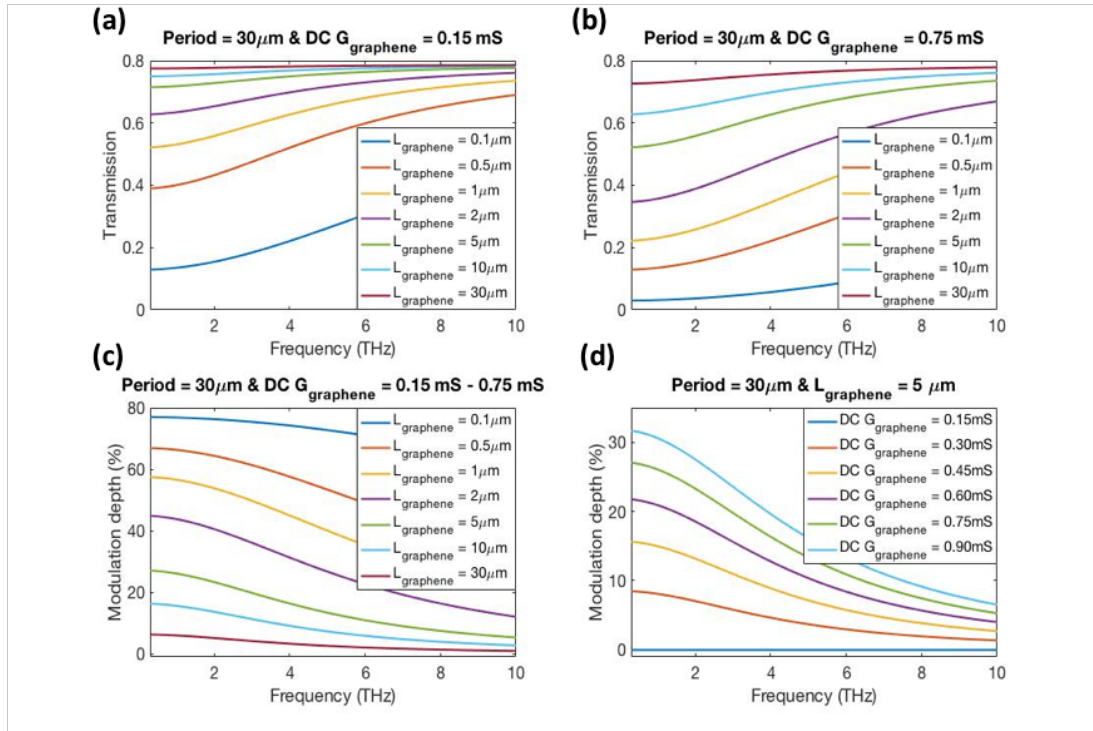
Figure 5.10 Free carrier movement induced transmission with different filling factors when the DC graphene conductivity is (a) 0.15 mS, and (b) 0.75 mS. Modulation depth with (c) different filling factors, and (d) different graphene conductivities.

Here, to illustrate the transmittance modulation, polarizers with different dimensions were investigated. The transmittance modulation depth was calculated using the values of graphene's conductivity changing from 0.15 mS to 0.75 mS. The calculated results were shown in Fig. 5.10(c), in which the graphene filling factors were calculated, by $L_{graphene}/\Lambda_{G/M}$, to be 1/300, 1/60, 1/30, 1/15, 1/6, 1/3 and 1. Clearly, the transmission depth was enhanced dramatically moving from smaller than 10% (filling factor = 1) to larger than 70% (filling factor = 1/300). Intuitively one would expect that a larger change in conductivity results in a larger transmittance modulation depth, which is also shown in Fig. 5.10(d), where the dimension of $L_{graphene}$ and $\Lambda_{G/M}$ are 5 μm and 30 μm, respectively.

Plasmon generation was demonstrated in the graphene area illuminated by a terahertz wave [48] (Fig. 5.11(a)) when introducing the metal arrays in the graphene. To calculate the transmittance modulation caused by the plasmons in graphene, an RLC equivalent circuit has previously been developed as shown in Fig. 5.11(b), and the details of calculation method were provided in the supporting information of Ref. [48]. This method is used for our calculations here because it was explicitly created for the calculation on the graphene plasmon-THz wave coupling, where the graphene samples were integrated with metal slab arrays, which are very similar to the structure of the hybrid stripes in our device. The resistance and inductance are proportional to the inverse of graphene's conductivity, while the capacitance is determined by the period of graphene-metal arrays and the graphene filling factors. In that case, the plasmon response will be modulated both by the conductivity and the polarizer's geometry.
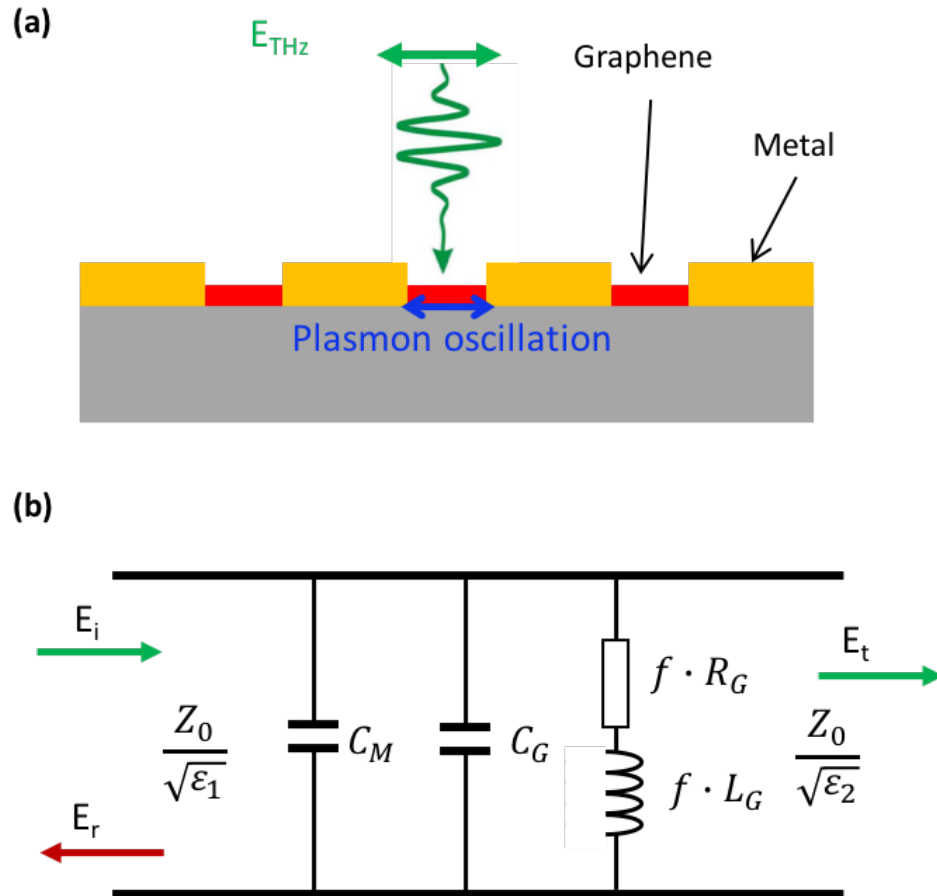
Figure 5.11 Diagram of (a) plasmon oscillation induced by terahertz wave in the graphene area, and (b) its equivalent circuit, taken from Ref. **[48]**.

Fig. 5.12(a)-(d) gave the calculated frequency dependent transmission and transmission modulation caused by plasmon with different graphene filling factors and different graphene conductivities. The transmission affected by the plasmon at different graphene filling factors is shown in Fig. 5.12(a), with DC graphene conductivity of 0.15 mS, and Fig. 5.12(b), with DC graphene conductivity of 0.75 mS. The resonant frequency of the plasmon, at the peak transmission, showed a blue shift as graphene filling factors decreased and graphene's conductivity increasing. The modulation depths

compared Fig. 5.12(a) and (b), were calculated by $MD = (T_{0.15mS} - T_{0.75mS})/$ $T_{0.15mS}$, with $T_{0.15mS}$ being the transmittance when conductivity of graphene is 0.15 mS and $T_{0.75mS}$ the transmittance when conductivity of graphene is 0.75 mS. The calculated results were shown in Fig. 5.12(c). Due to the blue shift of peak transmission frequency in graphene at larger conductivities, the $T_{0.75mS}$ was larger than $T_{0.15mS}$ in high-frequency range, inducing negative transmittance modulation ($MD < 0$). All the geometric parameters and conductivity values for calculations were the same as those used for Fig. 5.10, except for the geometry of graphene strips without metal arrays, which was not contained in Fig. 5.12 because no plasmon mode was generated in this arrangement. The modulation depth of the strip arrays with the geometric parameters of Dev 30 at different graphene conductivity was also calculated, as shown in Fig. 5.12(d). It can be seen that in the lower frequency range, the plasmon contributes to the enhancement of THz transmittance modulation, while at higher frequency range, the plasmon plays a negative effect.

Comparing Fig. 5.10(d) and Fig. 5.12(d), free carrier movements always exhibited a positive contribution for THz transmittance modulation, while plasmons showed a more complicated behavior, owing to the shift of plasmon frequency.
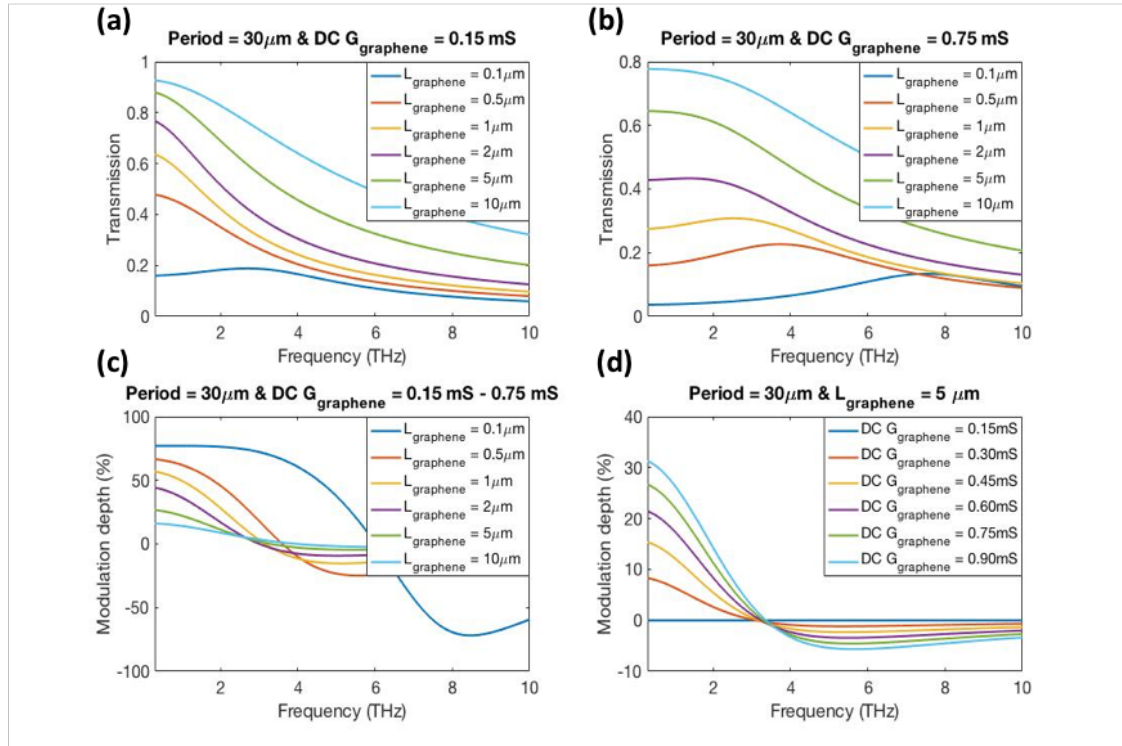
Figure 5.12 Plasmon-induced transmission with different filling factors when the DC graphene conductivity is (a) 0.15 mS, and (b) 0.75 mS. Modulation depths with (c) different filling factors, and (d) different graphene conductivities.

5.3.3 Direction dependent transmittance modulation

The graphene-metal hybrid strips arrays acted as a terahertz polarizer, whose minimum transmission appears when the strips are parallel to the THz polarization direction, while a maximum transmission appears when the strips are perpendicular to the THz polarization, as experimentally demonstrated in Fig. 5.13. This figure was plotted using polar coordinates, in which the angle represented the angle between the stripes of the polarizer and the THz polarization direction, shown as θ in Fig. 5.8(a). The distance of

the polar coordinate was normalized transmission $\left(T_{TM} - T_{pol}\right)/T_{TM}$ of the THz polarizer, where T_{TM} and T_{pol} are the transmission when $\theta = 90°$ and $\theta = 0°$, respectively. To create a practical tunable polarizer, the transmission of the polarizer should be electrically tunable in the parallel direction while unchangeable in the perpendicular direction with respect to the gate voltage, which is theoretically feasible according to the analysis in section 5.3.2.
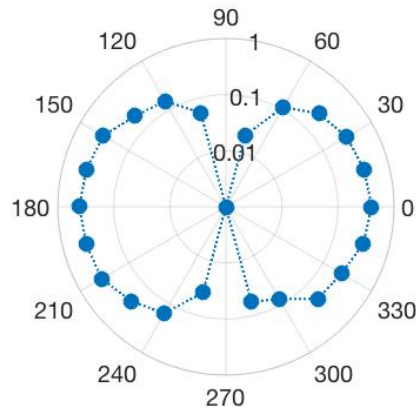
Figure 5.13 Direction-dependent transmission of the THz polarizer (Dev 30), where the angle was the angle between hybrid stripes and THz polarization, and the distance was the normalized transmission (at 0.5 THz) of the THz polarizer.

Dev 30 was firstly used for a gate-modulated transmittance measurement at different incident angles to study and experimentally confirm the angle-dependent modulation properties of the polarizer. To better understand the transmittance behaviors of the polarizers, frequency-domain signals were obtained using FFT for the following analysis. Incident angle was chosen to be 0°, 30°, 60°, and 90°, while gate voltages were incremented between -2.1 V and 0.4 V, since the Fermi level of graphene in Dev 30 reached the Dirac

point at 0.4 V according to a DC measurement (Fig. 5.9(b)). The reason that we limited the gate voltage at -2.1 V was that by using lower voltage the dark current in ion gel would be seen.
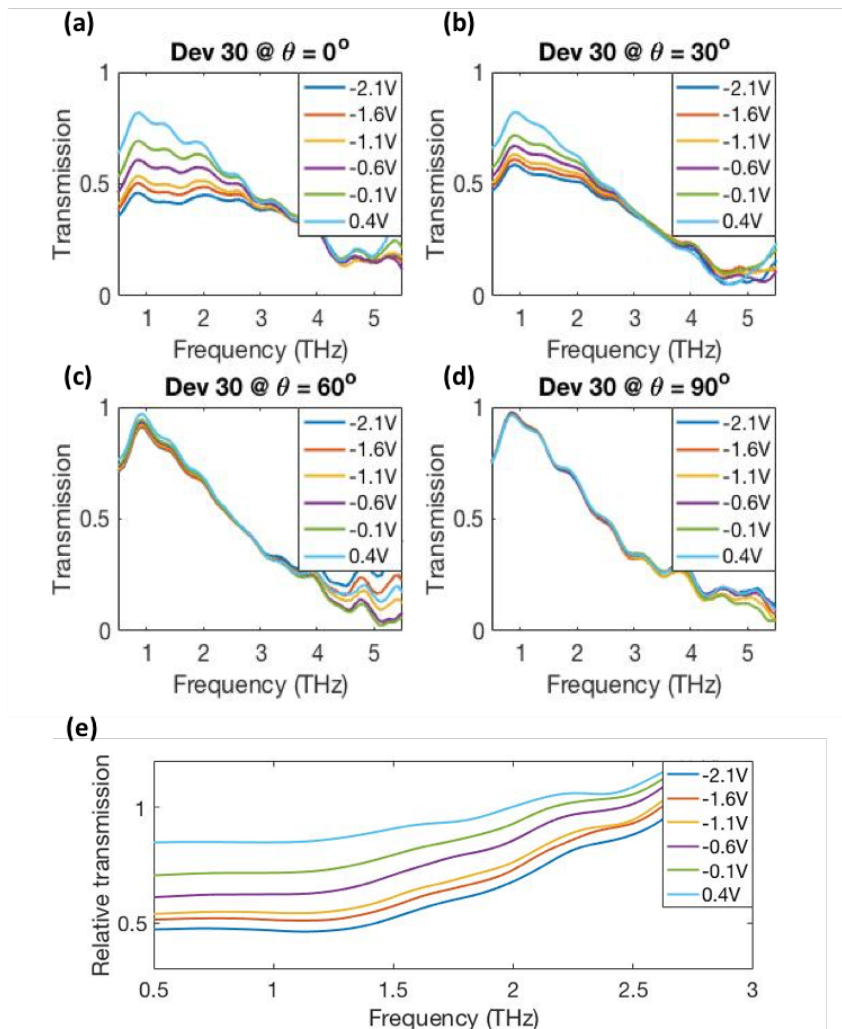
Figure 5.14 Direction-dependent transmission of the polarizer obtained by dividing the FFT information of transmitted THz pulse by the FFT information of reference THz pulse. θ gave the angle between hybrid stripes and THz polarization, and the transmission when θ= (a) 0°, (b) 30°, (c) 60° and (d) 90° were plotted in frequency domain. (e) gives the relative transmission obtained by T(0°) / T(90°)

The measured transmissions in frequency domain were obtained, as shown in Fig. 5.14(a)-(d). Significant transmission changes were seen in Fig. 5.14(a), in which the incident angle was 0º; the transmission changes gradually reduced with incident angle increasing until 90º, at which the transmission curves being modulated by different gate voltages overlapped, making the transmission change invisible. To highlight the difference transmission between different polarizations, a relative transmission obtained by $T(0°)/T(90°)$ was shown in Fig. 5.14(e), in which $T(0°)$ was the transmission in amplitude when $\theta = 0°$, and $T(90°)$ was the transmission in amplitude when $\theta = 90°$. It can be seen that the extinction ratio, which could be calculated by $20\log(T(90°)/T(0°))$ of the polarizer was also modulated.

To illustrate the angle-dependent modulation more clearly, the maximum modulation depths were calculated (Fig. 5.15) using $MD = (T_{max} - T_{min})/T_{max}$, where T_{max} is the transmission when $Vg = 0.4V$ and T_{min} is the transmission when $Vg = -2.1V$. The angle-dependent modulation depths at 1 THz in this group of experiments were directly plotted in the insert of Fig. 5.15. Clearly, the modulation depth in the parallel direction surpassed 40%, while the modulation depth in the perpendicular direction was negligible, as expected from the theoretical expectations detailed in section 5.3.2.
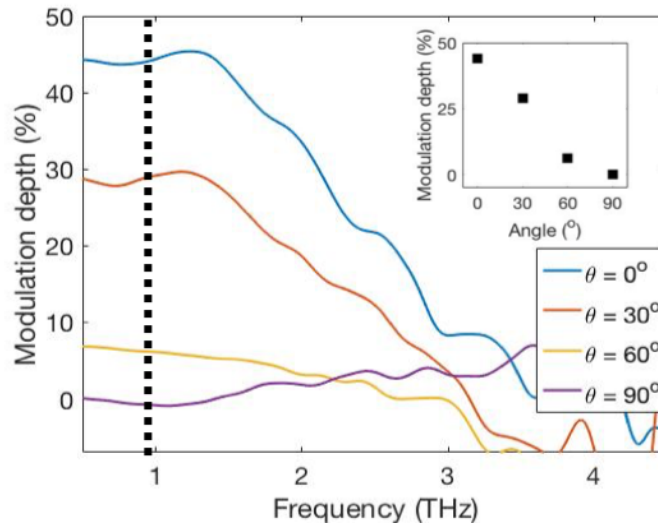
Figure 5.15 Modulation depth of Dev 30 when the angle, θ being defined above, was 0º, 30º, 60º and 90º.

An apparent transmittance modulation was reported for graphene strips arrays in the perpendicular direction, $\theta = 90°$ [47], which was also observed in the experiments on Dev GS, as shown in Fig. 5.16. Comparing Dev 30, Dev 90, and Dev GS, we found that the transmittance modulation in the perpendicular direction could be suppressed when $L_{graphene}$ getting smaller. This trend was shown in Fig. 5.16, in which the bold solid lines represented the modulation depth in perpendicular direction. For 25-μm-wide strip arrays, the transmittance modulation in perpendicular direction was negligible when the graphene length, $L_{graphene}$, was smaller than 5 μm, according to the experimental results shown in Fig. 5.16. The following discussions will focus on the transmittance modulation in the parallel direction $\theta = 0°$, since the modulation of the graphene-metal-hybrid stripe arrays in the perpendicular direction was negligible.
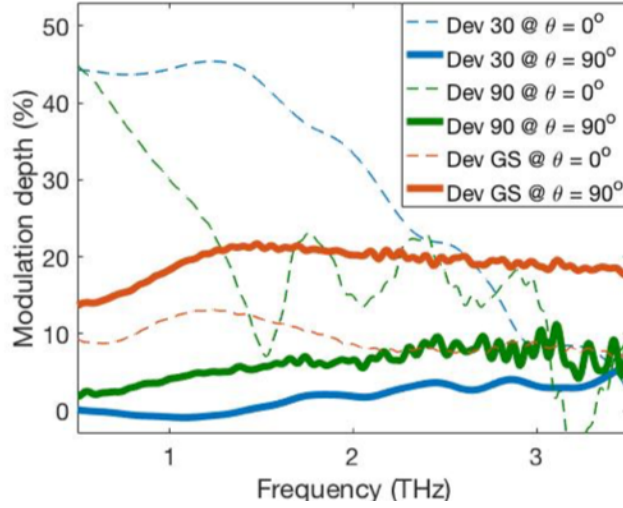
Figure 5.16 Comparison of modulation depth in parallel and perpendicular directions of Dev 30, Dev 90 and Dev GS.

5.3.4 Period limited bandwidth of modulation

Working bandwidth is an important factor for the polarizers in order to satisfy a broader range of applications. The primary limit for the bandwidth was the square metal patches array, which acted as a low-pass filter [212], whose cut-off frequency was determined by the geometries of the array.

To investigate the period-dependent working bandwidth, three devices with different periods, Dev 30, Dev 90 and Dev 15, were compared in both experiment (Fig. 5.17(a)) and calculation (Fig. 5.17(b)). The modulation depths given in these two figures were obtained by the transmittance modulation from $V_g=V_D$ (at Dirac point) to $V_g=-2.1V$. The modulation depth of the polarizers shown in Fig. 5.17(b) was calculated based on the method introduced above, considering the low-pass properties of metal arrays [212].

The bandwidth of Fig. 5.17(b) is similar to the bandwidth of the experimental data in Fig. 5.17(a), indicating that the geometry of the square metal patches was the dominate limit confining the bandwidth of the polarizers. To fabricate a broadband polarizer, a small graphene-metal period is needed. Among the fabricated devices, a largest bandwidth was obtained by using Dev 15, with a 15 μm period of graphene-metal array. The bandwidth of this device surpassed 5 THz, according to the experimental data, which covered the whole bandwidth of the TDS system being used.
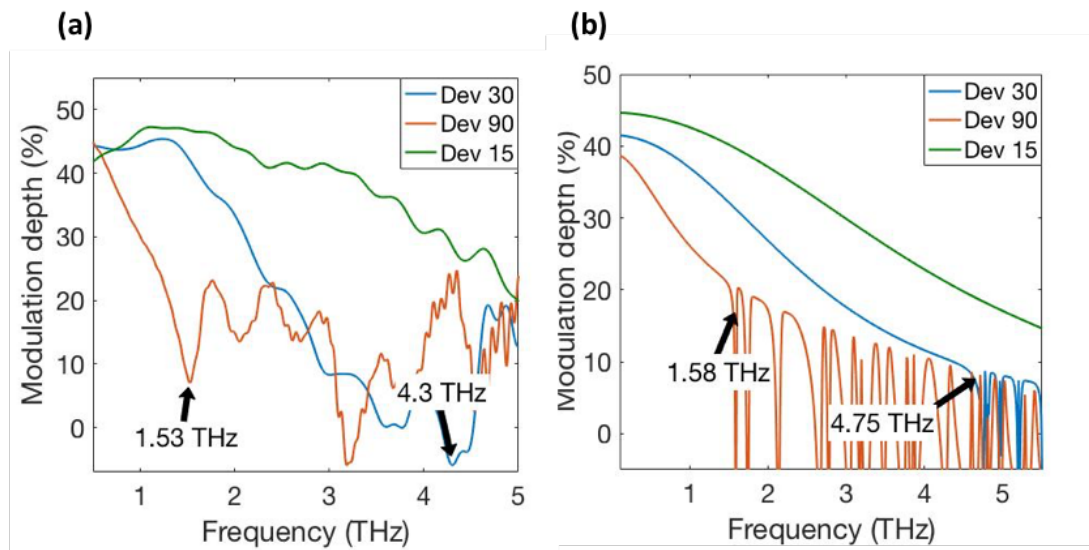
Figure 5.17 Modulation depths of Dev 30, Dev 90, and Dev 15 obtained by (a) experiment, and (b) calculation.

Comparing the experimental and theoretical transmission results, we note several differences, notwithstanding their overall similarity. First, the measured MD is up to ~3% larger than that calculated for low frequencies. This is likely to be a result of the contact resistance between graphene and

metal, causing the dc conductivity used in the calculation to be smaller than the sheet conductivity. Second, the measured MD decays somewhat more slowly with frequency than the calculated results. This could be caused by impurities and vacancies in the graphene, which may affect the optical conductivity and plasmon excitations [213] by the introduction of additional carrier scattering. Additionally, we observe a slight oscillatory behaviour in the experimental data, likely to be caused by interference of the THz pulse caused by the reflection the surfaces (substrate and ion gel). In addition, a more rapid MD decrease with respect to frequency was observed for frequencies above 3 THz in experiments owing to the limited system bandwidth, which rolled off beyond 3 THz.

5.3.5 Graphene dimension and filling factor determined modulation depth

To investigate the modulation enhancement by introducing graphene-metal hybrid structures, polarizers with different graphene filling factors were tested. The modulation depth of Dev 30, Dev GS and Dev 27.5 with gate voltage changing from V_D to -2.1 V were experimentally measured and theoretically calculated as shown in Fig. 5.18(a) and (b), respectively. Compared with Dev GS, in which no metal patches were introduced, a four times modulation enhancement was seen for Dev 30 and a six times modulation enhancement was seen for Dev 27.5, indicating that a smaller graphene filling factor induced a more considerable modulation. The polarization extinction ratio (PER) of Dev 27.5 was modulated from 3.7 dB to 10.3 dB obtained from $\mathrm{PER} = 20\log(T_{TM}/T_{TE})$, where T_{TM} and T_{TE} were the

TM transmission and TE transmission amplitudes, respectively. The maximum PER was obtained when $V_g = -2.1V$, and minimum when $V_g = V_{Dirac}$, which was 0.9 V for Dev 27.5.
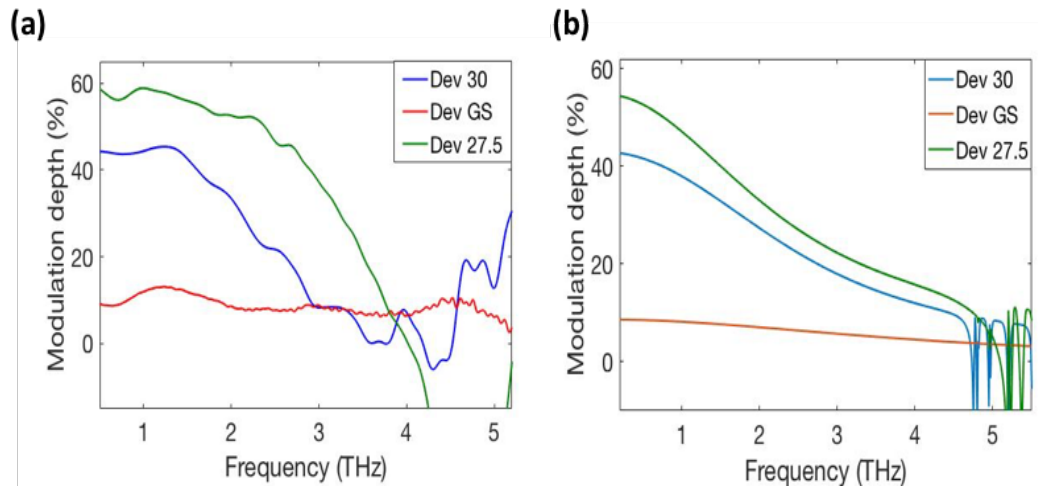
Figure 5.18 Modulation depth of Dev 30, Dev GS and Dev 27.5 with respect to frequency, obtained by (a) experiments, and (b) calculations.

An investigation was then taken to examine the relationship between the transmittance modulation and graphene's conductivity. Fig. 5.19 gave the modulation depth of the fabricated devices as a function of graphene's DC conductivity, in which 0.5 THz wave was utilized, with experiment and simulation result shown in Fig. 5.19(a) and (b), respectively. It is noticed that when the modulation of graphene's conductivity was small, the modulation depth and graphene's conductivity roughly obeyed a linear and proportional relationship. In order to give a numerical estimation on how much the modulation was enhanced, the slope of the curves of modulation depth versus conductivity was used as an indicator for representing the modulation

ability of the polarizers. The maximum modulation enhancement came from the device possessing the smallest graphene filling factors, Dev 27.5, while the modulation enhancement compared with graphene strips, Dev GS, was $2.06 \div 0.116 = 17.76$ according to the experiment and $1.84 \div 0.102 = 18.04$ according to the calculation.
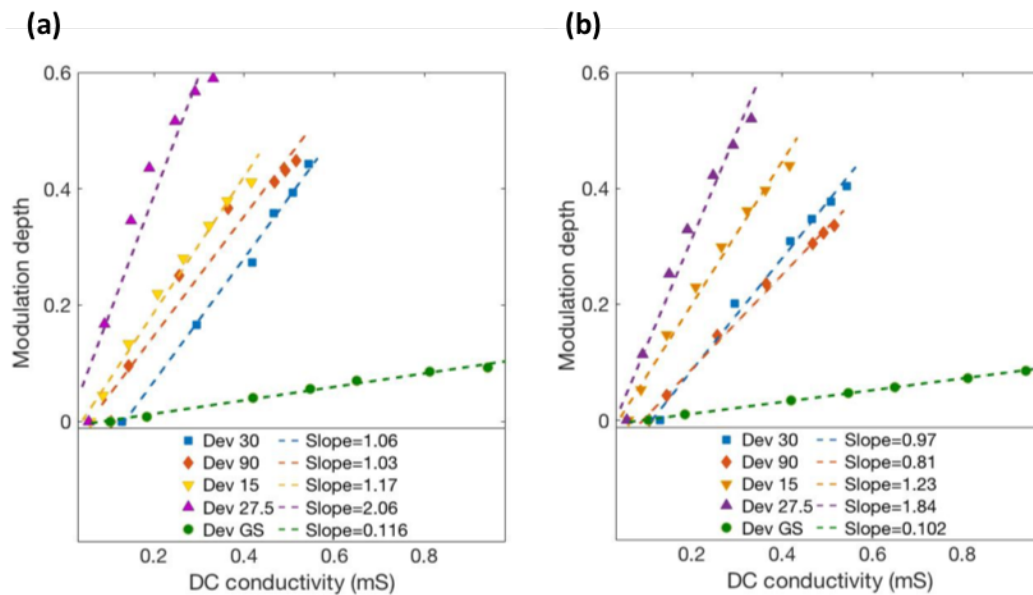
Figure 5.19 Modulation depth of Dev 30, Dev 90, Dev 15, Dev 27.5 and Dev GS with respect to graphene's conductivity obtained by (a) experiments, and (b) calculations.

Comparing the results of experiment theory, there were two consistent differences between them. First, the measured modulation depth was slightly larger than the calculated one. This was accounted to the contact resistance between graphene and metal, which caused the conductivity being utilized for calculation to be smaller than the real value. Second, the measured modulation depth decayed slower with respect to frequency than

the calculated results, especially in the low-frequency range. This may be caused by the defects and residues in the graphene area, which could induce additional plasmon-THz wave coupling modes. The resonant frequency of the plasmon is depend on the dimension of graphene, and smaller graphene inducing higher frequency of plasmon. In the case of these defects in the graphene introducing plasmon-THz wave coupling at higher frequencies, a slower modulation depth decrease with frequency should induced, as was observed.
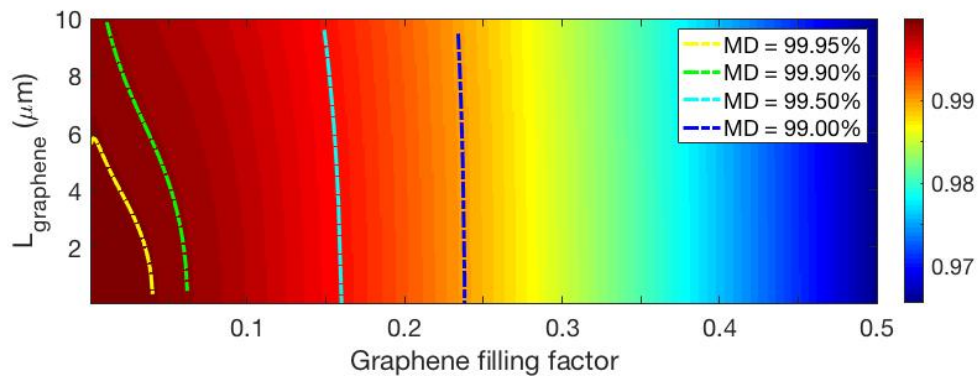
Figure 5.20 Modulation depth with respect to the length of graphene (ranging from 10 nm to 10 μm) and the graphene filling factors (ranging from 0.001 to 0.5), the MD value is indicated in the color bar.

The MD and the working bandwidth of the polarizer could be improved by further reducing the graphene filling factor and the $\Lambda_{G/M}$, which we investigated theoretically. Graphene dimensions were considered to be from 10 nm to 10 μm, noting that the former could potentially be realized experimentally using e-beam lithography. The graphene filling factors were set from 0.001 to 0.5 while the graphene conductivity was varied between

0.1 mS and 20 mS. The calculated MDs at 0.5 THz are shown in Fig. 5.20. Based on these parameters, the maximum MD found to be possible was 99.997%, employing 10 nm graphene with a 10 μm period.

Table 5.2 Performance of THz polarizers producing a 99.9% modulation depth for different geometric parameters

Geometry	$L_{graphene}$ (μm)	GFF	$\Lambda_{G/M}$ (μm)	Max / min transmission	Cut-off frequency (THz)	Min / max PER (dB)
1	0.1	0.064	1.56	0.557 / 5.85E-4	91.3	4.5 / 62
2	0.5	0.062	8.06	0.55 / 5.50E-4	17.7	4.7 / 63
3	2.3	0.059	38.98	0.499 / 5.00E-4	3.66	5.5 / 64
4	4.0	0.052	76.92	0.389 / 3.91E-4	1.85	7.7 / 66
5	6.0	0.037	162.16	0.202 / 2.01E-4	0.88	13 / 72

Aside from the MD, other performance parameters such as the bandwidth and transmission of the polarizer also change when the geometries are changed. To investigate this, several different geometries were investigated, realized to obtain a range MDs as shown in Fig. 5.20; the results are summarized in table 5.2. It can be seen that either a shorter $L_{graphene}$ or larger graphene filling factor results in a broader bandwidth (reaching as high as >90 THz for geometry 1 in table 3), while smaller graphene filling factor results in smaller TE transmission, indicating a higher PER (eg. up to ~70 dB for geometry 5). The possible PER of our design is up to 30 dB higher than commercial metal wire grid THz polarizers (20 – 40 dB). By a suitable choice

of geometry, the proposed polarizers can thus target either maximal bandwidth, maximal PER, or a compromise between these factors according to the needs of particular applications.

5.4 Conclusion

In this chapter, a graphene bowtie antenna was demonstrated to acts as a promising THz detector for free-space pulses. Then, this chapter demonstrated enhancement in the direction dependent modulation of broadband tunable THz polarizer, by introducing graphene-metal hybrid structures into the polarizer's strips, which both increased the effective conductivity of the strips and introduced plasmons in the graphene area. The bandwidth of this polarizer has the potential to cover the whole THz range, making it satisfy all kinds of THz sources requiring polarization control. Both of these pieces of work can contribute to the expanding range of applications for graphene in THz technology.

Chapter 6 Surface acoustic wave induced carriers transport in graphene channels

6.1 Chapter introduction

The interaction of SAWs with two-dimensional electron systems has received much attention. The moving sinusoidal electric field which accompanies SAWs can drag with it charge carriers which then drifting in the propagation direction of the SAWs, which is known as the acoustoelectric effect, as first discussed by Parmenter [214] and subsequently experimentally realized by Weinreich [215]. The charge carriers drifting in a 2DES by the acoustoelectric effect generates direct current or voltage, which has been experimental observed [216, 217, 218]. Later, quantized acoustoelectric current with the value of nef was achieved [219, 220], where n is the number of charge carriers trapped in one potential cycle, e is the elementary charge, and f is the frequency of the SAWs. Furthermore, increasing the charging energy in the electron system by means of quantum dots [221, 222] and by counter-propagating SAWs [223], has been demonstrated, effectively improving the accuracy of the quantized current.

The acoustoelectric interaction of SAWs with graphene has also received much attention, owing to the unique electronic properties of this two-

dimension material [224]. The pioneer experimental work on the detection of acoustoelectric current in graphene for the first time was made in our group by using CVD graphene on 128° Y-rotated LiNbO$_3$ [82]. Many factors, such as SAW frequency [225, 79], temperature [83], dimension of graphene channel [79], photoexcitation [85, 81], chemical doping [86], electrical doping [80, 226], and properties of substrate [227, 228], have subsequently been shown to affect the value of the acoustoelectric current in graphene by other groups. The graphene AE device is an interesting research topic, which involves both fundamental interests [229, 230, 231] and useful applications [89, 224].

In this chapter, graphene AE current experiments working at the frequency of 100s of MHz, realized in our group before, were firstly repeated. After that, three directions were pursued, all pushing towards new regimes of device operation, and motivated by the long term goal of obtaining devices in which a quantised acoustoelectric current might be observed in graphene: (1) fabrication and measurement of graphene AE devices working at higher frequency (~1.87 GHz), (2) investigation of the properties of graphene AE devices at low temperature, and (3) investigation of electrically tuneable graphene AE devices. AE current influenced by carrier localization behaviour was observed using AE devices with graphene nanoribbons as the carrier transport channel.

6.2 Acoustoelectric current in graphene

6.2.1 Experimental methods

A similar geometry of graphene AE device as in Ref. [82] was first utilized to confirm I could make and measure devices in which a DC current was generated in graphene by SAWs, as shown in Fig. 6.1. The SAW delay lines were fabricated following the recipes discussed in chapter 3. The CVD-derived graphene was then transferred directly onto the highly piezoelectric $LiNbO_3$ substrate in the middle of the two IDTs. Six electrodes were then made on top of the graphene using optical lithography and thermal evaporation. The sizes of the electrodes are shown in Fig. 6.1, where L is the length of the electrodes, l and D are the distance between electrodes in the directions along and vertical to the SAW propagating direction, respectively, and d is the width of the electrodes. The wavelength of IDTs was 17.6 µm, corresponding to the resonant frequency of 215 MHz according to the measurement shown in chapter 3.

A network analyzer was used to supply the radio-frequency (RF) signal for the IDTs, and a Keithley 2410 SMU was used to measure the generated AE current. The network analyzer and SMU were both controlled using LabView. A small burden voltage was generated by the SMU which brings an offset to the measured data. Thus, all the AE current data shown in this chapter had an offset subtracted in the data processing.
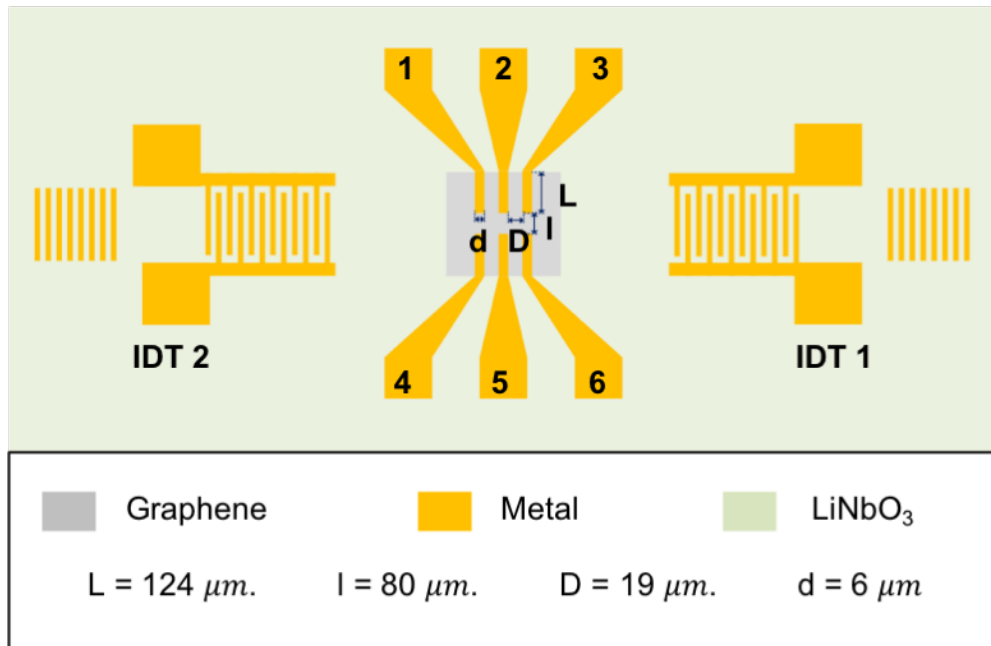
Figure 6.1 Schematic diagram of graphene AE devices.

6.2.2 Performance of graphene AE device

SAW-induced carrier transport was confirmed by comparing the measured current and the response of the SAW delay line in the frequency domain, as shown in Fig. 6.2, where the features of these two signals agreed, indicating the AE current was indeed excited by the SAWs. The number of electrodes is indicated in Fig. 6.1. IDT1 and IDT2 show the AE currents being generated by the left IDT and right IDT, respectively. The AE current peaked at around 215 MHz with a peak value of more than 1μA when a 10 dBm RF signal was applied to the IDT. Additionally, two current peaks appeared at around 207 MHz and 222 MHz, corresponding to the frequencies of secondary transmittance peaks of the SAW delay line response. The directions of the AE current were found to be the same as that of the SAWs propagation, confirmed with both IDTs, and indicating p-type

charge carriers transported in the graphene. P-type doping is typically observed in CVD graphene after the PMMA supported transfer due to residues and atmospheric adsorbents [232].
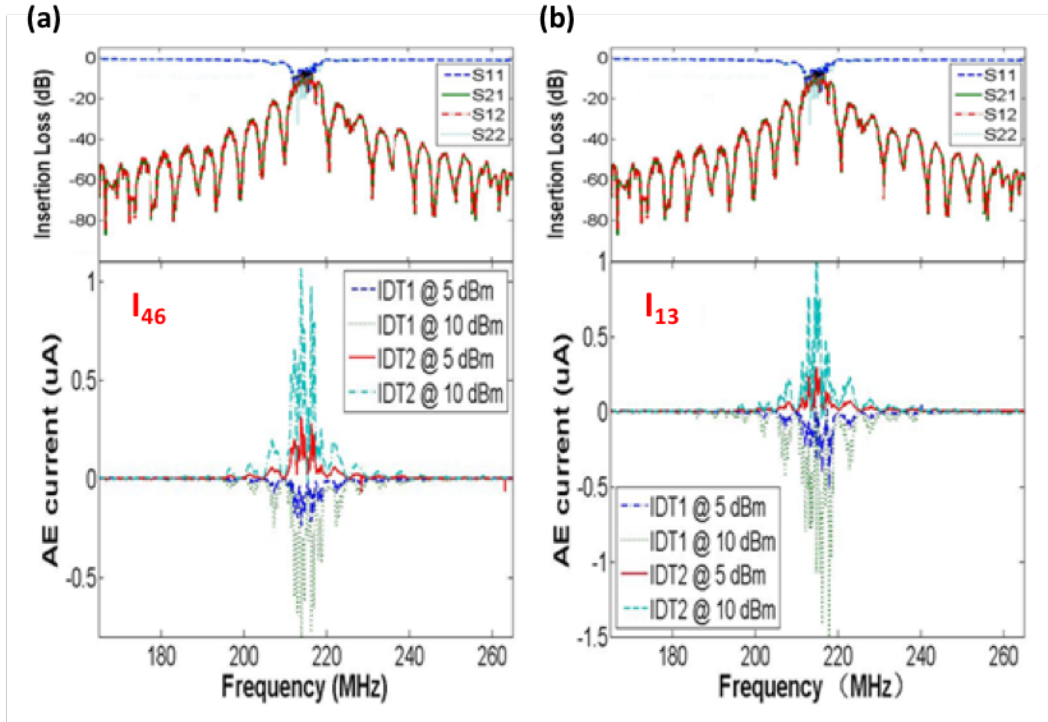
Figure 6.2 AE currents generated by IDT1 and IDT2, respectively, were measured at room temperature using electrodes (a) 1 and 3, (b) 4 and 6, comparing with the SAW delay line response (upper figures).

The amplitude of the AE current varied linearly with the SAW power, as shown in Fig. 6.3. In this figure, the x-axis is the power of RF signals applied on the IDT, and the y-axis is the peak value of the AE current. This result agrees with a relaxation model [224, 233], $I_{ae} = -\mu \frac{P_{SAW}}{v_{SAW}} \alpha$, where I_{ae} is the AE current, μ is the carrier mobility, P_{SAW} is the SAW power, v_{SAW} is the velocity of SAW, and α is the SAW attenuation ratio.
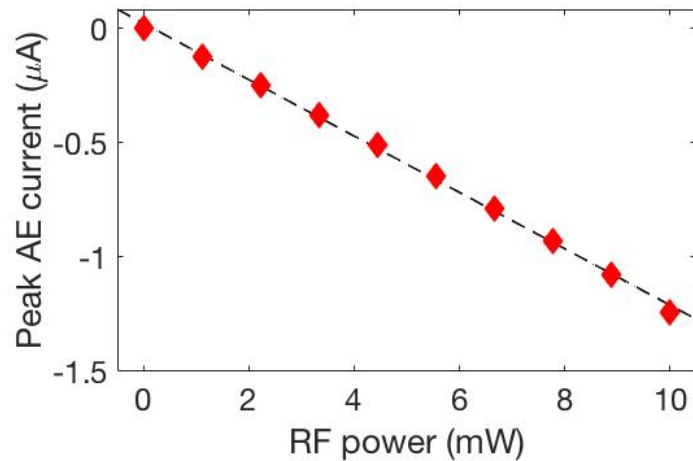
Figure 6.3 Linear relationship of AE current and RF power applied on the IDT.

It is noticeable that large oscillations are superimposed on the AE current curve around the region of the resonant frequency and they were not symmetric although the design was. To identify the origin of these fluctuations, some comparison of features were made using the curves of normalized AE current with respect to SAW frequency, as shown in Fig. 6.4. Fig. 6.4(a) and (b) compare the AE current features pumped at different powers. It can be seen that under the conditions of the same IDT and electrodes for measurements, the shape of the AE current as a function of frequency is independent of the RF power. Fig. 6.4(c) compares the AE current profile as a function of frequency measured using different electrodes while the SAW conditions were kept the same, while Fig. 6.4(d) compares the AE current profile as a function of frequency pumped by different IDTs while using the same electrodes to the graphene for measurement. Significant differences in the measured profiles were seen in both figures,

owing to two phenomena: RF pick-up [234] and SAW reflections from sample edges or the second transducer [220].
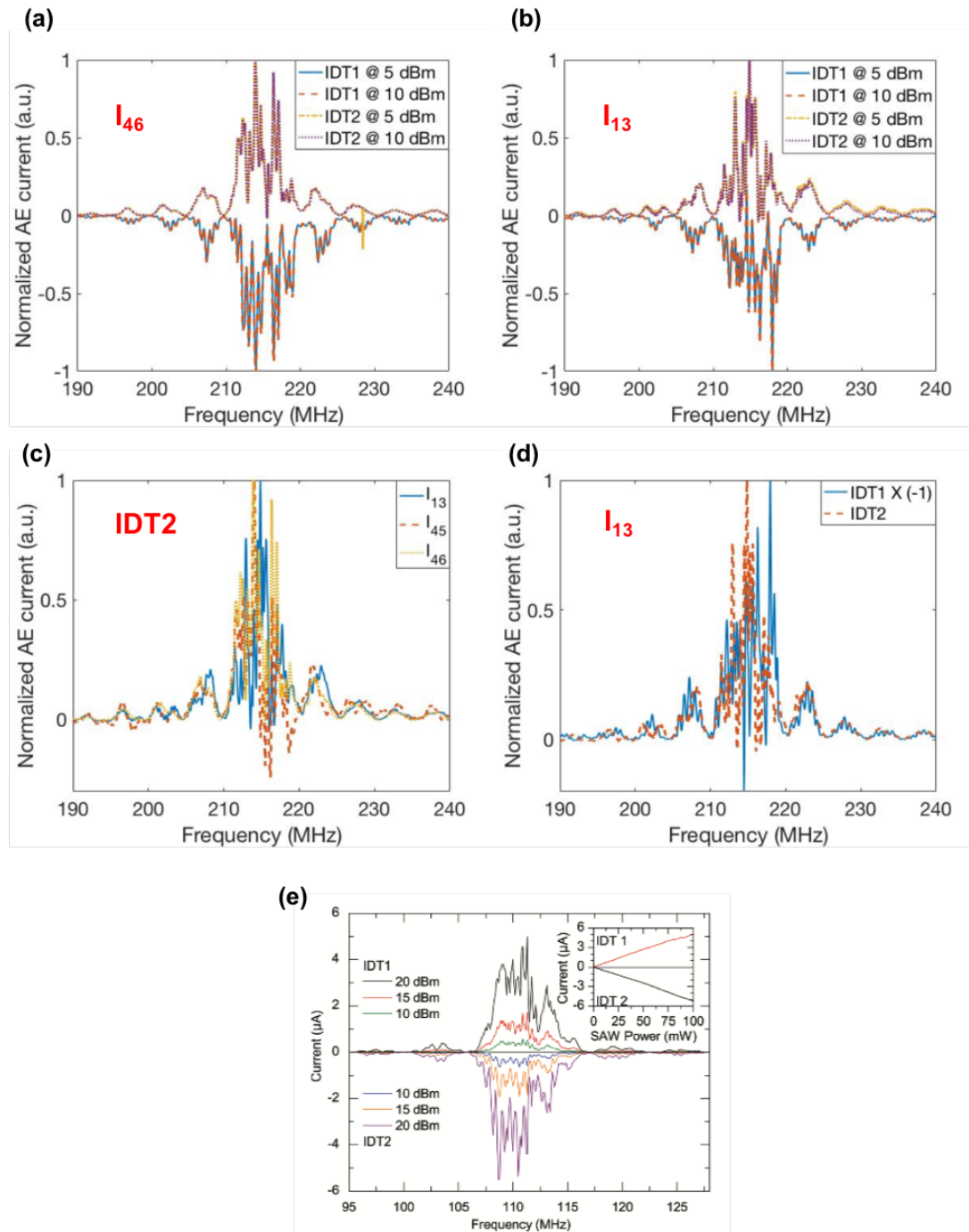
Figure 6.4 Comparisons of the AE current features under the conditions of (a) and (b) different SAW power, (c) different electrodes, and (d) different IDTs, where the number IDTs and electrodes were shown in Fig. 6.1. (e) AE current in graphene obtained in our group by V. Miseikis **[82]**.

For a comparison, previous measurements in our group using a similar device but working at ~ 110 MHz were shown in Fig. 6.4(e), which has been pulished in Appl. Phys. Lett. [82]. Random oscillations were also seen in these data. On the other hand, the efficiency of my device was higher than the previous device, owing to the higher working frequency of my device.

6.2.3 Graphene AE device at an expanded range of frequency

Two graphene AE devices working at the resonant frequencies of 110 MHz and 1.87 GHz were fabricated and tested. AE current for these two devices are shown in Fig. 6.5(a) and (b), respectively. The AE current for both of these two devices was also found to be linear in the SAW power, as shown in Fig. 6.5(c) and (d) using the value of peak AE current. Noticing that the values of current were much smaller than the current generated using the 215 MHz device; the likely reason is the lower coupling efficiency of the SAW delay lines confirmed by the SAW response measurement shown in Fig. 6.6. It is noticing that the background of the insertion loss in 1.87 GHz device (~ -50 dB) was much larger than that in 110 MHz device (~ -90 dB). This was caused by the cross-talk effect, which will be more significant for shorter wavelength devices.
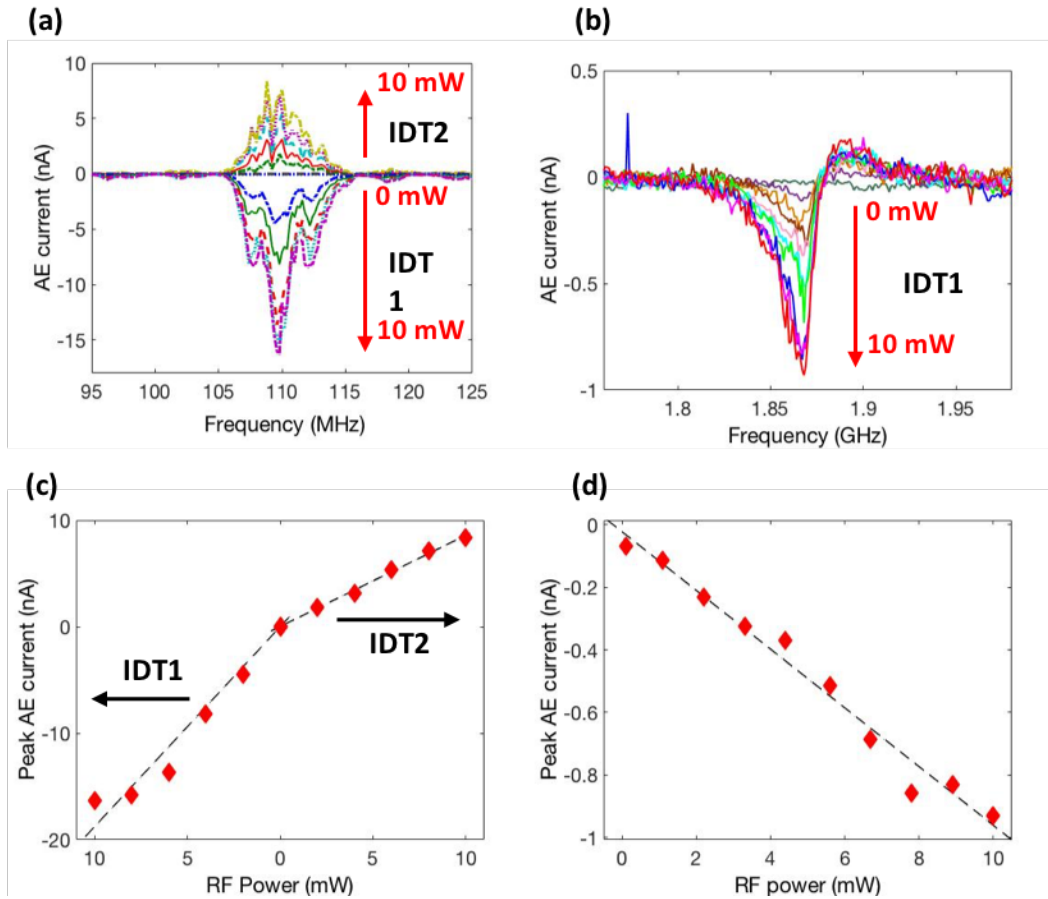
Figure 6.5 AE current excited by IDTs with a resonant frequency of (a) 110 MHz and (b) 1.87 GHz, whose linear relationship with the RF power is shown at (c) 110 MHz and (d) 1.87 GHz, respectively.
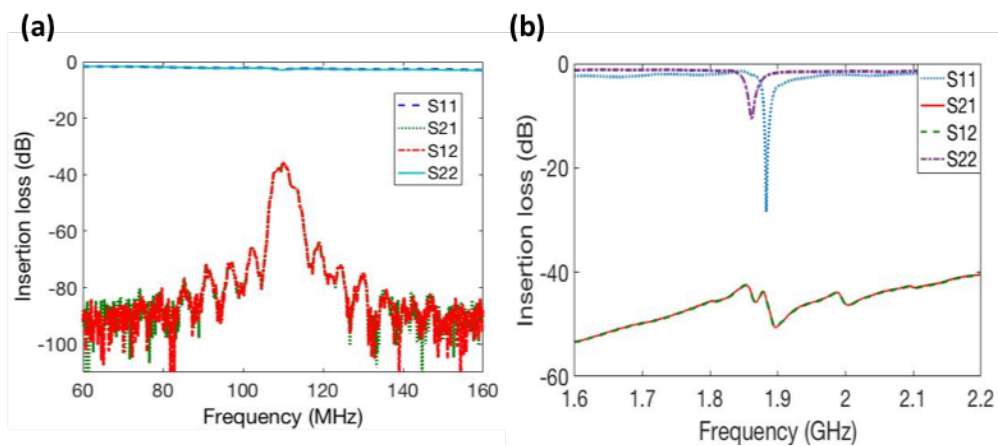
Figure 6.6 SAW delay response of the graphene AE devices working at the resonant frequency of (a) 110 MHz and (b) 1.87 GHz.

6.3 Temperature dependent acoustoelectric current in graphene channel

6.3.1 Temperature dependent AE current in bar graphene channel

The temperature affects the acoustoelectric current for two reasons. Firstly, the velocity of SAWs is larger at low temperatures, inducing a frequency shift to the SAW delay line response and the corresponding features in AE current correspondingly. Secondly, the conductivity of graphene is a temperature dependent value [235, 236, 233, 237], resulting in a change in the AE current. Fig. 6.7 shows the measured AE current for different temperatures using a graphene AE device with a graphene channel forming a 100-µm-width bar, and with a 214 MHz SAW delay line, excited by a 10 mW RF signal. A close-up view of the peak current was shown in the insert of Fig. 6.7, showing a significant frequency shift for different temperatures.
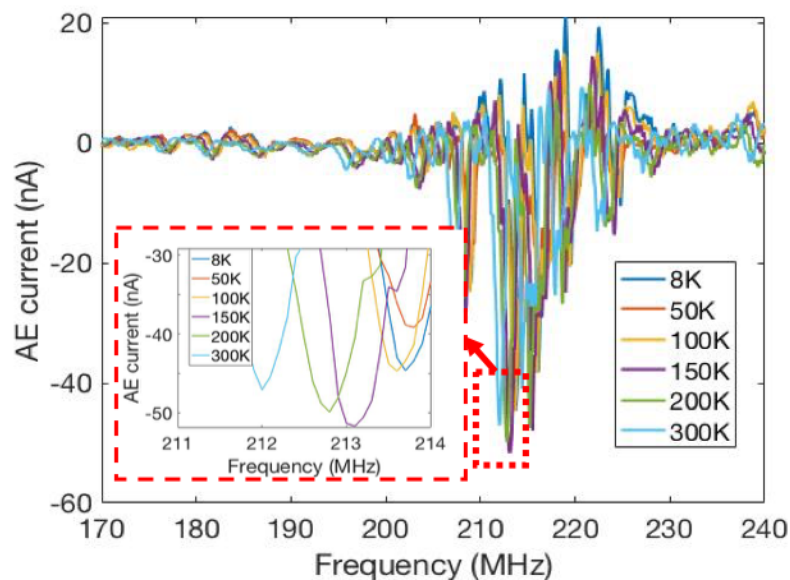
Figure 6.7 AE current at different temperatures, insert: close-up view of the peak current region.

To reveal the temperature induced frequency shift more clearly, the frequencies of the peak current were extracted and plotted with respect to temperature, as shown in Fig. 6.8. Since the lithium niobate has a higher SAW velocity at lower temperature, which obeys a linear relationship [238], a blue shift of the resonant frequency of AE current would be seen as the temperature decreases, which was illustrated in Fig. 6.8. ~1.8 MHz of frequency offset was obtained when the temperature decreasing from 300 K to 8 K.
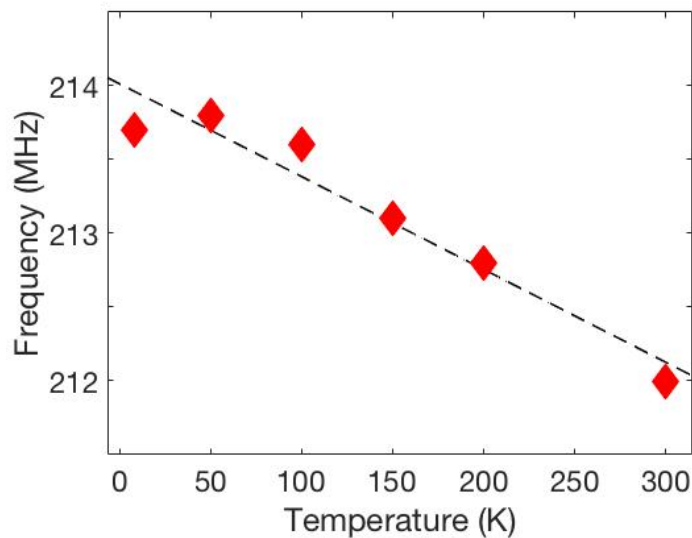
Figure 6.8 Temperature dependent frequency of the peak AE current.

The amplitude of the AE current at different temperatures is shown in Fig. 6.9. Quite small current changes were seen in this measurement owing to the conductivity of large area graphene (> 1 μm) with the Fermi level away from Dirac point varying only slightly with temperature [235, 236]. The little fluctuation of the current with respect to the temperature might be caused by

change of IDTs' coupling efficiency owing to the temperature-dependent resonant frequency shift.
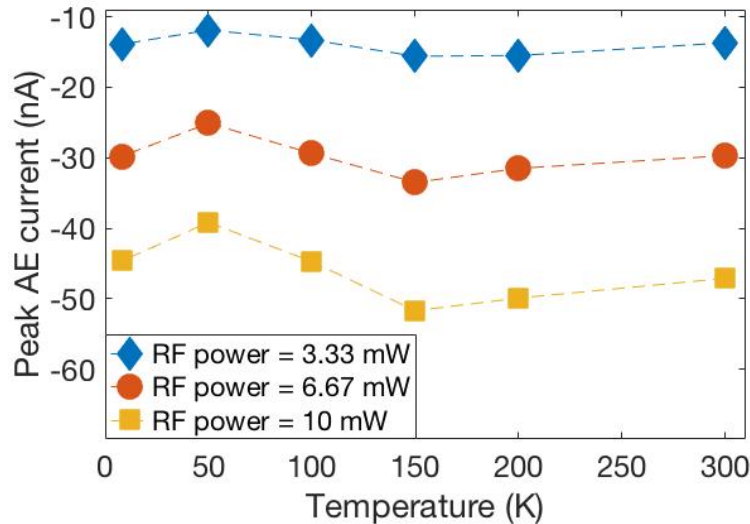
Figure 6.9 Temperature dependent amplitude of the AE current.

6.3.2 Carrier localization feature of AE current in graphene nanoribbon

When the dimension of graphene goes approaches the nanometer scale, potential barriers in graphene induced by grain boundaries, tears, wrinkles, charged impurities, edge disorder and band gap open [239, 84, 240, 241, 55, 242] and can become significant. Then, the conductivity of graphene decays exponentially with the increase of 1/T. On top of that, when the temperature is smaller than the potential barriers, $k_B T < P_{barrier}$, carriers localization was seen in graphene and the conductivity of graphene nanoribbon decays slower than it at higher temperature [237], which has been demonstrated as shown in Fig. 6.10.
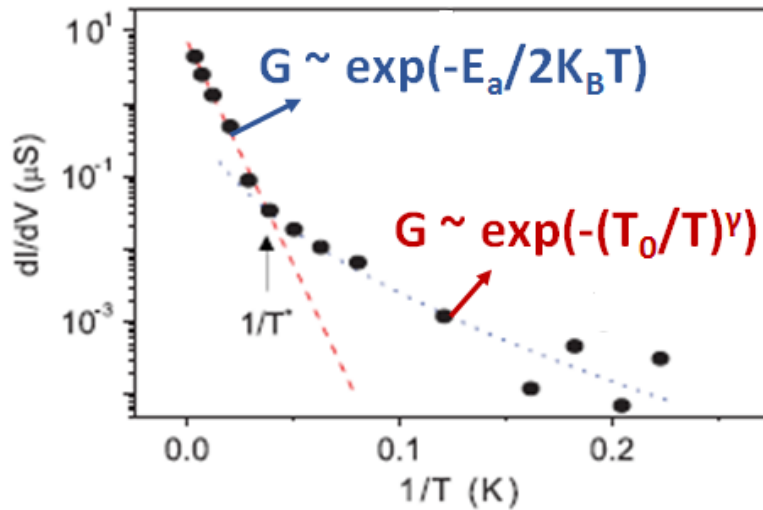
Figure 6.10 Demonstration of carrier localization in graphene nanoribbons, taken from Ref. **[237]**

The AE current is roughly linear to conductivity of the carrier transport channel when the channel conductivity is much smaller than the characteristic conductivity [224]. The characteristic conductivity can be calculated by $\sigma_M = v_{SAW}(\varepsilon_1 + \varepsilon_2)$, which is ~ 1 µS in the graphene AE device on LiNbO$_3$. A DC measurement by using Keithley 2410 showed that the conductivity of graphene channel at low temperature in the device used in this section (shown in Fig. 6.11) was about an order lower than the characteristic conductivity of this device. This suggests that the two-segment feature of the temperature-dependent conductivity shown in Fig. 6.10 should also be observed in the temperature-dependent feature of AE current generated in graphene nanoribbons.
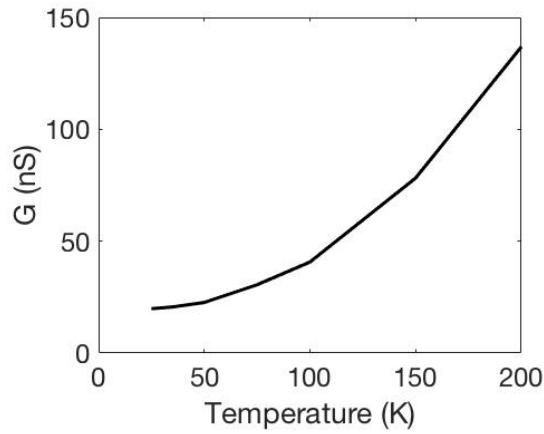
Figure 6.11 DC conductivity of graphene channel as a function of temperature.
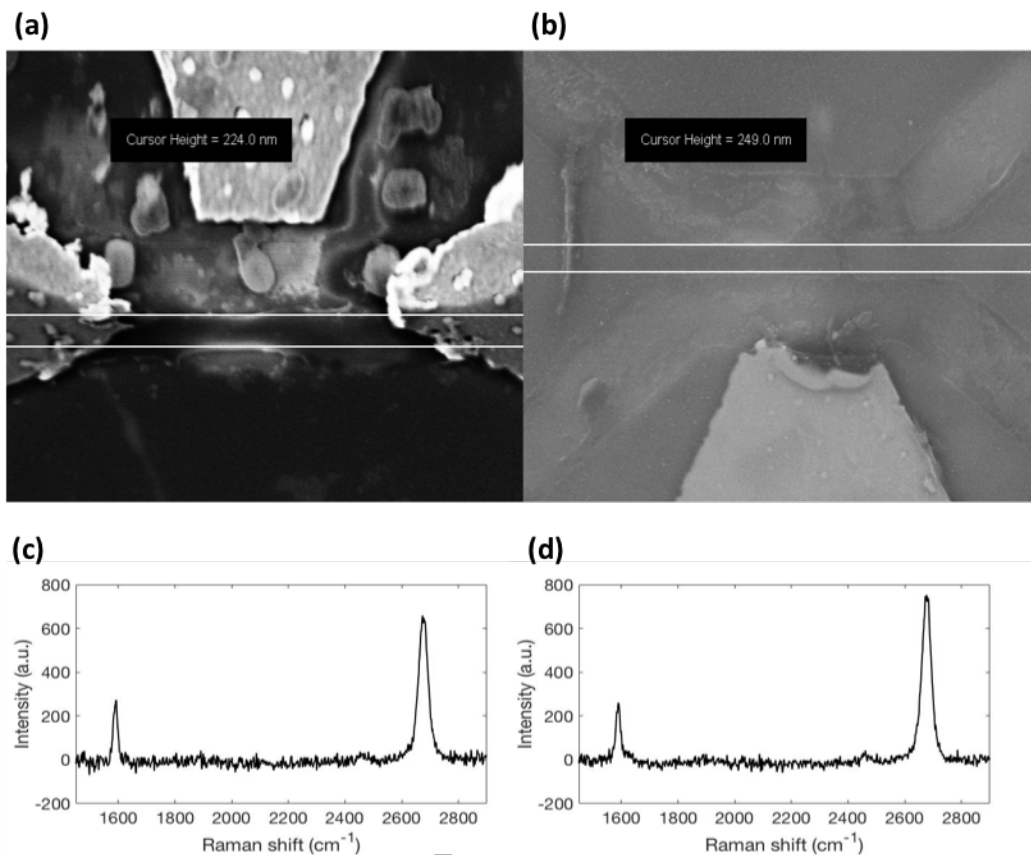
Figure 6.12 EBL images of the graphene channels in the two graphene AE devices with the channel width of (a) 224 nm, and (b) 249 nm, and the Raman spectra of these two devices plotted in (c) and (d), respectively.

Two graphene AE devices with graphene channels of width of around 200 nm were fabricated between two IDTs, whose EBL images are shown in Fig. 6.12 (a) and (b); their Raman spectra are shown in Fig. 6.12 (c) and (d), in which the background Raman signals of LiNbO3 were subtracted.

The device in Fig. 6.12(a) was utilized for the low-temperature AE experiments. Examples of the raw measurement are shown in Fig. 6.13 – Fig. 6.15, where Fig. 6.13 gives the SAW delay line response for different temperatures; the subsequent figures give the measured AE current at different temperature under the experimental conditions of IDT1 being supplied 5 mW of RF power (Fig. 6.14), IDT1 with 10 mW of RF power (Fig. 6.15). Since the amplitudes of the current obtained were in the sub-pA to pA level at low temperature, a current pre-amplifier was used to obtain these data.
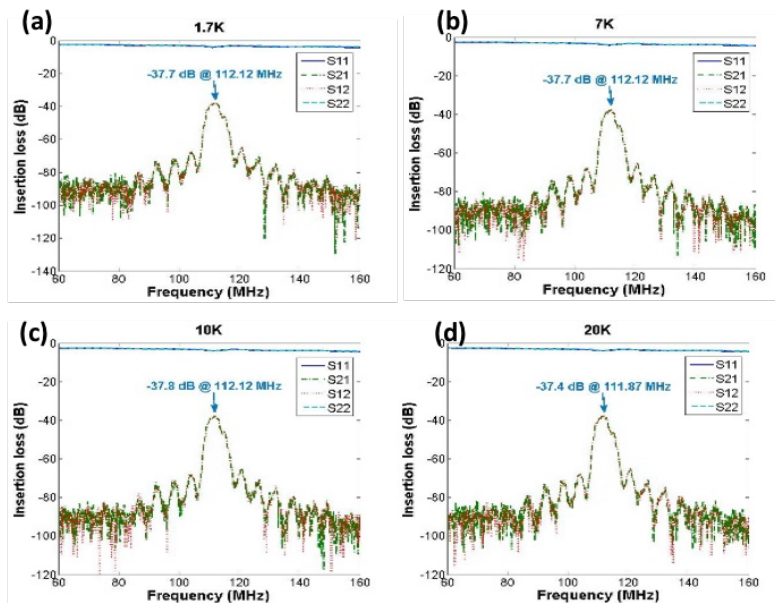
Figure 6.13 SAW delay line response at a temperature of (a) 1.7 K, (b) 7 K, (c) 10 K, and (d) 20 K.
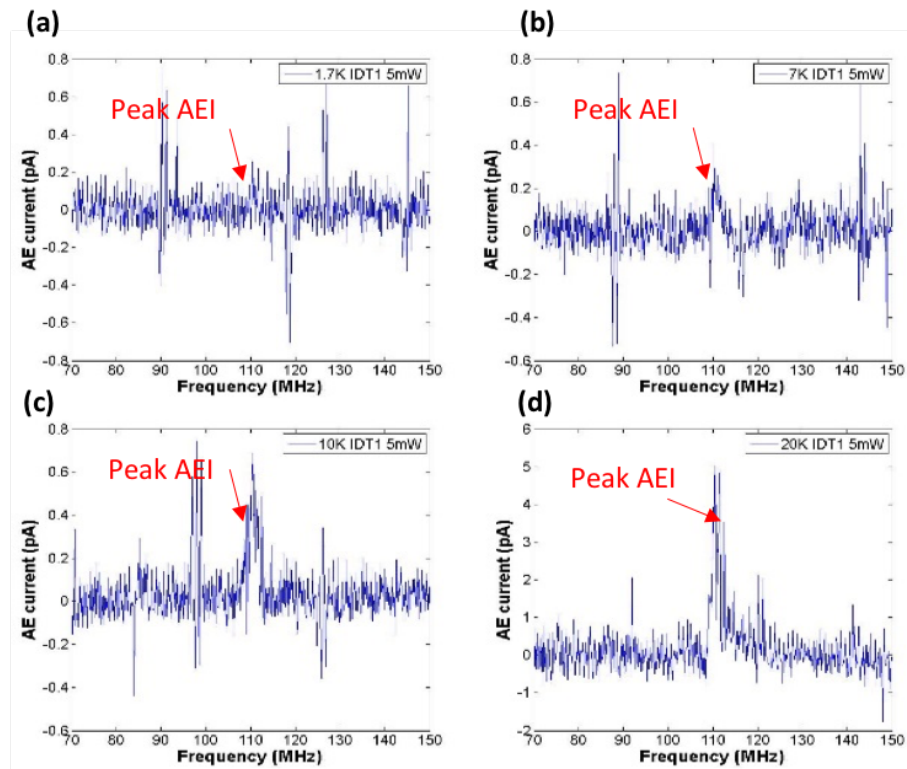
Figure 6.14 AE current excited by IDT1 with 5 mW RF power at temperatures of (a) 1.7 K, (b) 7 K, (c) 10 K, and (d) 20 K.
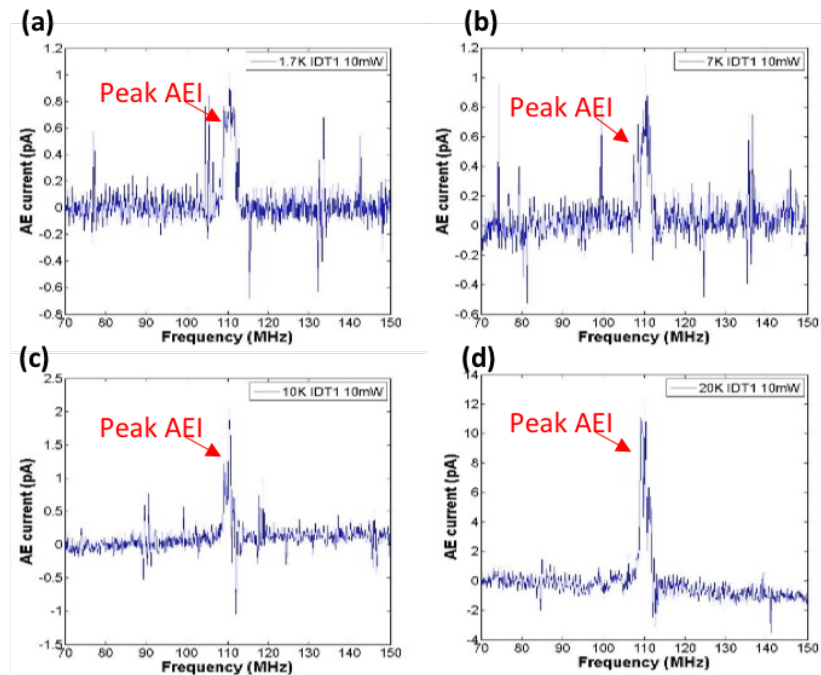
Figure 6.15 AE current excited by IDT1 with 10 mW RF power at temperatures of (a) 1.7 K, (b) 7 K, (c) 10 K, and (d) 20 K.

It can be seen from the Fig. 6.14 that AE current was undetectable when excited by 5 mW RF power at low temperature, which means that the AE current was possible to pinch off by reducing the temperature. While, the AE current was visible at all temperatures when excited by 10 mW RF power as shown in Fig. 6.15. To clearly illustrate the temperature-dependent AE current pinch off in graphene nanochannel, the peak AE current as a function of SAW power was obtained from these data and plotted in Fig. 6.16. First, taking the AE current obtained at 5 K as an example, when the RF power was smaller than 9.2 mW, the AE current was found to be in the noise level, which means the AE current was pinched off. When the RF power exceeded 9.2 mW, the AEI was found to be proportional to the SAW power. Comparing the figures in Fig. 6.16, we find that the RF power at which the AE current was pinched off was relevant to the temperature. Lower temperature resulted in a higher RF power, and when the temperature was high (50 K and 70 K in this measurement) the relationship of AE current with the SAW power was linear even at minimal RF power.
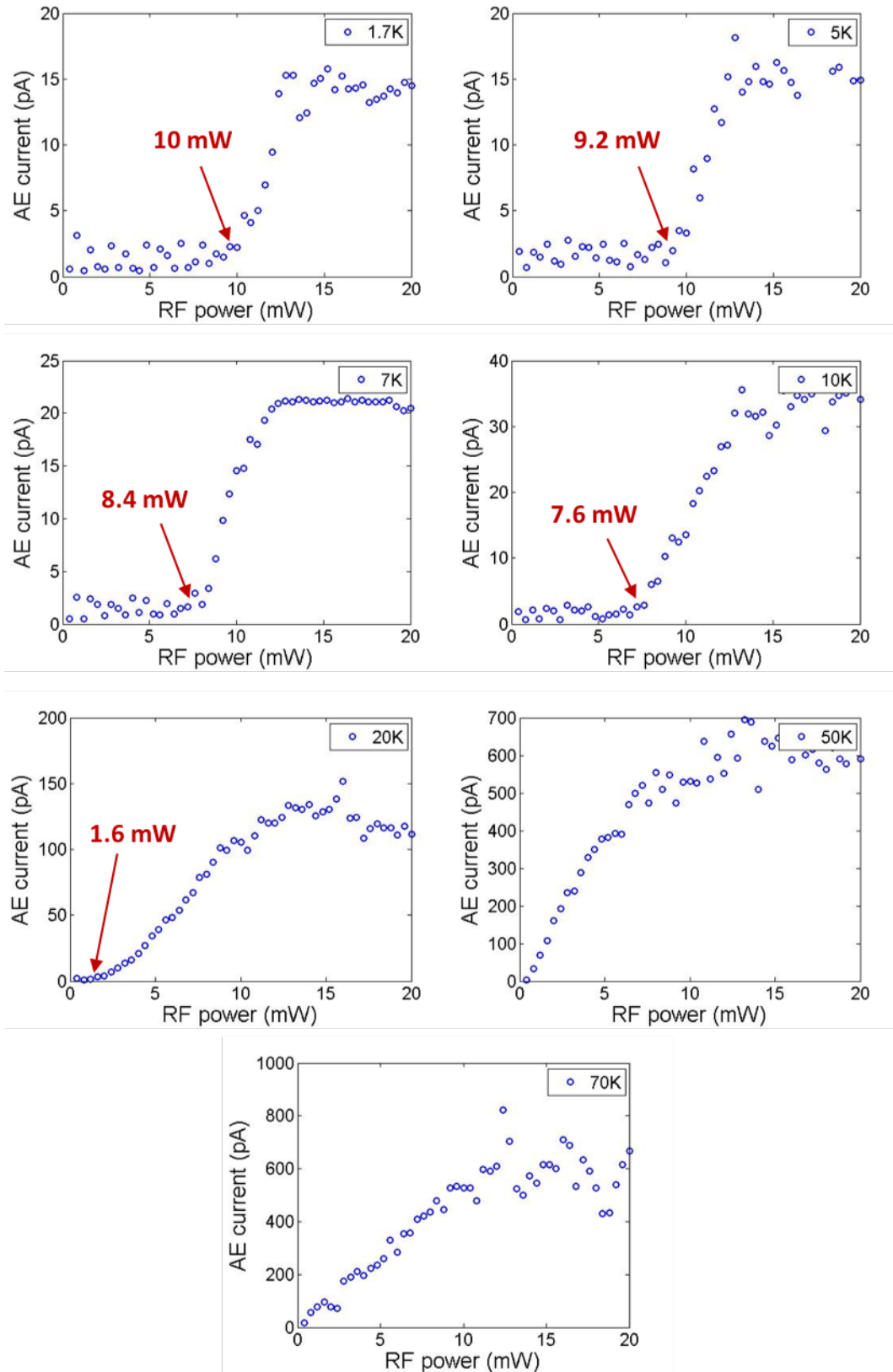
Figure 6.16 Peak AE current as a function of SAW power at different temperatures.

Noticing that channel area of the device was very dirty as shown in Fig. 6.12(a), to better investigate the AE current in graphene nanochannel at low temperature, a device with an improved graphene patterning in the channel with less contamination and flatter edges (Fig. 6.12(b)) was fabricated. On the other hand, noticing that the maximum output of the RF power source for the experiments on Fig. 6.16 was ~13 mW, a low noise amplifier (Mini-Circuits, ZHL-2010+) was used to investigate the AE current across a broader power range. Similar measurements to Fig. 6.16 were made for this device, and some of the data obtained for temperatures lower than 50 K are shown in Fig. 6.17.

In this measurement, the temperature-dependent AE current pinch off in graphene nanochannel was also seen, as shown in Fig. 6.17. In order to illustrate this behavior more clearly, some measurement results with smaller power interval were put together in the same figure (Fig. 6.18). As shown in Fig. 6.18, the acoustic current flow was pinched off for small RF power at low temperature, and only when the RF power was larger than a certain value, the AE current was allowed and increased as the RF power increasing. The RF power at which the current was just pinched off was larger at lower temperature. On the other hand, comparing with Fig. 6.16, a new feature of AE current-RF power curve showed up at around 15 mW – 20 mW range (illustrated by red circle), where the AE current and the RF power was not linear, the explanation of which needs a further investigation and wasn't done in this thesis.
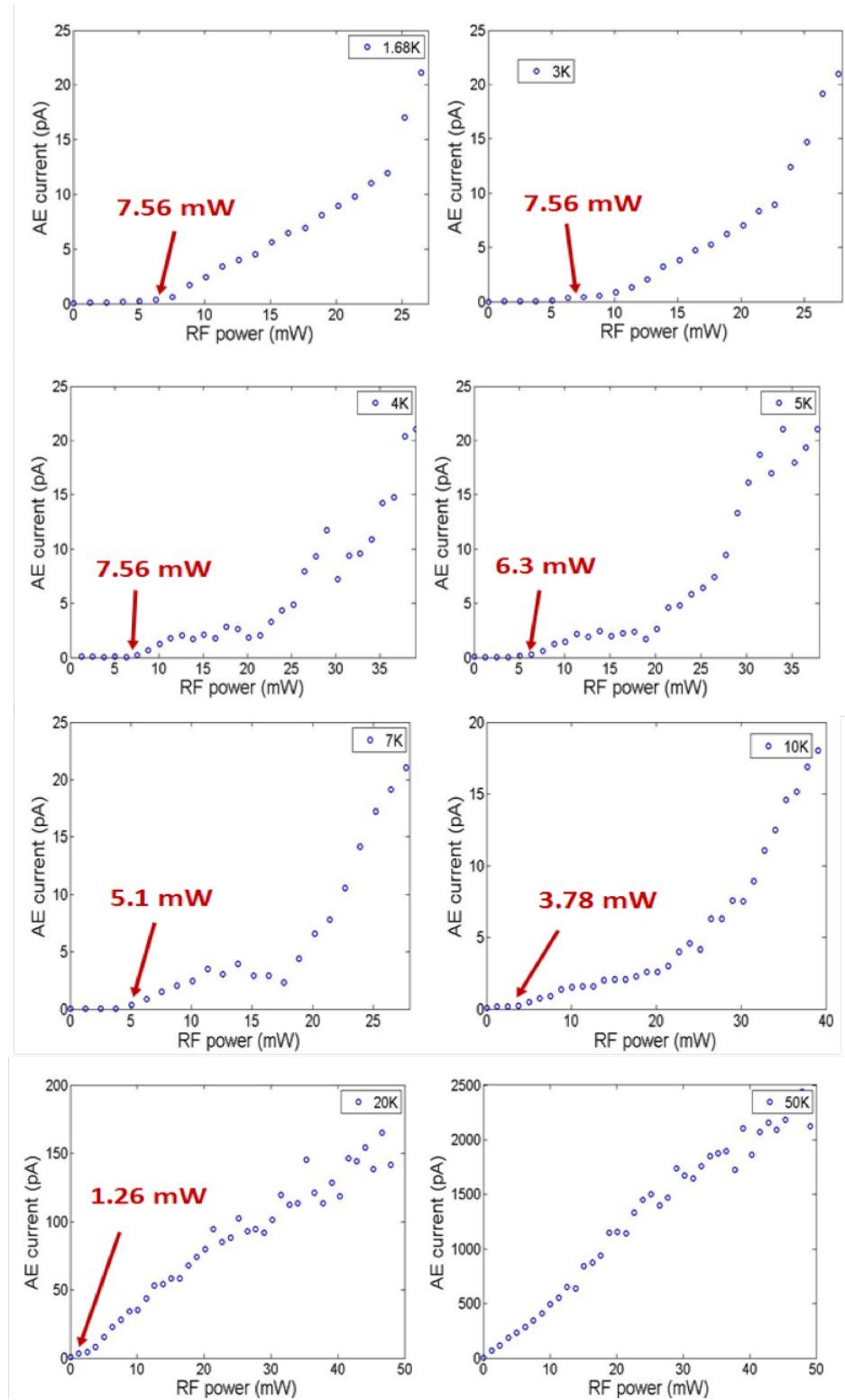
Figure 6.17 Peak AE current as a function of SAW power at different temperatures obtained using an improved graphene AE device.
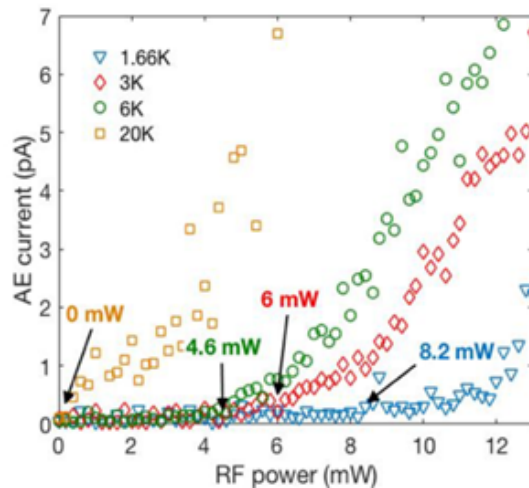
Figure 6.18 Peak AE current as a function of RF power at different temperatures, in which the power values illustrate the power at which the AE current began to be allowed.

It has been reported that boundary condition of graphene sample's edges [237], grain boundary in polycrystalline-structured CVD graphene [241], and impurities and defects [84] could introduce potential barriers in graphene nanoribbons. Additionally, no Klein tunneling would show up for carriers in graphene nanoribbon. In that case, the carrier could only pass through the graphene channel when its energy was larger than the channel barrier, or its tunneling probability decayed exponentially in the channel direction. The carrier's energy comes from thermal energy and SAWs. Only when the sum of potential of SAWs that applied on carriers and the thermal energy was larger than the potential of graphene channel barrier, the carriers could pass through the channel. This model explains the inverse relationship of temperature and "pinch off point". Based on these thought, a model relating graphene channel barriers height, SAW potential and temperature,

as illustrated in Fig. 6.19, was proposed to explain this behavior. In Fig. 6.19, T is the temperature, SAW potential represents the maximum potential of the SAW, the levels of source and drain represent the chemical potential at the input port and output port of the channel, and the channel barrier is the maximum potential through the channel.
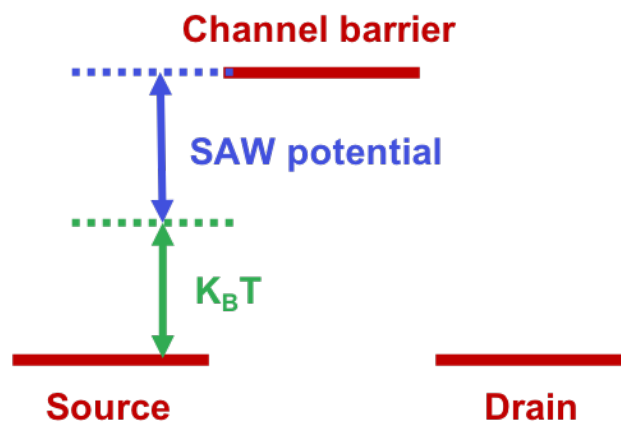
Figure 6.19 A heuristic model for illustrating the condition that SAW could pump the carrier transport through the graphene channel.

According to the relationship $P_{channel\ barrier} = k_B T + P_{SAW}$, illustrated in Fig. 6.19, the potential of the channel barrier should be obtainable by linear fitting since the value of k_B and T were known, and the SAW potential was proportional to RF power, $P_{SAW} = \alpha \cdot P_{RF}$, where α was a fitting coefficient and the RF power has been known. By using the data obtained in Fig. 6.18, the fit to the value of channel barrier was found to be ~1.3 meV (Fig. 6.20).
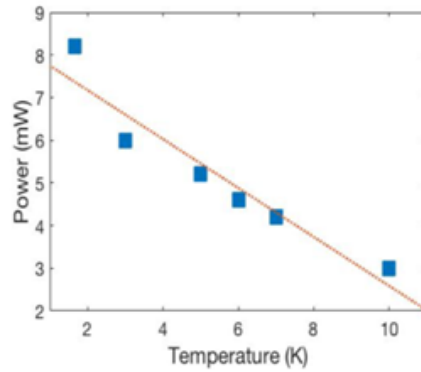
Figure 6.20 Linear fitting the relationship between the temperature and the RF power at which carriers was just pinched off from passing through the graphene channel.
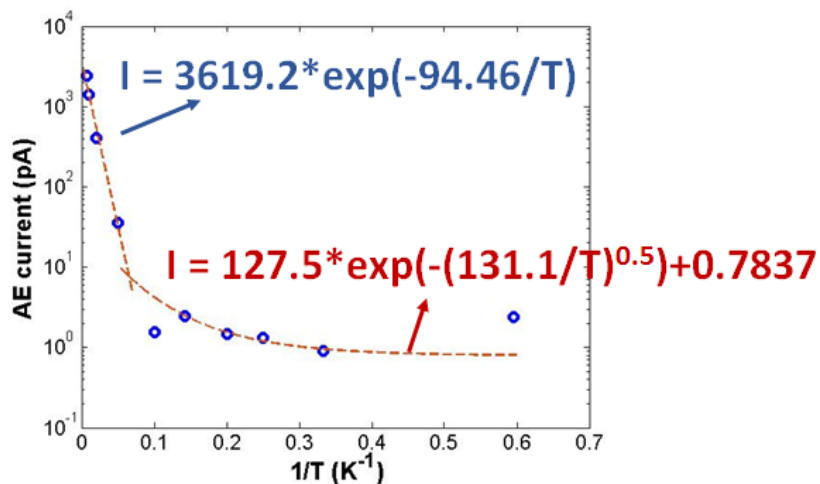
Figure 6.21 AE current with respect to reverse temperature.

The AE current of the device pumped by 10 mW RF power as a function of 1/T was plotted in Fig. 6.21, from which a clear two-segment feature was seen. In the high temperature region, the current-temperature data was fitted by $I = 3619.2 \times exp(-94.46/T)$, while in low temperature region, the current-temperature data followed the relationship: $I = 3619.2 \times exp(-94.46/T)$. The crossover point of these two fitting curves was found to be located at a

temperature around 16 K. The corresponding energy of the temperature was ~1.4 meV, which should be similar to the potential of the channel barrier [237].

The slight difference (~ 7%) of the values obtained by these two methods might be caused by: 1. The thermal energy of carriers should obey a Boltzmann distribution, whereas, by fitting $P_{channel\ barrier} = k_B T + P_{SAW}$, $k_B T$ was used as the thermal energy at T, which introduced the error in the fitting result. 2. The accuracy of the SAW power used for the fitting was limited by the interval of the RF power used for the measurement. 3. The generated AE current was in the noise level when the condition of $P_{channel\ barrier} = k_B T + P_{SAW}$ was just satisfied, making it difficult to get the precise SAW power enabling the carrier transport.

6.4 Electric modulated acoustoelectric current

In order to push towards quantized carrier transport, and by analogy with semiconductor systems, the AE current should be controlled electrically. Gate-voltage modulation of the AE current was therefore investigated.

6.4.1 Device

The device fabricated for this was imaged, as shown in Fig. 6.22(a), with a close-up view of the gated graphene area shown in Fig. 6.22(b). In this device, the wavelength of the IDTs was 16 μm with the space ratio of 1:1, the channel was 18 μm length and 10 μm width, the size of the gate was 12 μm, and the contact area of electrodes and graphene leads surpassed 200 μm^2.

The gate electrode, located in the middle of the two leads electrodes, was isolated from the graphene channel by 100 nm of atomic layer deposition (ALD) grown Al_2O_3. The horseshoe shape dark area in Fig. 6.22(b) was graphene, which was visible under the microscope because of the thin layer of Al_2O_3.

The conductivity of the graphene was modulated using a gate voltage, as shown in Fig. 6.22(c). The graphene channel reached the Dirac point at -7 V, as given by the point of minimum conductivity, indicating n-doping for the graphene before gating. The reason for the n doping was that the reaction, $2H_2O \rightarrow O_2 + 4H^+ + 4e^-(graphene)$, produced during the ALD process was enhanced at high growth temperatures [243]. The doping level of the graphene sample was calculated based on a capacitive model [4], to be $n = C_g V_g/e \approx 4.46 \times 10^{12} cm^{-2}$. One concern is whether the graphene sample could be oxidized during the ALD process. To check this, a device fabricated using the same recipe as the device for measurement was taken for a Raman measurement, after rinsing the device in MF319 solution to remove the Al_2O_3 layer. The measured Raman spectra are shown in Fig. 6.22(d), where clear G peak and 2D peak were seen, indicating a good quality for the single-layer graphene sample, even after the ALD process was undertaken.
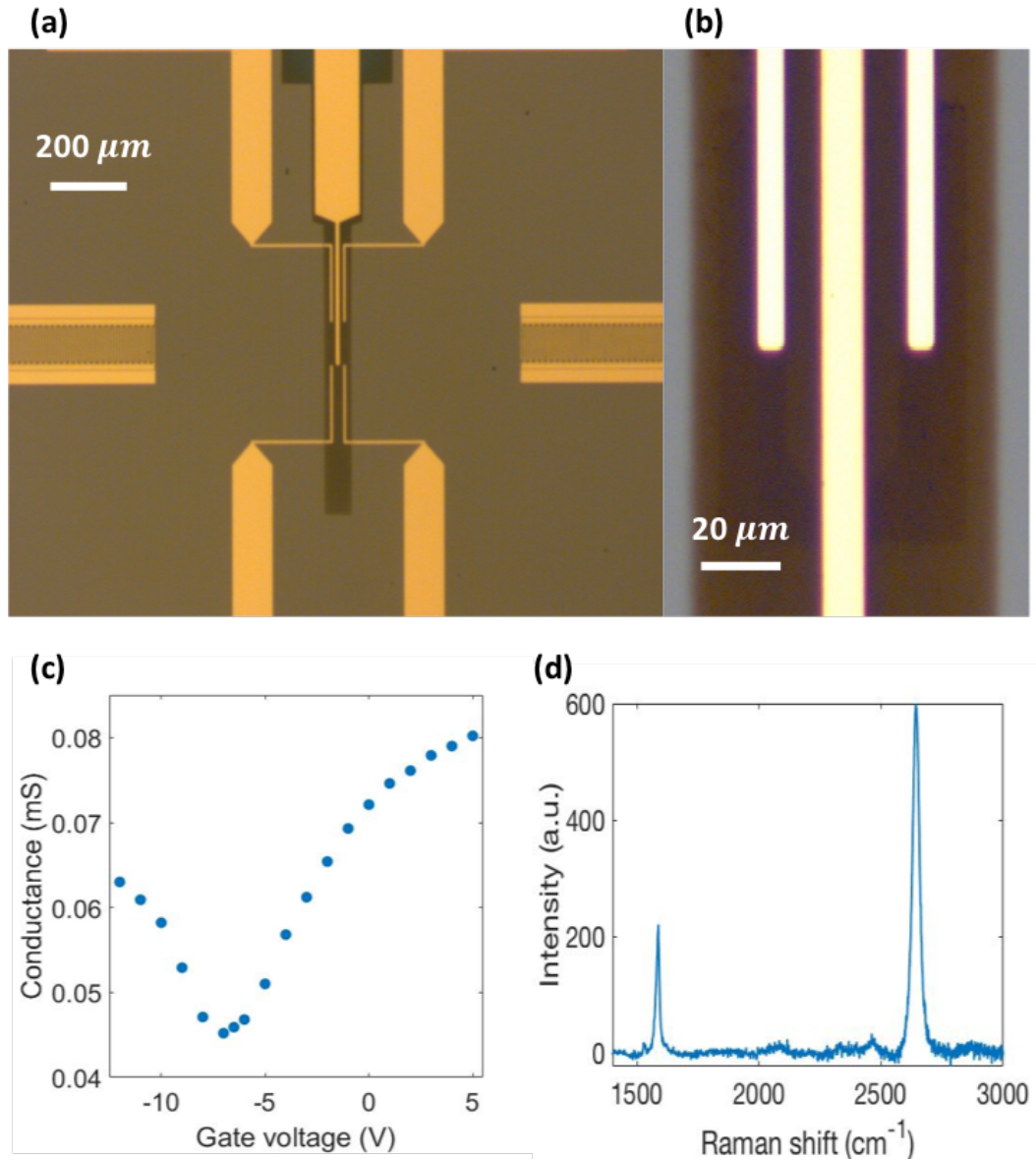
Figure 6.22 (a) Microscopic image of tunable graphene AE device, (b) the close-up view of the gated graphene area of the device, (c) modulation of the graphene's conductivity using gate voltage, (d) Raman spectra of graphene.

6.4.2 Gate modulated AE current

The device was first tested without gate voltage as shown in Fig. 6.23, in which similar resonant frequency of the SAW response (Fig. 6.23(a)) and

the position of peak AE current (Fig. 6.23(b)) confirmed SAW-induced carrier transport. Also, the measurement showed a negative current flow in the direction of the SAW travel, indicating electrons transport in the graphene, which is agree with the n-type doped graphene without gate as illustrated by Fig. 6.22(c).
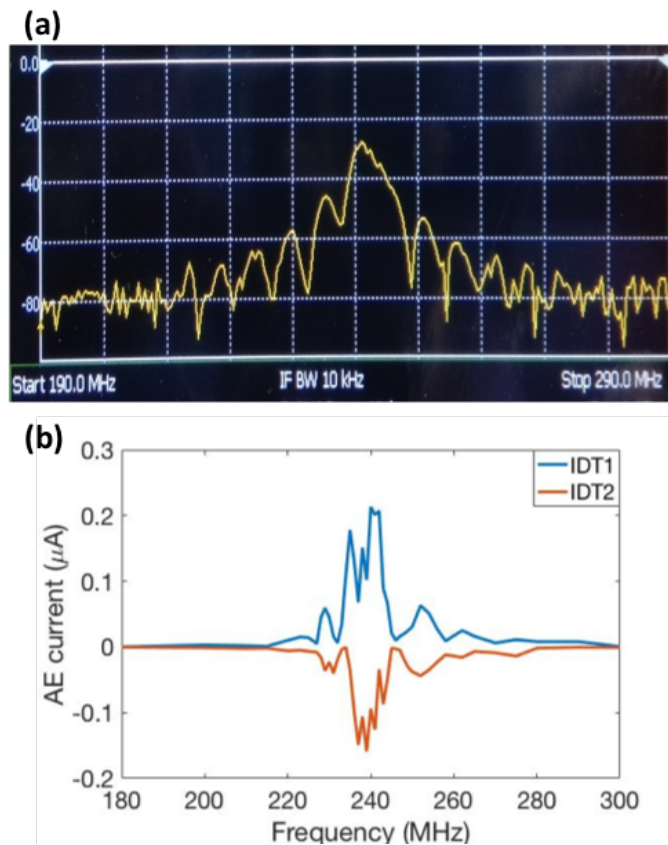
Figure 6.23 (a) Transmission of the SAW delay line, (b) AE current obtained without gate voltage.

The electrically modulated AE currents were then measured at a temperature of 20 K, shown as Fig. 6.24. It can be seen that, when the gate voltage was higher than V_D, the AE currents was always in the negative direction while the amplitude was linear to the SAW power; by contrast, when

the gate voltage was lower than V_D, the AE currents was found to be positive for small SAW powers, and negative at large SAW power.
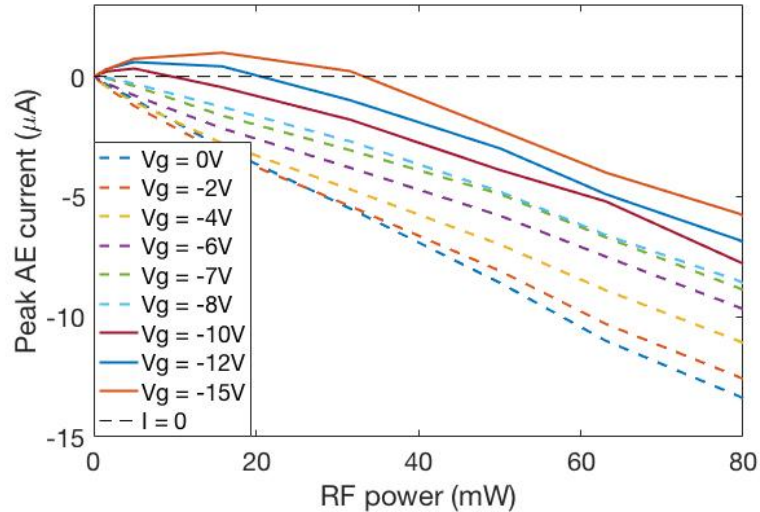
Figure 6.24 AE current obtained at different gate voltage.

The reason for the change of current direction at large SAW power when a gate voltage was lower than V_D is likely to be that, in this gating condition, the graphene channel under the gate electrodes was effectively p-doped, while the graphene area away from the gated region was n-doped. When the SAW potential was smaller than the Fermi level in graphene channel, only positive charge carriers could be transported through the graphene channel. Thus, the current direction found to be the same as the SAW propagating direction. On the other hand, when the SAW potential was larger than the Fermi level in graphene channel, both positive and negative charge carriers could be transported through the channel. In that case, if the SAW potential was large enough that the number of negative carriers trapped in the SAW potential from graphene leads was larger than the

number of positive carriers trapped in the SAW potential from graphene channel, the current direction became opposite to the SAW direction.

Fig. 6.25 gives the AE current as a function of gate voltage. As can be seen from this figure, when the SAW power was small, the current direction could be changed using gate voltage since the Fermi level was easy to surpass SAW potential. When the SAW power was so large that the Fermi level was much smaller than the SAW potential, the current direction was found to be always opposite to the SAW direction since the dominant quantity of carriers then came from the graphene leads, which were negatively doped.
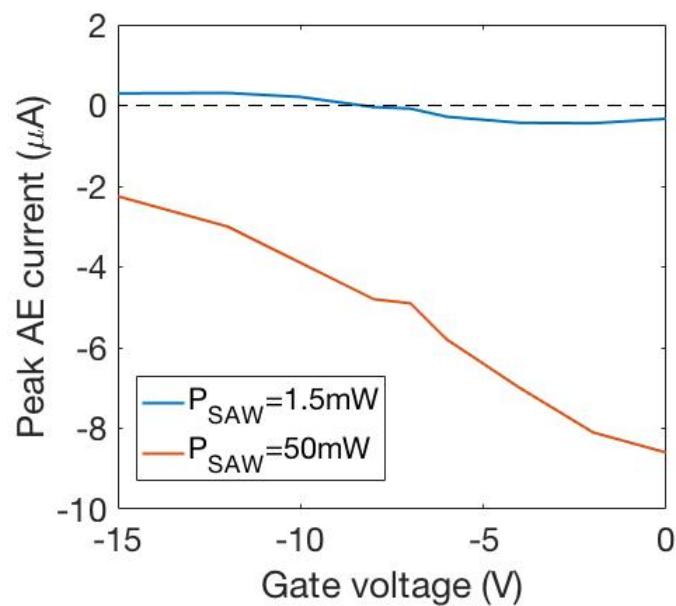
Figure 6.25 AE current as a function of gate voltage, generated by 1.5 mW RF power and 50 mW RF power.

6.5 Conclusion

Graphene AE devices working at GHz frequencies, and operating at low temperatures, and tunable using gate voltage were realized. Pinch-off of the AE current was observed in a graphene nanoribbon at low temperature. The results were shown to agree well with a heuristic model, taking both the effect of temperature and of the potential barrier formed by ther graphene ribbon into consideration. The findings contributed to better understanding the acoustoelectric effect in graphene nanostructure and provided a stepping stone towards graphene-based quantized acoustoelectric current source.

Chapter 7 Conclusion and future work

7.1 Conclusion

This thesis explored the interactions between two-dimensional materials and structures with two kinds of high-frequency signals, namely terahertz electromagnetic waves and MHz to GHz surface acoustic waves. The physical background and key technologies relevant to these works were described in chapter 2 and chapter 3, respectively. Following that, several specific topics aiming for practical applications were explored, and some interesting results are achieved, which are listed as follows:

1. A significant enhancement in the sensitivity of dielectric sensors based on the SRR terahertz metamaterials was produced by the introduction of etched trenches into the LC gap area. Both finite element simulations and THz-TDS experiments were utilized in this research. The introduction of etched trenches reduces the local effective dielectric permittivity of the SRR sensors, which is illustrated by the trenches induced blue shift of resonant frequencies. The enhancement of the dielectric sensitivity is demonstrated by the increase of frequency shift in response to the dielectric material deposited on the surface of the SRRs with thicknesses from 0 to 18 μm. The works showed a sensitivity enhancement by a factor of up to ~2.7 times with etched trenches

formed at a depth of ~3.4 μm, for example. This approach overcomes the limitations of previously reported sensitivity enhancement methods based on the use of lower-index or ultrathin substrates.

2. Free-space THz pulse detections using graphene bowtie photoconductive antenna were realized. The photogenerated carriers in graphene are accelerated by the electric field of THz wave, the signals of which are recorded by a THz-TDS setup. The SNR of the THz signal obtained by the graphene detector is ~130, with a bandwidth of ~2 THz. The linear dependence of the signal intensity on the intensity of the THz wave and the probe beam power was demonstrated.

3. A broadband tunable THz polarizer with a geometry of hybrid graphene-metal strip arrays was proposed, theoretically analyzed and experimentally demonstrated. The designed geometry of the hybrid graphene-metal strip arrays dramatically enhances the modulation depth compared with graphene strips owing to the increase of the effective conductivity of the strips and the enhancement of light-plasmon coupling in graphene. The direction-dependent modulation, the bandwidth, and the modulation enhancement of the polarizer were examined and illustrated with different geometries of devices using THz-TDS. Greater than 7 THz bandwidth and around ~18 times modulation enhancement is obtained experimentally, which agreed with the calculation results. Also, we predict greater than 40 THz bandwidth with a modulation depth of 95% at 0.5 THz, with a maximum of >98% modulation depth could be obtainable according to our calculations, using state-of-the-art fabrication technologies.

4. Graphene AE devices working at GHz frequencies, operating at low temperatures, and tuning by gate voltage were explored. A network analyser was used for supplying RF signal and detecting SAW delay line response, and a Keithley SMU was used for the current measurements. Pinch-off of the AE current was observed for a graphene nanoribbon at low temperature. The feature of temperature-dependent AE current in graphene nanoribbon agrees well with a heuristic model relevant to the carrier localization in graphene ribbon, taking both the effect of temperature and the potential barrier formed by the graphene ribbon into consideration. This model can be used to estimate the potential in the graphene ribbon, which was around 1.4 meV – 1.7 meV for the device in this work.

7.2 Future work

This thesis has created some opportunities for future investigations:

1. The wavelength-independent absorption nature of graphene makes the graphene PC antenna being valid for other kinds of femtosecond lasers, including 1550 nm and 1064 nm fibre lasers. The wavelength-dependent properties of graphene as a THz detector could therefore be investigated.

   Experimental method:

   The geometry of experimental setup used in this thesis could be used for the further investigation by changing the wavelength of the femtosecond lasers. One optional method is to replace the existing femtosecond laser by a

new one with different wavelength (1064 nm fibre lasers, for example). Another optional method is to use frequency doubling crystal (BBO for example) to change the frequency of femtosecond laser.

Data analysis method:

The properties of graphene could also be investigated. The detected terahertz pulse, Edetect, by using photoconductive antenna is the convolution of the induced terahertz pulse, E0, the response function of antenna, Rantenna, and the response properties of the photoconductive material, Rmaterial, in the time domain, which can be written as

$$E_{detect} \propto J_{detect} = E_0 \otimes R_{antenna} \otimes R_{material} \qquad 7.1$$

Since in THz-TDS the detected current is used to represent the field of terahertz pulse and the only difference between the current and the THz field is a constant coefficient, detected signal J_{detect} can be used for analysis. $R_{antenna}$ could be obtained by simulation using CST for example. E0 could be obtained using a detector with the same geometry as graphene bowtie, but LT-GaAs as photoconductive material whose properties have been well known. Obtaining all these values, the properties of the graphene acting as photoconductive material for coherent terahertz detection could be analysed using equation 7.1.

Theoretical consideration:

In order to understand the dynamic properties of the evolution of carrier density in graphene, the physical processes of the photoexcited carriers

should be considered. When an electron is excited from the valence band to the conduction band, the acquired energy of electrons is $E_{photon}/2$. If this value is much larger than the chemical potential of graphene sample, several mechanisms would be responsible for the dynamics of carrier density: carrier-carrier scattering (Auger processes) and carrier-phonon scattering (electron-hole recombination), both of which need to be considered for understanding the behaviors of carriers in graphene.

The Auger processes are quite different between n-doped graphene and p-doped graphene, as illustrated in Fig. 7.1. Works have been shown that in p-doped graphene carrier multiplication is expected, which should be taken into account for analysing the efficiency of graphene detector.
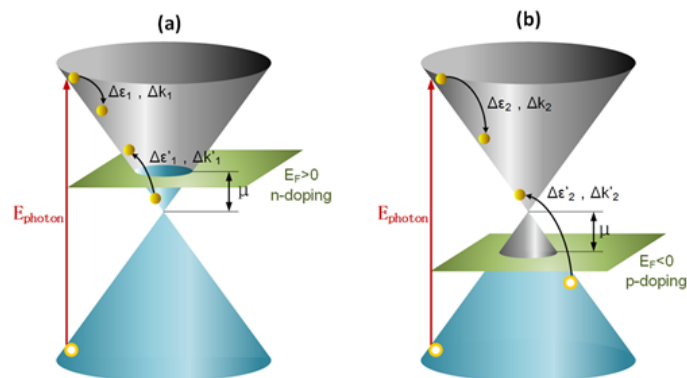
Figure 7.1 Intra-band Auger process and inter-band Auger process in graphene with different doping properties.

2. Three main achievements were obtained for graphene AE devices, which are extensions to GHz frequencies, AE current pinch-off at low temperatures, and tuning by gate voltage. A further potentially promising line of research would be to attempt observation of a quantized

acoustoelectric current in graphene, in which SAW frequency would then be locked to the carrier transport.

Improvements being needed in fabrication:

The GHz SAW delay line fabricated in this thesis is good enough for quantised AE device. While, it could be improved by enlarging the aperture of the IDTs and making the distance between IDT and graphene channel shorter to increase the efficiency of the device.
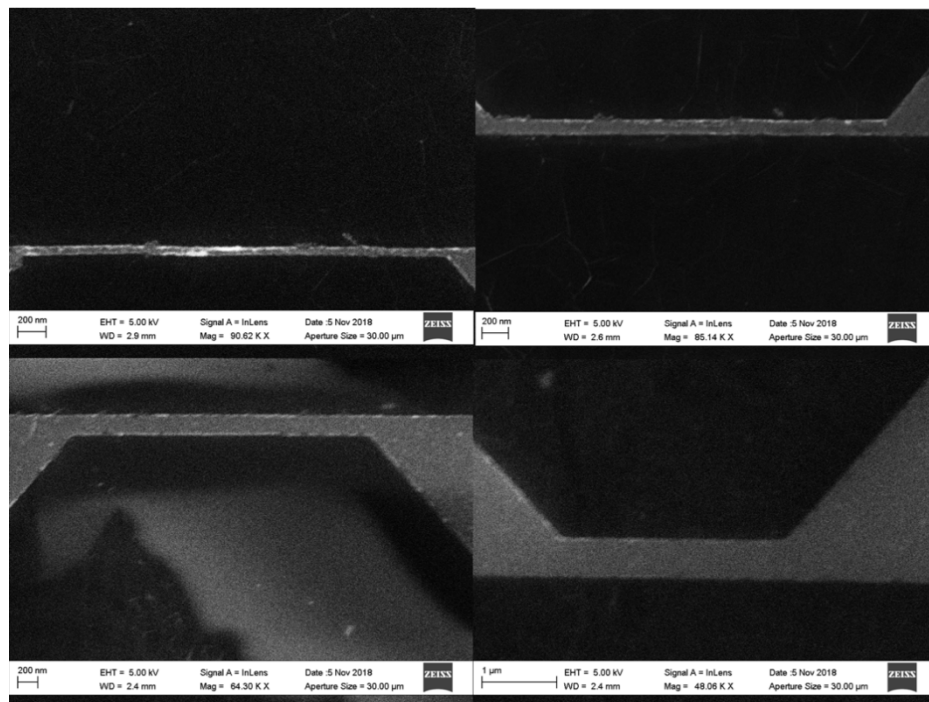
Figure 7.2 SEM images of graphene channel with the width of 50 nm, 100 nm, 200 nm, and 500 nm, respectively.

A graphene channel with larger barrier potential could help to reduce the difficulties of measurements. The larger barrier can be obtained by reducing the width of graphene channel. I have done some researches on this with Dr.

Mark Rosamond, and 50 nm wide graphene has been realized, as shown in Fig. 7.2.

100 nm Al_2O_3 has been proved its good performance for gating the AE current at gate voltage lower than 20 V. While further investigations are needed to better control the leakage / shorting currents. Possible methods would be using thicker Al_2O_3 layer, or CVD grown SiO_2 or Si_3N_4 layers as dielectric materials.

Bibliography

[1] A. K. Geim and K. S. Novoselov, "The rise of graphene," *Nature Materials,* vol. 6, pp. 183-191, 2007.

[2] M. Lapine, I. V. Shadrivov and Y. S. Kivshar, "Colloquium: Nonlinear metamaterials," *REVIEWS OF MODERN PHYSICS,* vol. 86, no. 3, pp. 1093-1123, 2014.

[3] K. S. Novoselov, A. K. Geim, S. V. Morozov, D. Jiang, Y. Zhang, S. V. Dubonos, I. V. Grigorieva and A. A. Firsov, "Electric field effect in atomically thin carbon films," *Science,* vol. 306, no. 5696, pp. 666-669, 2004.

[4] K. S. Novoselov, A. K. Geim, S. V. Morozov, D. Jiang, M. I. Katsnelson, I. V. Grigorieva, S. V. Dubonos and A. A. Firsov, "Two-dimensional gas of massless Dirac fermions in graphene," *nature,* vol. 438, pp. 197-200, 2005.

[5] A. H. C. Neto, F. Guinea, N. M. R. Peres, K. S. Novoselov and A. K. Geim, "The electronic properties of graphene," *REVIEWS OF MODERN PHYSICS,* vol. 81, no. 1, pp. 109-162, 2009.

[6] F. Bonaccorso, Z. Sun, T. Hasan and A. C. Ferrari, "Graphene photonics and optoelectronics," *NATURE PHOTONICS,* vol. 4, pp. 611-622, 2010.

[7] R. Murali, Y. Yang, K. Brenner, T. Beck and J. D. Meindl, "Breakdown current density of graphene nanoribbons," *APPLIED PHYSICS LETTERS,* vol. 94, no. 243114, pp. 1-3, 2009.

[8] K. S. Novoselov, V. I. Fal'ko, L. Colombo, P. R. Gellert, M. G. Schwab and K. Kim, "A roadmap for graphene," *NATURE,* vol. 490, no. 7419, pp. 192-200, 2012.

[9] P. E. Allain and J.-N. Fuchs, "Klein tunneling in graphene: optics with massless electrons," *Eur. Phys. J. B,* vol. 83, no. 301, 2011.

[10] M. Gmitra, S. Konschuh, C. Ertler, C. Ambrosch-Draxl and J. Fabian, "Band-structure topologies of graphene: Spin-orbit coupling effects from first principles," *PHYSICAL REVIEW B,* vol. 80, no. 235431, pp. 1-5, 2009.

[11] J. H. Warner, F. Schaffel, A. Bachmatiuk and M. H. Rummeli, Graphene: Fundamentals and Emergent Applications, Elsevier Inc., 2013.

[12] S. D. Sarma, S. Adam , E. H. Hwang and E. Rossi, "Electronic transport in two-dimensional graphene," *REVIEWS OF MODERN PHYSICS,* vol. 83, no. 2, pp. 407-470, 2011.

[13] S. S. SHAMS, R. ZHANG and J. ZHU, "Graphene synthesis: a Review," *Materials Science-Poland,* vol. 33, no. 3, pp. 566-578, 2015.

[14] M. S. A. Bhuyan, M. N. Uddin, M. M. Islam, F. A. Bipasha and S. S. Hossain, "Synthesis of graphene," *Int Nano Lett,* vol. 6, pp. 65-83, 2016.

[15] N. Behabtu, J. R. Lomeda, M. J. Green, A. L. Higginbotham, A. Sinitskii, D. V. Kosynkin, D. Tsentalovich, A. N. G. Parra-Vasquez, J. Schmidt, E. Kesselman, Y. Cohen, Y. Talmon and J. M. Tour, "Spontaneous high-concentration dispersions and liquid crystals of graphene," *NATURE NANOTECHNOLOGY,* vol. 5, pp. 406-411, 2010.

[16] N. Liu, F. Luo, H. Wu, Y. Liu, C. Zhang and J. Chen, "One-Step Ionic-Liquid-Assisted Electrochemical Synthesis ofIonic-Liquid-Functionalized Graphene SheetsDirectly from Graphite," *Adv. Funct. Mater.,* vol. 18, pp. 1518-1525, 2008.

[17] X. Li, W. Cai, J. An, S. Kim, J. Nah, D. Yang, R. Piner, A. Velamakanni, I. Jung, E. Tutuc, S. K. Banerjee, L. Colombo and R. S. Ruoff, "Large-Area Synthesis of High-Quality and Uniform Graphene Films on Copper Foils," *Science,* vol. 324, no. 5932, pp. 1312-1314, 2009.

[18] E. Rollings, G.-H. Gweon, S. Y. Zhou, B. S. Mun, J. L. McChesney, B. S. Hussain, A. V. Fedorov, P. N. First, W. A. de Heer and A. Lanzara, "Synthesis and characterization of atomically thin graphite films on a silicon carbide substrate," *Journal of Physics and Chemistry of Solids,* vol. 67, pp. 2172-2177, 2006.

[19] S. Bae, H. Kim, Y. Lee, X. Xu, J.-S. Park, Y. Zheng, J. Balakrishnan, T. Lei, H. R. Kim, Y. I. Song, Y.-J. Kim, K. S. Kim, B. Ozyilmaz, J.-H. Ahn, B. H. Hong and S. Iijima, "Roll-to-roll production of 30-inch graphene films for transparent electrodes," *NATURE NANOTECHNOLOGY,* vol. 5, pp. 574-578, 2010.

[20] S.-a. Peng, Z. Jin, P. Ma, D.-y. Zhang, J.-y. Shi, X.-y. Wang, S.-q. Wang, M. Li, X.-y. Liu and G.-h. Yu, "Effect of source-gate spacing on direct current and radio frequency characteristic of graphene field effect transistor," *APPLIED PHYSICS LETTERS,* vol. 106, no. 033503, pp. 1-4, 2015.

[21] L. Liao, J. Bai, R. Cheng, Y. Lin, S. Jiang, Y. Qu, Y. Huang and X. Duan, "Sub-100 nm Channel Length Graphene Transistors," *Nano Lett.,* vol. 10, no. 10, pp. 3952-3956, 2010.

[22] C. Yu, Z. He, X. Song, Q. Liu, L. Gao, B. Yao, T. Han, X. Gao, Y. Lv, Z. Feng and S. Cai, "High-Frequency Flexible Graphene Field-EffectTransistors with Short Gate Length of 50 nmand Record Extrinsic Cut-Off Frequency," *Phys. Status Solidi RRL,* vol. 12, no. 1700435, pp. 1-4, 2018.

[23] Y. Wu, Y.-m. Lin, A. A. Bol, K. A. Jenkins, F. Xia, D. B. Farmer, Y. Zhu and P. Avouris, "High-frequency, scaled graphene transistors on diamond-like carbon," *NATURE,* vol. 472, pp. 74-78, 2011.

[24] T. Ihn, J. Güttinger, F. Molitor, S. Schnez, E. Schurtenberger, A. Jacobsen, S. Hellmüller, T. Frey, S. Dröscher, C. Stampfer and K. Ensslin, "Graphene single-electron transistors," *materials today,* vol. 13, no. 3, pp. 44-50, 2010.

[25] J. M. Dawlaty, S. Shivaraman, J. Strait, P. George, M. Chandrashekhar, F. Rana, M. G. Spencer, D. Veksler and Y. Chen, "Measurement of the optical absorption spectra of epitaxial graphene from terahertz to visible," *APPLIED PHYSICS LETTERS,* vol. 93, no. 131905, pp. 1-3, 2008.

[26] K. F. Mak, M. Y. Sfeir, Y. Wu, C. H. Lui, J. A. Misewich and T. F. Heinz, "Measurement of the Optical Conductivity of Graphene," *PHYSICAL REVIEW LETTERS,* vol. 101, no. 196405, pp. 1-4, 2008.

[27] T. Low and P. Avouris, "Graphene Plasmonics for Terahertz to Mid-Infrared Applications," *ACS Nano,* vol. 8, no. 2, pp. 1086-1101, 2014.

[28] N. Hunter, A. S. Mayorov, C. D. Wood, C. Russell, L. Li, E. H. Linfield, A. G.

Davies and J. E. Cunningham, "On-Chip Picosecond Pulse Detection and Generation Using Graphene Photoconductive Switches," *Nano Lett.,* vol. 15, pp. 1591-1596, 2015.

[29] D. A. Bandurin, D. Svintsov, I. Gayduchenko, S. G. Xu, A. Principi, M. Moskotin, I. Tretyakov, D. Yagodkin, S. Zhukov, T. Taniguchi, K. Watanabe, I. V. Grigorieva, M. Polini and G. Goltsman, "Resonant terahertz detection using graphene plasmons," *NATURE COMMUNICATIONS,* vol. 9, no. 5392, pp. 1-8, 2018.

[30] Z. Xu, D. Wu, Y. Liu, C. Liu, Z. Yu, L. Yu and H. Ye, "Design of a Tunable Ultra-Broadband Terahertz Absorber Based on Multiple Layers of Graphene Ribbons," *Nanoscale Research Letters,* vol. 13, no. 143, pp. 1-8, 2018.

[31] Z. Chen, X. Chen, L. Tao, K. Chen, M. Long, X. Liu, K. Yan, R. I. Stantchev, E. Pickwell-MacPherson and J.-B. Xu, "Graphene controlled Brewster angle device for ultra broadband terahertz modulation," *NATURE COMMUNICATIONS,* vol. 9, no. 4909, pp. 1-7, 2018.

[32] W. J. Padilla, D. N. Basov and D. R. Smith, "Negative refractive index metamaterials," *materials today,* vol. 9, pp. 28-35, 2006.

[33] C. R. Simovski, "Material Parameters of Metamaterials (a Review)," *OPTICS AND SPECTROSCOPY,* vol. 107, no. 5, pp. 726-753, 2009.

[34] H.-H. Hsiao, C. H. Chu and D. P. Tsai, "Fundamentals and Applications of Metasurfaces," *Small Methods,* vol. 1, no. 1600064, pp. 1-20, 2017.

[35] H.-T. Chen, A. J. Taylor and N. Yu, "A review of metasurfaces: physics and applications," *Rep. Prog. Phys.,* vol. 79, no. 076401, 2016.

[36] J. B. Pendry, "Negative Refraction Makes a Perfect Lens," *PHYSICAL REVIEW LETTERS,* vol. 85, no. 18, pp. 3966-3969, 2000.

[37] A. Grbic and G. V. Eleftheriades, "Overcoming the Diffraction Limit with a Planar Left-Handed Transmission-Line Lens," *PHYSICAL REVIEW LETTERS,* vol. 92, no. 117403, pp. 1-4, 2004.

[38] W. Withayachumnankul, H. Lin, K. Serita, C. M. Shah, S. Sriram, M. Bhaskaran, M. Tonouchi, C. Fumeaux and D. Abbott, "Sub-diffraction thin-film sensing with planar terahertz metamaterials," *OPTICS EXPRESS,* vol. 20, no. 3, pp. 3345-3352, 2012.

[39] N. Yu, F. Aieta, P. Genevet, M. A. Kats, Z. Gaburro and F. Capasso, "A broadband, background-free quarter-wave plate based on plasmonic metasurfaces," *Nano Lett.,* vol. 12, no. 12, pp. 6328-6333, 2012.

[40] N. K. Emani, A. V. Kildishev, V. M. Shalaev and A. Boltasseva, "Graphene: A Dynamic Platform for Electrical Control of Plasmonic Resonance," *Nanophotonics,* vol. 4, pp. 214-223, 2015.

[41] T.-T. Kim, H. Kim, M. Kenney, H. S. Park, H.-D. Kim, B. Min and S. Zhang, "Amplitude Modulation of Anomalously Refracted Terahertz Waves with Gated-Graphene Metasurfaces," *Adv. Optical Mater.,* vol. 6, no. 1700507, pp. 1-7, 2018.

[42] Y. Li, H. Yu, X. Qiu, T. Dai, J. Jiang, G. Wang, Q. Zhang, Y. Qin, J. Yang and X. Jiang, "Graphene-based nonvolatile terahertz switch with asymmetric

electrodes," *Scientific Reports,* vol. 8, no. 1562, pp. 1-9, 2018.

[43]   L. Xia, Y. Wang, G. Wang, X. Long, S. Huang, Y. Tan, W. Yan, S. Dang, S. Yin and H. Cui, "Graphene based terahertz amplitude modulation with metallic tortuous ring enhancement," *Optics Communications,* vol. 440, pp. 190-193, 2019.

[44]   S. H. Lee, M. Choi, T.-T. Kim, S. Lee, M. Liu, X. Yin, H. K. Choi, S. S. Lee, C.-G. Choi, S.-Y. Choi, X. Zhang and B. Min, "Switching teraherz waves with gate-controlled active graphene metamaterials," *Nature Materials,* vol. 11, pp. 936-941, 2012.

[45]   S. J. Kindness, N. W. Almond, B. Wei, R. Wallis, W. Michailow, V. S. Kamboj, P. Braeuninger-Weimer, S. Hofmann, H. E. Beere, D. A. Ritchie and R. Degl'Innocenti, "Active Control of Electromagnetically Induced Transparency in a Terahertz Metamaterial Array with Graphene for Continuous Resonance Frequency Tuning," *Adv. Optical Mater.,* vol. 1800570, pp. 1-8, 2018.

[46]   L. Deng, Y. Wu, C. Zhang, W. Hong, B. Peng, J. Zhu and S. Li, "Manipulating of Different-Polarized Reflected Waves with Graphene- based Plasmonic Metasurfaces in Terahertz Regime," *Scientific Reports,* vol. 7, no. 10558, pp. 1-10, 2017.

[47]   L. Ju, B. Geng, J. Horng, C. Girit, M. Martin, Z. Hao, H. A. Bechtel, X. Liang, A. Zettl, Y. R. Shen and F. Wang, "Graphene plasmonics for tunable terahertz metamaterials," *NATURE NANOTECHNOLOGY,* vol. 6, pp. 630-634, 2011.

[48]   M. M. Jadidi, A. B. Sushkov, R. L. Myers-Ward, A. K. Boyd, K. M. Daniels, D. K. Gaskill, M. S. Fuhrer, H. D. Drew and T. E. Murphy, "Tunable Terahertz Hybrid Metal–Graphene Plasmons," *Nano Lett.,* vol. 15, pp. 7099-7104, 2015.

[49]   P. R. Wallace, "The Band Theory of Graphite," *PHYSICAL REVIEW,* vol. 71, no. 9, pp. 622-634, 1947.

[50]   K. Nakada and M. Fujita, "Edge state in graphene ribbons Nanometer size effect and edge shape dependence," *PHYSICAL REVIEW B,* vol. 54, no. 24, pp. 17954-17961, 1996.

[51]   V. Barone, O. Hod and G. E. Scuseria, "Electronic Structure and Stability of Semiconducting Graphene Nanoribbons," *NANO LETTERS,* vol. 6, no. 12, pp. 2748-2754, 2006.

[52]   F. Sols, F. Guinea and A. H. C. Neto, "Coulomb Blockade in Graphene Nanoribbons," *PHYSICAL REVIEW LETTERS,* vol. 99, no. 166803, pp. 1-4, 2007.

[53]   C. Stampfer, J. Guttinger, S. Hellmuller, F. Molitor, K. Ensslin and T. Ihn, "Energy Gaps in Etched Graphene Nanoribbons," *PHYSICAL REVIEW LETTERS,* vol. 102, no. 056403, pp. 1-4, 2009.

[54]   A. Celis, M. N. Nair, A. Taleb-Ibrahimi, E. H. Conrad, C. Berger, W. d. Heer and A. Tejeda, "Graphene nanoribbons: fabrication, properties and devices," *J. Phys. D: Appl. Phys.,* vol. 49, no. 143001, 2016.

[55]   M. Y. Han, B. Ozyilmaz, Y. Zhang and P. Kim, "Energy band-gap engineering of graphene nanoribbons," *PHYSICAL REVIEW LETTERS,* vol. 98, no. 206805, pp. 1-4, 2007.

[56]   B. Trauzettel, D. V. Bulaev, D. Loss and G. Burkard, "Spin qubits in graphene

quantum dots," *Nature Physics,* vol. 3, pp. 192-196, 2007.

[57] C. Bena and S. A. Kivelson, "Quasiparticle scattering and local density of states in graphite," *PHYSICAL REVIEW B,* vol. 72, no. 125432, pp. 1-5, 2005.

[58] S. V. Morozov, K. S. Novoselov, M. I. Katsnelson, F. Schedin, D. C. Elias, J. A. Jaszczak and A. K. Geim, "Giant Intrinsic Carrier Mobilities in Graphene and Its Bilayer," *PHYSICAL REVIEW LETTERS,* vol. 100, no. 016602, pp. 1-4, 2008.

[59] J.-H. CHEN, C. JANG, S. XIAO, M. ISHIGAMI and M. S. FUHRER, "Intrinsic and extrinsic performance limits of graphene devices on SiO2," *nature nanotechnology,* vol. 3, pp. 206-209, 2008.

[60] K. I. Bolotin, K. J. Sikes, Z. Jiang, M. Klima, G. Fudenberg, J. Hone, P. Kim and H. L. Stormer, "Ultrahigh electron mobility in suspended graphene," *Solid State Communications,* vol. 146, pp. 351-355, 2008.

[61] C. R. Dean, A. F. Young, I. Meric, C. Lee, L. Wang, S. Sorgenfrei, K. Watanabe, T. Taniguchi, P. Kim, K. L. Shepard and J. Hone, "Boron nitride substrates for high-quality graphene electronics," *Nature Nanotechnology,* vol. 5, pp. 722-726, 2010.

[62] S. Rahimi, L. Tao, S. F. Chowdhury, S. Park, A. Jouvray, S. Buttress, N. Rupesinghe, K. Teo and D. Akinwande, "Toward 300 mm Wafer-Scalable High-Performance Polycrystalline Chemical Vapor Deposited Graphene Transistors," *ACS Nano,* vol. 8, no. 10, pp. 10471-10479, 2014.

[63] J. Baringhaus, M. Ruan, F. Edler, A. Tejeda, M. Sicot, A.-. Ibrahimi, A.-P. Li, Z. Jiang, E. H. Conrad, C. Berger, C. Tegenkamp and W. A. de Heer, "Exceptional ballistic transport in epitaxial graphene nanoribbons," *nature,* vol. 506, pp. 349-354, 2014.

[64] S. Yuan, R. Roldan, H. D. Raedt and M. I. Katsnelson, "Optical conductivity of disordered graphene beyond the Dirac cone approximation," *PHYSICAL REVIEW B,* vol. 84, no. 195418, pp. 1-11, 2011.

[65] R. R. Nair, P. Blake, A. N. Grigorenko, K. S. Novoselov, T. J. Booth, T. Stauber, N. M. R. Peres and A. K. Geim, "Fine Structure Constant Defines Visual Transparency of Graphene," *Science,* vol. 320, no. 5881, p. 1308, 2008.

[66] S. D. Ganichev, D. Weiss and J. Eroms, "Terahertz Electric Field Driven Electric Currents and Ratchet Effects in Graphene," *Ann. Phys.,* vol. 529, no. 1600406, pp. 1-13, 2017.

[67] M. Mittendorff, J. Kamann, J. Eroms, D. Weiss, C. Drexler, S. D. Ganichev, J. Kerbusch, A. Erbe, R. J. Suess, T. E. Murphy, S. Chatterjee, K. Kolata, J. Ohser, J. C. KönigOtto and Schneid, "Universal ultrafast detector for short optical pulses based on graphene," *OPTICS EXPRESS,* vol. 23, no. 22, pp. 28728-28735, 2015.

[68] H. Yan, X. Li, B. Chandra, G. Tulevski, Y. Wu, M. Freitag, W. Zhu, P. Avouris and F. Xia, "Tunable Infrared Plasmonic Devices Using Graphene/Insulator Stacks," *Nature Nanotechnology,* vol. 7, pp. 330-334, 2012.

[69] H. Yan, T. Low, W. Zhu, Y. Wu, M. Freitag, X. Li, F. Guinea, P. Avouris and F. Xia, "Damping Pathways of Mid-Infrared Plasmons in Graphene Nanostructures," *NATURE PHOTONICS,* vol. 7, pp. 394-399, 2013.

[70] N. Yu, P. Genevet, M. A. Kats, F. Aieta, J.-P. Tetienne, F. Capasso and Z. Gaburro, "Light Propagation with Phase Discontinuities: Generalized Laws of Reflection and Refraction," *SCIENCE,* vol. 334, pp. 333-337, 2011.

[71] P. Gay-Balmaz and O. J. F. Martin, "Electromagnetic resonances in individual and coupled split-ring resonators," *JOURNAL OF APPLIED PHYSICS,* vol. 92, no. 5, pp. 2929-2936, 2002.

[72] T. GUO and C. ARGYROPOULOS, "Broadband polarizers based on graphene metasurfaces," *Optics Letters,* vol. 41, no. 23, pp. 5592-5595, 2016.

[73] Y. Fan, N.-H. Shen, F. Zhang, Q. Zhao, Z. Wei, P. Zhang, J. Dong, Q. Fu, H. Li and C. M. Soukoulis, "Photoexcited Graphene Metasurfaces: Significantly Enhanced and Tunable Magnetic Resonances," *ACS Photonics,* vol. 5, no. 4, pp. 1612-1618, 2018.

[74] Z. LIU and B. BAI, "Ultra-thin and high-efficiency graphene metasurface for tunable terahertz wave manipulation," *OPTICS EXPRESS,* vol. 25, no. 8, pp. 8584-8592, 2017.

[75] S.-F. Shi, B. Zeng, H.-L. Han, X. Hong, H.-Z. Tsai, H. S. Jung, A. Zettl, M. F. Crommie and F. Wang, "Optimizing Broadband Terahertz Modulation with Hybrid Graphene/ Metasurface Structures," *Nano Lett.,* vol. 15, pp. 372-377, 2014.

[76] G. Liang, X. Hu, X. Yu, Y. Shen, L. H. Li, A. G. Davies, E. H. Linfield, H. K. Liang, Y. Zhang, S. F. Yu and Q. J. Wang, "Integrated Terahertz Graphene Modulator with 100% Modulation Depth," *ACS Photonics,* vol. 2, no. 11, pp. 1559-1566, 2015.

[77] A. Wixforth, J. Scriba, M. Wassermeier and J. P. Kotthaus, "Surface acoustic waves on GaAs/AlxGa1-xAs heterostructures," *PHYSICAL REVIEW B,* vol. 40, no. 11, pp. 7874-7887, 1989.

[78] A. Wixforth and J. P. Kotthaus, "Quantum Oscillations in the Surface-Acoustic-Wave Attenuation Caused by a Two-Dimensional Electron System," *PHYSICAL REVIEW LETTERS,* vol. 56, no. 19, pp. 2104-2106, 1986.

[79] T. Poole and G. R. Nash, "Acoustoelectric Current in Graphene Nanoribbons," *Scientific Reports,* vol. 7, no. 1767, pp. 1-9, 2017.

[80] L. Bandhu and G. R. Nash, "Controlling the properties of surface acoustic waves using graphene," *Nano Research,* vol. 9, no. 3, pp. 685-691, 2016.

[81] T. Poole and G. R. Nash, "Acoustoelectric photoresponse of graphene nanoribbons," *J. Phys. D: Appl. Phys.,* vol. 51, no. 154001, pp. 1-5, 2018.

[82] V. Miseikis, J. E. Cunningham, K. Saeed, R. O'Rorke and A. G. Davies, "Acoustically induced current flow in graphene," *APPLIED PHYSICS LETTERS,* vol. 100, no. 133105, pp. 1-4, 2012.

[83] L. Bandhu and G. R. Nash, "Temperature dependence of the acoustoelectric current in graphene," *APPLIED PHYSICS LETTERS,* vol. 105, no. 263106, pp. 1-4, 2014.

[84] Q. Li, E. H. Hwang and S. D. Sarma, "Disorder-induced temperature-dependent transport in graphene: puddles, impurities, activation, and diffusion," *PHYSICAL REVIEW B,* vol. 84, no. 115442, pp. 1-16, 2011.

[85] T. Poole, L. Bandhu and G. R. Nash, "Acoustoelectric photoresponse in graphene," *APPLIED PHYSICS LETTERS,* vol. 106, no. 133107, pp. 1-4, 2015.

[86] S. Zheng, H. Zhang, Z. Feng, Y. Yu, R. Zhang, C. Sun, J. Liu, X. Duan, W. Pang and D. Zhang, "Acoustic charge transport induced by the surface acoustic wave in chemical doped graphene," *APPLIED PHYSICS LETTERS,* vol. 109, no. 183110, pp. 1-5, 2016.

[87] B. Davaji, H. D. Cho, M. Malakoutian, J.-K. Lee, G. Panin, T. W. Kang and C. H. Lee, "A patterned single layer graphene resistance temperature sensor," *Scientific Reports,* vol. 7, no. 8811, pp. 1-10, 2017.

[88] E. F. Whitehead, E. M. Chick, L. Bandhu, L. M. Lawton and G. R. Nash, "Gas loading of graphene-quartz surface acoustic wave devices," *APPLIED PHYSICS LETTERS,* vol. 103, no. 063110, pp. 1-4, 2013.

[89] S. Zheng and D. Zhang, "Acoustoelectric Current Response to Gas Molecular Doping in Graphene," in *2016 IEEE SENSORS*, Orlando, FL, USA, 2016.

[90] D. R. Cooper, B. D'Anjou, N. Ghattamaneni, B. Harack, M. Hilke, A. Horth, N. Majlis, M. Massicotte, L. Vandsburger, E. Whiteway and V. Yu, "Experimental Review of Graphene," *ISRN Condensed Matter Physics,* vol. 2012, no. 501686, pp. 1-56, 2012.

[91] A. V. Eletskii, I. M. Iskandarova, A. A. Knizhnik and D. N. Krasikov, "Graphene: fabrication methods and thermophysical properties," *Physics - Uspekhi,* vol. 54, no. 3, pp. 227-258, 2011.

[92] N. Bartelt and K. McCarty, "Graphene growth on metal surfaces," *MRS Bulletin,* vol. 37, no. 12, pp. 1158-1165, 2012.

[93] I. V. Antonova, "Chemical vapor deposition growth of graphene on copper substrates: current trends," *Physics - Uspekhi,* vol. 56, no. 10, pp. 1013-1020, 2013.

[94] A. Ambrosi and M. Pumera, "The CVD graphene transfer procedure introduces metallic impurities which alter the graphene electrochemical properties," *Nanoscale,* vol. 6, pp. 472-476, 2014.

[95] M. T. Ghoneim, C. E. Smith and M. M. Hussain, "Simplistic graphene transfer process and its impact on contact resistance," *APPLIED PHYSICS LETTERS,* vol. 102, no. 183115, pp. 1-4, 2013.

[96] J. W. Suk, A. Kitt, C. W. Magnuson, Y. Hao, S. Ahmed, J. An, A. K. Swan, B. B. Goldberg and R. S. Ruoff, "Transfer of CVD-grown monolayer graphene onto arbitrary substrates," *ACS Nano,* vol. 5, no. 9, pp. 6916-6924, 2011.

[97] J. Kang, D. Shin, S. Bae and B. H. Hong, "Graphene transfer: key for applications," *Nanoscale,* vol. 4, pp. 5527-5537, 2012.

[98] Y. Lee, S. Bae, H. Jang, S. Jang, S.-E. Zhu, S. H. Sim, Y. I. Song, B. H. Hong and J.-H. Ahn, "Wafer-scale synthesis and transfer of graphene films," *Nano Lett.,* vol. 10, pp. 490-493, 2010.

[99] G. B. Barin, Y. Song, I. d. F. Gimenez, A. G. S. Filho, L. S. Barreto and J. Kong, "Optimized graphene transfer: Influence of polymethylmethacrylate (PMMA) layer concentration and baking time on graphene final performance," *CARBON,* vol. 84, pp. 82-90, 2015.

[100] M. Lavin-Lopez, J. Valverde, A. Garrido, L. Sanchez-Silva, P. Martinez and A. Romero-Izquierdo, "Novel etchings to transfer CVD-grown graphene from copper to arbitrary substrates," *Chemical Physics Letters,* vol. 614, pp. 89-94, 2014.

[101] X. Liang, B. A. Sperling, I. Calizo, G. Cheng, C. A. Hacker, Q. Zhang, Y. Obeng, K. Yan, H. Peng, Q. Li, X. Zhu, H. Yuan, A. R. H. Walker, Z. Liu, L.-m. Peng and C. A. Richter, "Toward clean and crackless transfer of graphene," *ACS Nano,* vol. 5, no. 11, pp. 9144-9153, 2011.

[102] A. Pirkle, J. Chan, A. Venugopal, D. Hinojos, C. W. Magnuson, S. McDonnell, L. Colombo, E. M. Vogel, R. S. Ruoff and R. M. Wallace, "The effect of chemical residues on the physical and electrical properties of chemical vapor deposited graphene transferred to SiO2," *APPLIED PHYSICS LETTERS,* vol. 99, no. 122108, pp. 1-3, 2011.

[103] B. H. Son, H. S. Kim, H. Jeong, J.-Y. Park, S. Lee and Y. H. Ahn, "Electron beam induced removal of PMMA layer used for graphene transfer," *Scientific REPORTS,* vol. 7, no. 18058, pp. 1-7, 2017.

[104] L. G. Cançado, A. Reina, J. Kong and M. S. Dresselhaus, "Geometrical approach for the study of G' band in the Raman spectrum of monolayer graphene, bilayer graphene, and bulk graphite," *PHYSICAL REVIEW B,* vol. 77, no. 245408, pp. 1-9, 2008.

[105] C. V. RAMAN and F. R. S., "A new radiation," *Indian J. Phys.,* vol. 2, pp. 387-398, 1928.

[106] A. C. Ferrari, J. C. Meyer, V. Scardaci, C. Casiraghi, M. Lazzeri, F. Mauri, S. Piscanec, D. Jiang, K. S. Novoselov, S. Roth and A. K. Geim, "Raman Spectrum of Graphene and Graphene Layers," *PHYSICAL REVIEW LETTERS,* vol. 97, no. 187401, pp. 1-4, 2006.

[107] Z. Wu and Z. Ni, "Spectroscopic investigation of defects in two-dimensional materials," *Nanophotonics,* vol. 6, no. 6, pp. 1219-1237, 2017.

[108] E. J. Heller, Y. Yang, L. Kocia, W. Chen, S. Fang, M. Borunda and E. Kaxiras, "Theory of Graphene Raman Scattering," *ACS Nano,* vol. 10, pp. 2803-2818, 2016.

[109] M. A. Pimenta, G. Dresselhaus, M. S. Dresselhaus, L. G. Cancado, A. Jorio and R. Saito, "Studying disorder in graphite-based systems by Raman spectroscopy," *Physical Chemistry Chemical Physics,* vol. 9, pp. 1276-1291, 2007.

[110] A. Eckmann, A. Felten, A. Mishchenko, L. Britnell, R. Krupke, K. S. Novoselov and C. Casiraghi, "Probing the Nature of Defects in Graphene by Raman Spectroscopy," *Nano Lett.,* vol. 12, pp. 3925-3930, 2012.

[111] J. Liu, Q. Li, Y. Zou, Q. Qian, Y. Jin, G. Li, K. Jiang and S. Fan, "The Dependence of Graphene Raman D-band on Carrier Density," *Nano Lett.,* vol. 13, pp. 6170-6175, 2013.

[112] J. Neu and C. A. Schmuttenmaer, "Tutorial: An introduction to terahertz time domain spectroscopy (THz-TDS)," *JOURNAL OF APPLIED PHYSICS,* vol. 124, no. 231101, pp. 1-14, 2018.

[113] M. Tani, S. Matsuura, K. Sakai and S.-i. Nakashima, "Emission characteristics of photoconductive antennas based on low-temperature-grown GaAs and semi-insulating GaAs," *APPLIED OPTICS,* vol. 36, no. 30, pp. 7853-7859, 1997.

[114] A. Nahata, A. S. Weling and T. F. Heinz, "A wideband coherent terahertz spectroscopy system using optical rectification and electro-optic sampling," *Appl. Phys. Lett.,* vol. 69, no. 16, pp. 2321-2323, 1996.

[115] I. Babushkin, W. Kuehn, C. Kohler, S. Skupin, L. Berge, K. Reimann, M. Woerner, J. Herrmann and T. Elsaesser, "Ultrafast Spatiotemporal Dynamics of Terahertz Generation by Ionizing Two-Color Femtosecond Pulses in Gases," *PHYSICAL REVIEW LETTERS,* vol. 105, no. 053903, pp. 1-4, 2010.

[116] V. Apostolopoulos and M. E. Barnes, "THz emitters based on the photo-Dember effect," *J. Phys. D: Appl. Phys.,* vol. 47, no. 374002, pp. 1-16, 2014.

[117] M. Hangyo, M. Tani and T. Nagashima, "TERAHERTZ TIME-DOMAIN SPECTROSCOPY OF SOLIDS: A REVIEW," *International Journal of Infrared and Millimeter Waves,* vol. 26, no. 12, pp. 1661-1690, 2005.

[118] L. Rayleigh, D. C. L. and F. R. S., "On Waves Propagated along the Plane Surface of an Elastic Solid," *Proceedings of the London Mathematical Society,* Vols. s1-17, no. 1, pp. 4-11, 1885.

[119] R. M. White and F. W. Voltmer, "Direct Piezoelectric Coupling to Surface Elastic Waves," *APPLIED PHYSICS LETTERS,* vol. 7, no. 12, pp. 314-316, 1965.

[120] N.-F. WANG, I.-T. TANG, C.-I. HUNG and M.-P. HOUNG, "Investigation of Novel Microwave Surface-Acoustic-Wave Filter on Different Piezoelectric Substrates," *Japanese Journal of Applied Physics,* vol. 43, no. 12, pp. 8139-8145, 2004.

[121] S. Kumar, P. Sharma and K. Sreenivas, "Low-intensity ultraviolet light detector using a surface acoustic wave oscillator based on ZnO/LiNbO3 bilayer structure," *Semicond. Sci. Technol.,* vol. 20, no. 8, pp. L27-L30, 2005.

[122] T. Shiba, J. Yamada and A. Yuhara, "Transformer ratio and capacitance in general form for equivalent circuit of SAW IDTs," in *IEEE,* Orlando, FL, USA, USA, 1991.

[123] A. S. Mayorov, N. Hunter, W. Muchenje, C. D. Wood, M. Rosamond, E. H. Linfield, A. G. Davies and J. E. Cunningham, "Surface acoustic wave generation and detection using graphene interdigitated transducers on lithium niobate," *APPLIED PHYSICS LETTERS,* vol. 104, no. 083509, pp. 1-4, 2014.

[124] M. R. T. Tan and C. A. Flory, "Minmization of diffraction effects in SAW devices using a wide aperture," in *IEEE 1986 Ultrasonics Symposium,* Williamsburg, VA, USA, 1986.

[125] D. S. Ballantin , S. J. Martin, A. J. Ricco, G. C. Fry, H. Wohltje, R. M. Whit and E. T. Zellers, Acoustic Wave Sensors: Theory, Design and Physico-Chemical Applications, Academic Press, 1997.

[126] S. J. Park, J. T. Hong, S. J. Choi, H. S. Kim, W. K. Park, S. T. Han, J. Y. Park, S. Lee, D. S. Kim and Y. H. Ahn, "Detection of microorganisms using terahertz metamaterials," *Scientific REPORTS,* vol. 4, no. 4988, pp. 1-7, 2014.

[127] H. Tao, C. Bingham, A. Strikwerda, D. Pilon, D. Shrekenhamer, N. Landy, K.

Fan, X. Zhang, W. Padilla and R. Averitt, "Highly flexible wide angle of incidence terahertz metamaterial absorber: Design, fabrication, and characterization," *PHYSICAL REVIEW B,* vol. 78, no. 241103, pp. 1-4, 2008.

[128] H. Tao, A. Strikwerda, K. Fan, C. Bingham, W. Padilla, X. Zhang and R. Averitt, "Terahertz metamaterials on free-standing highly-flexible polyimide substrates," *Journal of Physics D: Applied Physics,* vol. 41, no. 232004, pp. 1-5, 2008.

[129] W. J. Padilla, M. T. Aronsson, C. Highstrete, M. Lee, A. J. Taylor and R. D. Averitt, "Electrically resonant terahertz metamaterials: Theoretical and experimental investigations," *PHYSICAL REVIEW B,* vol. 75, no. 041102, pp. 1-4, 2007.

[130] W. J. Padilla, A. J. Taylor, C. Highstrete, M. Lee and R. D. Averitt, "Dynamical Electric and Magnetic Metamaterial Response at Terahertz Frequencies," *PHYSICAL REVIEW LETTERS,* vol. 96, no. 107401, pp. 1-4, 2006.

[131] H.-T. Chen, W. J. Padilla, J. M. O. Zide, A. C. Gossard, A. J. Taylor and R. D. Averitt, "Active terahertz metamaterial devices," *nature,* vol. 444, no. 30, pp. 597-600, 2006.

[132] Y. Lee, S.-J. Kim, H. Park and B. Lee, "Metamaterials and Metasurfaces for Sensor Applications," *Sensors,* vol. 17, no. 1726, pp. 1-28, 2017.

[133] A. Salim and S. Lim, "Review of Recent Metamaterial Microfluidic Sensors," *Sensors,* vol. 18, no. 232, pp. 1-25, 2018.

[134] Y. Zhang, J. Zhao, J. Cao and B. Mao, "Microwave Metamaterial Absorber for Non-Destructive Sensing Applications of Grain," *Sensors,* vol. 18, no. 1912, pp. 1-10, 2018.

[135] S. J. M. Rao, Y. K. Srivastava, G. Kumar and D. R. Chowdhury, "Modulating Fundamental Resonance in Capacitive Coupled Asymmetric Terahertz Metamaterials," *Scientific REPORTS,* vol. 8, no. 16773, pp. 1-8, 2018.

[136] M. Islam, S. J. M. Rao, G. Kumar, B. P. Pal and D. R. Chowdhury, "Role of Resonance Modes on Terahertz Metamaterials based Thin Film Sensors," *Scientific REPORTS,* vol. 7, no. 7355, pp. 1-8, 2017.

[137] Z. C. Chen, N. R. Han, Z. Y. Pan, Y. D. Gong, T. C. Chong and M. H. Hong, "Tunable resonance enhancement of multi-layer terahertz metamaterials fabricated by parallel laser micro-lens array lithography on flexible substrates," *OPTICAL MATERIALS EXPRESS,* vol. 1, no. 20, pp. 151-157, 2011.

[138] R. Singh, I. A. I. Al-Naib, M. Koch and W. Zhang, "Asymmetric planar terahertz metamaterials," *OPTICS EXPRESS,* vol. 18, no. 12, pp. 13044-13050, 2010.

[139] A. P. Tenggara, S. J. Park, H. T. Yudistira, Y. H. Ahn and D. Byun, "Fabrication of terahertz metamaterials using electrohydrodynamic jet printing for sensitive detection of yeast," *J. Micromech. Microeng,* vol. 27, no. 035009, pp. 1-8, 2017.

[140] S. J. Park, S. W. Jun, A. R. Kim and Y. H. Ahn, "Terahertz metamaterial sensing on polystyrene microbeads: shape dependence," *OPTICAL MATERIALS EXPRESS,* vol. 5, no. 10, pp. 2150-2155, 2015.

[141] R. Singh, A. K. Azad, J. F. O'Hara, A. J. Taylor and W. Zhang, "Effect of metal

permittivity on resonant properties of terahertz metamaterials," *OPTICS LETTERS,* vol. 33, no. 13, pp. 1506-1508, 2008.

[142] H. S. KIM, S. H. CHA, B. ROY, S. KIM and Y. H. AHN, "Humidity sensing using THz metamaterial with silk protein fibroin," *OPTICS EXPRESS,* vol. 26, no. 26, pp. 33575-33581, 2018.

[143] J. T. Hong, S. W. Jun, S. H. Cha, J. Y. Park, S. Lee, G. A. Shin and Y. H. Ahn, "Enhanced sensitivity in THz plasmonic sensors with silver nanowires," *Scientific REPORTS,* vol. 8, no. 15536, pp. 1-8, 2018.

[144] S. J. PARK, S. H. CHA, G. A. SHIN and Y. H. AHN, "Sensing viruses using terahertz nano-gap metamaterials," *BIOMEDICAL OPTICS EXPRESS,* vol. 8, no. 8, pp. 3551-3558, 2017.

[145] L. Cong, S. Tan, R. Yahiaoui, F. Yan, W. Zhang and R. Singh, "Experimental demonstration of ultrasensitive sensing with terahertz metamaterial absorbers: A comparison with the metasurfaces," *APPLIED PHYSICS LETTERS,* vol. 106, no. 031107, pp. 1-5, 2015.

[146] M. Liu, H. Y. Hwang, H. Tao, A. C. Strikwerda, K. Fan, G. R. Keiser, A. J. Sternbach, K. G. West, S. Kittiwatanakul, J. Lu, S. A. Wolf, F. G. Omenetto, X. Zhang, K. A. Nelson and R. Averitt, "Terahertz-field-induced insulator-to-metal transition in vanadium dioxide metamaterial," *Nature,* vol. 487, no. 11231, pp. 345-348, 2012.

[147] H.-T. CHEN, J. F. O'HARA, A. K. AZAD, A. J. TAYLOR, R. D. AVERITT, D. B. SHREKENHAMER and W. J. PADILLA, "Experimental demonstration of frequency-agile terahertz metamaterials," *nature photonics,* vol. 2, pp. 295-298, 2008.

[148] S. J. Park, S. A. N. Yoon and Y. H. Ahn, "Effective Sensing Volume of Terahertz Metamaterial with Various Gap Widths," *Journal of the Optical Society of Korea,* vol. 20, no. 5, pp. 628-632, 2016.

[149] D. J. Park, S. J. Park, I. Park and Y. H. Ahn, "Dielectric substrate effect on the metamaterial resonances in terahertz frequency range," *Current Applied Physics,* vol. 14, pp. 570-574, 2014.

[150] J. F. O'Hara, R. Singh, I. Brener, E. Smirnova, J. Han, A. J. Taylor and W. Zhang, "Thin-film sensing with planar terahertz metamaterials: sensitivity and limitations," *OPTICS EXPRESS,* vol. 16, no. 3, pp. 1786-1795, 2008.

[151] S. J. Park, B. H. Son, S. J. Choi, H. S. Kim and Y. H. Ahn, "Sensitive detection of yeast using terahertz slot antennas," *OPTICS EXPRESS,* vol. 22, no. 25, pp. 30467-30472, 2014.

[152] Y. Backlund and L. Rosengren, "New shapes in (100) Si using KOH and EDP etches," *J. Micromech. Microeng,* vol. 2, pp. 75-79, 1992.

[153] I. Zubel and K. P. Rola, "The effect of monohydric and polyhydric alcohols on silicon anisotropic etching in KOH solutions," *Sensors and Actuators A,* vol. 266, pp. 145-157, 2017.

[154] H. Tanaka, S. Yamashita, Y. Abe, M. Shikida and K. Sato, "Fast etching of silicon with a smooth surface in high temperature ranges near the boiling point of KOH solution," *Sensors and Actuators,* vol. 114, pp. 516-520, 2004.

[155] K. Biswas and S. Kal, "Etch characteristics of KOH, TMAH and dual doped TMAH for bulk micromachining of silicon," *Microelectronics Journal,* vol. 37, pp. 519-525, 2006.

[156] K. Sato, M. Shikida, Y. Matsushima, T. Yamashiro, K. Asaumi, Y. Iriye and M. Yamamoto, "Characterization of orientation-dependent etching properties of single-crystal silicon: effects of KOH concentration," *Sensors and Actuators A,* vol. 64, pp. 87-93, 1998.

[157] Y. Fan, P. Han, P. Liang, Y. Xing, Z. Ye and S. Hu, "Differences in etching characteristics of TMAH and KOH on preparing inverted pyramids for silicon solar cells," *Applied Surface Science,* vol. 264, pp. 761-766, 2013.

[158] A. V. N. Rao, V. Swarnalatha and P. Pal, "Etching characteristics of Si{110} in 20 wt% KOH with addition of hydroxylamine for the fabrication of bulk micromachined MEMS," *Micro and Nano Syst Lett,* vol. 5, no. 23, pp. 1-9, 2017.

[159] M. OGITA, T. CARROLL, J. WEI, J. V. D. SPIEGEL and J. N. ZEMEL, "Use of gold films as masks for a KOH preferential etch," *Thin Solid Films,* vol. 120, pp. 79-81, 1984.

[160] N. Fujitsuka, K. Hamaguchi, H. Funabashi, E. Kawasaki and T. Fukada, "Aluminum Protected Silicon Anisotropic Etching Technique Using TMAH with an Oxidizing Agent and Dissolved Si," *R&D Review of Toyota CRDL,* vol. 39, no. 2, pp. 34-40, 2004.

[161] J. Ohara, K. Asami, Y. Takeuchi and K. Sato, "Development of RIE-lag Reduction Technique for Si Deep Etching Using Double Protection Layer Method," *IEEJ Trans,* vol. 5, pp. 125-130, 2010.

[162] H. Zou, "Anisotropic Si deep beam etching with profile control using SF6/O2 Plasma," *Microsystem Technologies,* vol. 10, pp. 603-607, 2004.

[163] D. R. BACON, A. D. BURNETT, M. SWITHENBANK, C. RUSSELL, L. LI, C. D. WOOD, J. CUNNINGHAM, E. H. LINFIELD, A. G. DAVIES, P. DEAN and J. R. FREEMAN, "Free-space terahertz radiation from a LT-GaAs-on-quartz large-area photoconductive emitter," *OPTICS EXPRESS,* vol. 24, no. 23, pp. 26986-26997, 2016.

[164] Y.-S. Jin, G.-J. Kim and S.-G. Jeon, "Terahertz Dielectric Properties of Polymers," *Journal of the Korean Physical Society,,* vol. 49, no. 2, pp. 513-517, 2006.

[165] S. J. Park and Y. H. Ahn, "Substrate Effects on Terahertz Metamaterial Resonances for Various Metal Thicknesses," *Journal of the Korean Physical Society,* vol. 65, no. 11, pp. 1843-1847, 2014.

[166] Y. Chen, I. A. I. Al-Naib, J. Gu, M. Wang, T. Ozaki, R. Morandotti and W. Zhang, "Membrane metamaterial resonators with a sharp resonance: A comprehensive study towards practical terahertz filters and sensors," *AIP ADVANCES,* vol. 2, no. 022109, pp. 1-9, 2012.

[167] J. Cunningham, C. Wood, A. G. Davies, C. K. Tiang, P. Tosch, D. A. Evans, E. H. Linfield and I. C. Hunter, "Multiple-frequency terahertz pulsed sensing of dielectric films," *APPLIED PHYSICS LETTERS,* vol. 88, no. 071112, pp. 1-3, 2006.

[168] S. J. Park, S. A. N. Yoon and Y. H. Ahn, "Dielectric constant measurements of thin films and liquids using terahertz metamaterials," *RSC Adv.,* vol. 6, pp. 69381-69386, 2016.

[169] F. Marty, L. Rousseau, B. Saadany, B. Mercier, O. Francais, Y. Mita and T. Bourouina, "Advanced etching of silicon based on deep reactive ion etching for silicon high aspect ratio microstructures and three-dimensional micro- and nanostructures," *Microelectronics Journal,* vol. 36, pp. 673-677, 2005.

[170] A. Tredicucci and M. S. Vitiello, "Device Concepts for Graphene-Based Terahertz Photonics," *IEEE JOURNAL OF SELECTED TOPICS IN QUANTUM ELECTRONICS,* vol. 20, no. 1, pp. 1-9, 2014.

[171] M. Wang and E.-H. Yang, "THz applications of 2D materials: Graphene and beyond," *Nano-Structures & Nano-Objects,* vol. 15, pp. 107-113, 2018.

[172] S. H. Abedinpour and G. Vignale, "Drude weight, plasmon dispersion, and ac conductivity in doped graphene sheets," *PHYSICAL REVIEW B,* vol. 84, no. 045429, pp. 1-14, 2011.

[173] P. A. George, J. Strait, J. Dawlaty, S. Shivaraman, M. Chandrashekhar, F. Rana and M. G. Spencer, "Ultrafast Optical-Pump Terahertz-Probe Spectroscopy of the Carrier Relaxation and Recombination Dynamics in Epitaxial Graphene," *Nano Lett.,* vol. 8, no. 12, pp. 4248-4251, 2008.

[174] J. Horng, C.-F. Chen, B. Geng, C. Girit, Y. Zhang, Z. Hao, H. A. Bechtel, M. Martin, A. Zettl, M. F. Crommie, Y. R. Shen and F. Wang, "Drude conductivity of Dirac fermions in graphene," *PHYSICAL REVIEW B,* vol. 83, no. 165113, pp. 1-5, 2011.

[175] R. R. Hartmann, J. Kono and M. E. Portnoi, "Terahertz science and technology of carbon nanomaterials," *Nanotechnology,* vol. 25, no. 32, pp. 322001-322016, 2014.

[176] V. Ryzhii, M. Ryzhii, V. Mitin and T. Otsuji, "Toward the creation of terahertz graphene injection laser," *JOURNAL OF APPLIED PHYSICS,* vol. 110, no. 9, p. 094503, 2011.

[177] K. J. Tielrooij, J. C. W. Song, S. A. Jensen, A. Centeno, A. Pesquera, A. Z. Elorza, M. Bonn, L. S. Levitov and F. H. L. Koppens, "Photoexcitation cascade and multiple hot-carrier generation in graphene," *NATURE PHYSICS,* vol. 9, pp. 248-252, 2013.

[178] T. Winzer and E. Malic, "Impact of Auger processes on carrier dynamics in graphene," *Phys. Rev. B,* vol. 85, no. 24, p. 241404, 2012.

[179] G. Jnawali, Y. Rao, H. Yan and T. F. Heinz, "Observation of a Transient Decrease in Terahertz Conductivity of Single-Layer Graphene Induced by Ultrafast Optical Excitation," *Nano Lett.,* vol. 13, pp. 524-530, 2013.

[180] P. Tassin, T. Koschny and C. M. Soukoulis, "Graphene for Terahertz Applications," *SCIENCE,* vol. 341, no. 6146, pp. 620-621, 2013.

[181] J. Zhu, B. Ruan, Q. You, J. Guo, X. Dai and Y. Xiang, "Terahertz imaging sensor based on the strong coupling of surface plasmon polaritons between PVDF and graphene," *Sensors and Actuators B: Chemical,* vol. 264, pp. 398-403, 2018.

[182] X. HE, F. LIU, F. LIN and W. SHI, "Graphene patterns supported terahertz tunable plasmon induced transparency," *OPTICS EXPRESS,* vol. 26, no. 8, pp. 9931-9944, 2018.

[183] A. Noual, M. Amrani, E. E. Boudouti, Y. Pennec and B. Djafari-Rouhani, "Terahertz multi-plasmon induced reflection and transmission and sensor devices in a graphene-based coupled nanoribbons resonators," *Optics Communications,* vol. 440, pp. 1-13, 2019.

[184] Z. Sun, A. Martinez and F. Wang, "Optical modulators with 2D layered materials," *NATURE PHOTONICS,* vol. 10, pp. 227-238, 2016.

[185] L. Wang, Z. Sofer, P. Šimek, I. Tomandl and M. Pumera, "Boron-Doped Graphene: Scalable and Tunable p-Type Carrier Concentration Doping," *J. Phys. Chem. C,* vol. 117, pp. 23251-23257, 2013.

[186] X. Cai, A. B. Sushkov, R. J. Suess, M. M. Jadidi, G. S. Jenkins, L. O. Nyakiti, R. L. Myers-Ward, S. Li, J. Yan, D. K. Gaskill, T. E. Murphy, H. D. Drew and M. S. Fuhrer, "Sensitive Room-Temperature Terahertz Detection via Photothermoelectric Effect in Graphene," *Nature Nanotechnology,* vol. 9, pp. 814-819, 2014.

[187] X. Yang, A. Vorobiev, A. Generalov, M. A. Andersson and J. Stake, "A flexible graphene terahertz detector," *APPLIED PHYSICS LETTERS,* vol. 111, no. 021102, pp. 1-4, 2017.

[188] J. Tong, M. Muthee, S.-Y. Chen, S. K. Yngvesson and J. Yan, "Antenna Enhanced Graphene THz Emitter and Detector," *Nano Lett.,* vol. 15, pp. 5295-5301, 2015.

[189] A. V. Muraviev, S. L. Rumyantsev, G. Liu, A. A. Balandin, W. Knap and M. S. Shur, "Plasmonic and bolometric terahertz detection by graphene field-effect transistor," *APPLIED PHYSICS LETTERS,* vol. 103, no. 181114, pp. 1-4, 2013.

[190] D. Zhou, L. Xiao, B. Xiao, F. Guo, X. Yu, H. Ling and Z. Xu, "A high-performance terahertz modulator based on double-layer graphene," *Optics Communications,* vol. 427, pp. 215-219, 2018.

[191] Q. Li, Z. Tian, X. Zhang, R. Singh, L. Du, J. Gu, J. Han and W. Zhang, "Active graphene–silicon hybrid diode for terahertz waves," *NATURE COMMUNICATIONS,* vol. 6, no. 7028, pp. 1-6, 2015.

[192] I. Chatzakis, Z. Li, A. V. Benderskii and S. B. Cronin, "Broadband terahertz modulation in electrostatically-doped artificial trilayer graphene," *Nanoscale,* vol. 9, pp. 1721-1726, 2017.

[193] B. Sensale-Rodriguez, R. Yan, S. Rafique, M. Zhu, W. Li, X. Liang, D. Gundlach, V. Protasenko, M. M. Kelly, D. Jena, L. Liu and H. G. Xing, "Extraordinary Control of Terahertz Beam Reflectance in Graphene Electro-absorption Modulators," *Nano Lett.,* vol. 12, pp. 4518-4522, 2012.

[194] F. Yan, C. Yu, H. Park, E. P. J. Parrott and E. Pickwell-MacPherson, "Advances in Polarizer Technology for Terahertz Frequency Applications," *J Infrared Milli Terahz Waves,* vol. 34, pp. 489-499, 2013.

[195] J. WEI and N. C. PANOIU, "Polarization control using passive and active crossed graphene gratings," *OPTICS EXPRESS,* vol. 26, no. 2, pp. 1882-1894,

2018.

[196] S. WU, D. ZHA, Y. HE, L. MIAO and J. JIANG, "Design of stable and high-efficiency graphene- based polarizers for oblique angle of incidence in terahertz frequency," *Applied Optics,* vol. 58, no. 3, pp. 492-497, 2019.

[197] L. Zhu, Y. Fan, S. Wu, L. Yu, K. Zhang and Y. Zhang, "Electrical control of terahertz polarization by graphene microstructure," *Optics Communications,* vol. 346, pp. 120-123, 2015.

[198] Y. Zhang, Y. Feng, B. Zhu, J. Zhao and T. Jiang, "Graphene based tunable metamaterial absorber and polarization modulation in terahertz frequency," *OPTICS EXPRESS,* vol. 22, no. 19, pp. 22743-22752, 2014.

[199] T. K. Nguyen, W. T. Kim, B. J. Kang, H. S. Bark, K. Kim, J. Lee, I. Park, T.-I. Jeon and F. Rotermund, "Photoconductive dipole antennas for efficient terahertz receiver," *Optics Communications,* vol. 383, pp. 50-56, 2017.

[200] K. Nagashio, T. Nishimura, K. Kita and A. Toriumi, "Metal/graphene contact as a performance Killer of ultra-high mobility graphene analysis of intrinsic mobility and contact resistance," in *2009 IEEE International Electron Devices Meeting (IEDM)*, Baltimore, 2009.

[201] D. M. Basko, S. Piscanec and A. C. Ferrari, "Electron-electron interactions and doping dependence of the two-phonon Raman intensity in graphene," *PHYSICAL REVIEW B,* vol. 80, no. 165413, pp. 1-10, 2009.

[202] S. Gupta, M. Y. Frankel, J. A. Valdmanis, J. F. Whitaker, G. A. Mourou, F. W. Smith and A. R. Calawa, " Subpicosecond carrier llifetime in GaAs grown by molecular beam epitaxy at low temperatures," *Appl. Phys. Lett.,* vol. 59, no. 25, pp. 3276-3278, 1991.

[203] J. E. Heyes, W. Withayachumnankul, N. K. Grady, D. R. Chowdhury, A. K. Azad and H. Chen, "Hybrid metasurface for ultra-broadband terahertz modulation," *Applied Physics Letters,* vol. 105, no. 181108, pp. 1-5, 2014.

[204] J. Wu, "Enhancement of Absorption in Graphene Strips With Cascaded Grating Structures," *IEEE Photonics Tchnol. Lett.,* vol. 28, pp. 1332-1335, 2016.

[205] M. Grande, G. V. Bianco, M. A. Vincenti, D. d. Ceglia, P. Capezzuto, M. Scalora, A. D'Orazio and G. Bruno, "Optically Transparent Microwave Polarizer Based On Quasi-Metallic Graphene," *Scientific Reports,* vol. 5, p. 17083, 2015.

[206] Y. Xia, Y. Dai, B. Wang, A. Chen, Y. Zhang, Y. Zhang, F. Guan, X. Liu, L. Shi and J. Zi, "Polarization dependent plasmonic modes in elliptical graphene disk arrays," *Optics Express,* vol. 27, no. 2, pp. 1080-1089, 2019.

[207] S. Xiao and N. A. Mortensen, "Surface-plasmon-polariton-induced suppressed transmission through ultrathin metal disk arrays," *OPTICS LETTERS,* vol. 36, no. 1, pp. 37-39, 2011.

[208] Z. Miao, Q. Wu, X. Li, Q. He, K. Ding, Z. An, Y. Zhang and L. Zhou, "Widely Tunable Terahertz Phase Modulation with Gate-Controlled Graphene Metasurfaces," *PHYSICAL REVIEW X,* vol. 5, no. 041027, pp. 1-13, 2015.

[209] B. J. Kim, H. Jang, S.-K. Lee, B. H. Hong, J.-H. Ahn and J. H. Cho, "High-Performance Flexible Graphene Field Effect Transistors with Ion Gel Gate Dielectrics," *Nano Lett.,* vol. 10, pp. 3464-3466, 2010.

[210] K. Chae, N. D. Cuong, S. Ryu, D.-I. Yeom, Y. Ahn, S. Lee and J.-Y. Park, "Electrical properties of ion gels based on PVDF-HFP applicable as gate stacks for flexible devices," *Current Applied Physics,* vol. 18, pp. 500-504, 2018.

[211] B. Sensale-Rodriguez, T. Fang, R. Yan, M. M. Kelly, D. Jena, L. Liu and H. Xing, "Unique prospects for graphene-based terahertz modulators," *APPLIED PHYSICS LETTERS,* vol. 99, no. 113104, pp. 1-3, 2011.

[212] . O. Luukkonen, . C. Simovski, . G. Granet, . G. Goussetis, . D. Lioubtchenko, . A. V. Raisanen and . S. A. Tretyakov, "Simple and Accurate Analytical Model of Planar Grids and High-Impedance Surfaces Comprising Metal Strips or Patches," *IEEE Transactions on Antennas and Propagation,* vol. 56, no. 6, pp. 1624-1632, 2008.

[213] G. Viola, T. Wenger, J. Kinaret and M. Fogelstrom, "Graphene plasmons: Impurities and nonlocal effects," *Phyiscal Review B,* vol. 97, p. 085429, 2018.

[214] R. H. Parmenter, "The acousto-electric effect," *PHYSICAL REVIEW,* vol. 89, no. 5, pp. 990-998, 1953.

[215] G. WEINREICH and H. G. WHITE, "Observation of the Acoustoelectric Effect," *Phys. Rev.,* vol. 106, pp. 1104-1106, 1957.

[216] J. Campbell, F. Guillon, M. D'Iorio, M. Buchanan and R. Stoner, "Characterization of the surface acoustic wave induced potential in a GaAsAlGaAs heterostructure," *Solid State Communications,* vol. 84, no. 7, pp. 735-738, 1992.

[217] J. M. Shilton, D. R. Mace, V. I. Talyanskii, M. Pepper, M. Y. Simmons, A. C. Churchill and D. A. Ritchie, "Effect of spatial dispersion on acoustoelectric current in a high-mobility two-dimensional electron gas," *PHYSICAL REVIEW B,* vol. 51, no. 20, pp. 14770-14773, 1995.

[218] M. Rotter, A. Wixforth, A. O. Govorov, W. Ruile, D. Bernklau and H. Riechert, "Nonlinear acoustoelectric interactions in GaAs/LiNbO3 structures," *APPLIED PHYSICS LETTERS,* vol. 75, no. 7, pp. 965-967, 1999.

[219] J. M. Shilton, V. I. Talyanskii, M. Pepper, D. A. Ritchie, J. E. F. Frost, C. J. B. Ford, C. G. Smith and G. A. C. Jones, "High-frequency single-electron transport in a quasi-one-dimensional GaAs channel induced by surface acoustic waves," *J. Phys.: Condens. Matter,* vol. 8, pp. 531-539, 1996.

[220] V. I. Talyanskii, J. M. Shilton, M. Pepper, C. G. Smith, C. J. B. Ford, E. H. Linfield, D. A. Ritchie and G. A. C. Jones, "Single-electron transport in a one-dimensional channel by high-frequency surface acoustic waves," *PHYSICAL REVIEW B,* vol. 56, no. 23, pp. 15180-15184, 1997.

[221] J. Ebbecke, N. E. Fletcher, T. J. B. M. Janssen, F. J. Ahlers, M. Pepper, H. E. Beere and D. A. Ritchie, "Quantized charge pumping through a quantum dot by surface acoustic waves," *APPLIED PHYSICS LETTERS,* vol. 84, no. 21, pp. 4319-4321, 2004.

[222] F. Stein, D. Drung, L. Fricke, H. Scherer, F. Hohls, C. Leicht, M. Gotz, C. Krause, R. Behr, E. Pesel, K. Pierz, U. Siegner, F. J. Ahlers and H. W. Schumacher, "Validation of a quantized-current source with 0.2 ppm uncertainty," *APPLIED PHYSICS LETTERS,* vol. 107, no. 103501, pp. 1-5, 2015.

[223] J. Cunningham, V. Talyanski , J. Shilton, M. Pepper, D. Ritchie, G. Jones, C. Ford, C. Smith, A. Kristensen and P. Lindelof, "Quantised current driven by surface acoustic waves," *Materials Science and Engineering C,* vol. 15, pp. 97-100, 2001.

[224] A. Hernández-Mínguez, Y.-T. Liou and P. V. Santos, "Interaction of surface acoustic waves with electronic excitations in graphene," *J. Phys. D: Appl. Phys.,* vol. 51, no. 383001, pp. 1-17, 2018.

[225] L. Bandhu, L. M. Lawton and G. R. Nash, "Macroscopic acoustoelectric charge transport in graphene," *APPLIED PHYSICS LETTERS,* vol. 103, no. 133101, pp. 1-4, 2013.

[226] J. R. Lane, L. Zhang, M. A. Khasawneh, B. N. Zhou, E. A. Henriksen and J. Pollanen, "Flip-chip gate-tunable acoustoelectric effect in graphene," *JOURNAL OF APPLIED PHYSICS,* vol. 124, no. 194302, pp. 1-6, 2018.

[227] Y.-T. Liou, A. Hernández-Mínguez, J. Herfort, J. M. J. Lopes, A. Tahraoui and P. V. Santos, "Acousto-electric transport in MgO/ZnO-covered graphene on SiC," *J. Phys. D: Appl. Phys.,* vol. 50, no. 464008, pp. 1-10, 2017.

[228] P. V. Santos, T. Schumann, M. H. Oliveira, Jr., J. M. J. Lopes and H. Riechert, "Acousto-electric transport in epitaxial monolayer graphene on SiC," *APPLIED PHYSICS LETTERS,* vol. 102, no. 221907, pp. 1-3, 2013.

[229] N. Ma and M. S. Reis, "Anomalous acoustic phonons as the physical mechanism behind the adiabatic barocaloric effect on graphene," *Scientific Reports,* vol. 9, no. 219, pp. 1-6, 2019.

[230] Y. Koohsarian, K. Javidan and A. Shirzad, "Casimir energy for acoustic phonons in graphene," *EPL,* vol. 119, no. 48002, pp. 1-6, 2017.

[231] K. A. Dompreh, N. G. Mensah and S. Y. Mensah, "Acoustoelectric effect in graphene with degenerate energy dispersion," *Physica E,* vol. 85, pp. 160-163, 2017.

[232] F. SCHEDIN, A. K. GEIM, S. V. MOROZOV, E. W. HILL, P. BLAKE, M. I. KATSNELSON and K. S. NOVOSELOV, "Detection of individual gas molecules adsorbed on graphene," *nature materials,* vol. 6, pp. 652-655, 2007.

[233] A. Kumari, N. Prasad, P. K. Bhatnagar, P. C. Mathur, A. K. Yadav, C. V. Tomy and C. S. Bhatia, "Electrical transport properties of polycrystalline CVD graphene on SiO2/Si substrate," *Diamond & Related Materials,* vol. 45, pp. 28-33, 2014.

[234] M. Kataoka, C. J. B. Ford, C. H. W. Barnes, D. Anderson, G. A. C. Jones, H. E. Beere, D. A. Ritchie and M. Pepper, "The effect of pulse-modulated surface acoustic waves on acoustoelectric current quantization," *JOURNAL OF APPLIED PHYSICS,* vol. 100, no. 063710, pp. 1-4, 2006.

[235] K. I. Bolotin, K. J. Sikes, J. Hone, H. L. Stormer and P. Kim, "Temperature-Dependent Transport in Suspended Graphene," *PHYSICAL REVIEW LETTERS,* vol. 101, no. 096802, pp. 1-4, 2008.

[236] V. Skákalová, A. B. Kaiser, J. S. Yoo, D. Obergfell and S. Roth, "Correlation between resistance fluctuations and temperature dependence of conductivity in graphene," *PHYSICAL REVIEW B,* vol. 80, no. 153404, pp. 1-4, 2009.

[237] M. Y. Han, J. C. Brant and P. Kim, "Electron Transport in Disordered Graphene Nanoribbons," *PHYSICAL REVIEW LETTERS,* vol. 104, no. 056801, pp. 1-4, 2010.

[238] B. Drafts, "Acoustic Wave Technology Sensors," *IEEE TRANSACTIONS ON MICROWAVE THEORY AND TECHNIQUES,* vol. 49, no. 4, pp. 795-802, 2001.

[239] Y. Zhang, V. W. Brar, C. Girit, A. Zettl and M. F. Crommie, "Origin of spatial charge inhomogeneity in graphene," *NATURE PHYSICS,* vol. 5, pp. 722-726, 2009.

[240] H. S. Song, S. L. Li, H. Miyazaki, S. Sato, K. Hayashi, A. Yamada, N. Yokoyama and K. Tsukagoshi, "Origin of the relatively low transport mobility of graphene grown through chemical vapor deposition," *SCIENTIFIC REPORTS,* vol. 2, no. 337, pp. 1-6, 2012.

[241] O. V. Yazyev and S. G. Louie, "Electronic transport in polycrystalline graphene," *NATURE MATERIALS,* vol. 9, pp. 806-809, 2010.

[242] Y. Hu, P. Xie, M. D. Corato, A. Ruini, S. Zhao, F. Meggendorfer, L. A. Straasø, L. Rondin, P. Simon, J. Li, J. J. Finley, M. R. Hansen, J.-S. Lauret, E. Molinari, X. Feng and Bart, "Bandgap Engineering of Graphene Nanoribbons by Control over Structural Distortion," *J. Am. Chem. Soc,* vol. 140, pp. 7803-7809, 2018.

[243] L. Zheng, X. Cheng, D. Cao, Z. Wang, C. Xia, Y. Yu and D. Shen, "Property transformation of graphene with Al2O3 films deposited directly by atomic layer deposition," *APPLIED PHYSICS LETTERS,* vol. 104, no. 023112, pp. 1-5, 2014.